



UNIVERSITÀ DI PISA

SCUOLA DI INGEGNERIA

Dipartimento di Ingegneria dell'Energia, dei Sistemi, del Territorio
e delle Costruzioni

Tesi di Laurea Magistrale in Ingegneria Energetica

**Identification, Modeling and Analysis of
Energy Losses in a SOFC/GT
Hybrid Power Plant**

Candidata:
Costanza Saletti

Relatore:
Prof. Umberto Desideri

Supervisor:
Mike Steilen

Anno Accademico 2015-2016

Alla mia Big Family

Abstract

Hybrid power plants consisting of a solid oxide fuel cell (SOFC) and a gas turbine (GT) are an interesting field of research due to the expected high electrical efficiency, fuel flexibility and part-load good performance.

At DLR (German Aerospace Center), a demonstration SOFC/GT hybrid power plant is being built and its operation is being simulated by means of a global system model that does not account for heat losses. The system models available in literature are adiabatic as well. Though, considering heat losses during stationary operation allows for an improved prediction of the operating range as well as for the prevention of undesired operating problems. Similarly, investigating the heat capacity of the system during transient processes allows for the examination of new possible operating strategies.

In the present thesis, the energy losses from the hybrid power plant are identified and modeled, in order to integrate the global system model and enhance its accuracy while keeping a low computational time. Due to the complexity of the system, the high number of components and the loop-type interactions between them, a high computational speed is required to analyze a large number of operating points and boundary conditions.

For this purpose, different modeling strategies are compared. Various multi-dimensional models for the evaluation of heat losses from the components of the hybrid power plant are created in the MATLAB environment for both stationary and transient operation. The real system parameters are implemented by building a database for material properties and components geometries.

The results obtained with the different models are then compared in order to choose the paradigm that gives the lowest computational time while maintaining a feasible accuracy. Eventually, a zero-dimensional model is selected for the implementation in the global system simulation, as it meets those requirements.

Therefore, a complete set of fast and reliable sub-models for stationary and transient simulations is available to carry on future studies and thoroughly investigate the operation of the SOFC/GT hybrid power plant.

Sommario

Gli impianti ibridi costituiti da celle a combustibile ad ossidi solidi (SOFC) e turbina a gas (GT) rappresentano un campo di ricerca interessante a causa dell'elevato rendimento elettrico atteso, della flessibilità di funzionamento con diversi combustibili e delle buone prestazioni a carico parziale.

Nel DLR (German Aerospace Center), un impianto ibrido SOFC/GT dimostrativo è in costruzione e il suo funzionamento viene simulato per mezzo di un modello globale di sistema che non include le perdite termiche. I modelli di sistema disponibili in letteratura per questo tipo di impianto sono anch'essi adiabatici.

Tuttavia, considerare le perdite termiche durante il funzionamento stazionario consente sia di migliorare la previsione del range di funzionamento dell'impianto, sia di prevenire l'insorgere di problematiche operative. Analogamente, considerare la capacità termica del sistema come sistema di accumulo termico durante i processi transitori consente di indagare nuove possibili strategie di operazione.

Lo scopo di questa tesi è effettuare l'identificazione e la modellazione delle perdite energetiche dell'impianto ibrido SOFC/GT del DLR, in modo da integrare il modello globale di sistema e aumentare la sua correttezza, mantenendo allo stesso tempo un basso costo computazionale. A causa infatti della complessità del sistema, dell'elevato numero di componenti e delle interazioni cicliche tra essi, un'alta velocità computazionale è indispensabile per poter analizzare molteplici modalità di funzionamento e condizioni al contorno.

Per questo scopo, sono state confrontate differenti strategie di modellazione. Vari modelli multidimensionali per la valutazione delle perdite termiche dai componenti dell'impianto durante i funzionamenti sia stazionario che dinamico sono stati costruiti in ambiente MATLAB. I parametri reali del sistema sono stati implementati attraverso la costruzione di un database per la geometria dei componenti e per le proprietà dei materiali.

I risultati ottenuti con i diversi metodi sono poi stati confrontati per scegliere la strategia che dia il minor tempo computazionale pur mantenendo una buona accuratezza. Un modello zero-dimensionale è stato infine selezionato per l'implementazione nelle simulazioni dell'intero sistema, poichè rispetta i requisiti citati.

Quindi, una serie completa di sotto-modelli rapidi ed affidabili per simulazioni stazionarie e dinamiche è ora disponibile per portare avanti ulteriori studi e analizzare scrupolosamente il funzionamento dell'impianto ibrido SOFC/GT.

Contents

List of Figures	vii
List of Tables	viii
Nomenclature	ix
1 Introduction	1
1.1 Motivation	2
1.2 Outline of the Thesis	3
2 State of the Scientific and Technical Knowledge	5
2.1 SOFC/GT Hybrid Power Plant Concept	5
2.1.1 Fuel Cell	5
2.1.2 Gas Turbine	7
2.1.3 Hybrid Power Plant	8
2.2 Hybrid Power Plant Modeling	11
2.3 Multi-dimensional Heat Transfer Modeling	13
3 Theoretical Fundamentals	17
3.1 Heat Transfer	17
3.1.1 Conduction	17
3.1.2 Convection	18
3.1.3 Radiation	21
3.1.4 Thermal Resistance	22
3.1.5 Transient Heat Transfer	26
3.2 Computational Heat Transfer	28
4 Model Implementation	35
4.1 Computation of Thermo-physical Properties	37
4.1.1 Gas Properties	37
4.1.2 Solid Material Properties	39
4.2 Stationary Model	40
4.2.1 Two-dimensional approach	42
4.2.2 One-dimensional approach	43
4.2.3 Zero-dimensional approach	45
4.3 Transient Model	50
4.4 Computational Time	51

Contents

4.4.1	Mathematical Simplifications	51
4.4.2	Conceptual Simplifications	52
4.5	Models of Components	54
4.5.1	Reformer	55
4.5.2	Recirculation Blower	56
4.5.3	Heat Exchanger	59
4.5.4	Burner	62
4.5.5	Gas Turbine	63
4.5.6	SOFC Stack Modules	65
4.5.7	Pressure Vessel	66
5	Discussion and Results	69
5.1	Comparison 2D vs 1D	69
5.2	Comparison 1D vs 0D	73
5.3	Implementation of Gas Mean Temperature	77
5.4	Comparison with Experimental Results	78
5.5	Stationary vs Transient	80
5.6	Adiabatic vs Non-Adiabatic	84
6	Conclusions	87
	Acknowledgements	xiv
	References	xv

List of Figures

1.1	Comparison of electrical efficiencies of different power plant types . . .	1
2.1	Schematic representation of the type of solid oxide fuel cell used at DLR	6
2.2	Schematic representation of a gas turbine.	8
2.3	Schematic representation of a hybrid power plant made by a SOFC system and a gas turbine	9
2.4	Schematic representation of the configuration used at DLR for the prototype SOFC/GT hybrid power plant	10
3.1	Thermal resistance.	23
3.2	Cylindrical shell.	24
3.3	Convective and radiative thermal resistances from a surface to the ambient	25
3.4	Representation of the thermal resistances of a tube with a gas flowing inside and ambient air outside	25
3.5	Representation of a generic control volume	26
3.6	Thermal resistance and thermal capacity of a material	28
3.7	Grid or mesh centered in the volume	30
3.8	Control volume P and its surrounding ones for the two-dimensional situation	30
3.9	Boundary control volume B with a convective boundary condition. . .	32
4.1	Black-box concept	35
4.2	Hybrid power plant global model concept	36
4.3	Percentage deviation of dynamic viscosity and thermal conductivity of a generic gas mixture calculated with the simplified weighted mean from the values calculated with the Wassiljeva's mixture formula.	39
4.4	Percentage deviation of the density of the two types of stainless steel used for the hybrid power plant at DLR from the values at ambient temperature	40
4.5	Hybrid power plant 3D drawing.	41
4.6	Schematic representation of the two-dimensional model	43
4.7	Schematic representation of the one-dimensional model	44
4.8	Schematic representation of the zero-dimensional model with two materials.	45

List of Figures

4.9	Algorithm implemented in MATLAB for the computation of heat losses of an insulated tube.	46
4.10	Algorithm implemented in MATLAB for the computation of heat losses of an insulated tube with the use of the DLR in-built multi-dimensional solver	47
4.11	Representation of the neutral surfaces in a tube with two layers. . .	49
4.12	Percentage deviation of the computational time spent in the calculation of the thermo-physical properties with and without Horner’s method.	52
4.13	Calculation of Darcy friction factor with different methods: (a) percentage deviation from the Colebrook-White equation, (b) influence on the computational time.	53
4.14	Percentage deviation of the heat loss calculated with different values of emissivity to simulate its dependence on temperature.	54
4.15	Reformer with insulation.	55
4.16	Reformer (REF) schematic representation	55
4.18	(a) Recirculation modeled as an adiabatic compression with after-cooling. (b) Recirculation modeled as a non adiabatic compression.	57
4.19	Percentage deviation of outlet temperature and mechanical power of the recirculation blower between the two modeling strategies. . .	58
4.20	Heat exchanger.	60
4.21	Heat exchanger schematic representation	60
4.22	Influence of insulation thickness on secondary circuit outlet temperature and heat loss	61
4.23	Burner with a single-can layout	62
4.24	Burner (BUR) schematic representation	62
4.25	3 kW Micro Gas Turbine studied at the Institute of Combustion Technology at DLR.	63
4.26	Gas turbine (TUR) schematic representation	63
4.27	Percentage deviation of outlet temperature and mechanical power of the gas turbine between the two modeling strategies.	64
4.28	SOFC Stack Modules for the hybrid power plant at DLR	65
4.29	SOFC Stack Module schematic representation. Heat is directly lost from the bottom of the stacks to the Sensor Compartment (\dot{Q}_{SEN}) and from the other sides to the pressure vessel’s fresh air (\dot{Q}_{VES}). .	66
4.30	Open pressure vessel during fabrication.	67
4.31	Sketch of the pressure vessel’s inside, considered as a set of flat plates.	67

List of Figures

5.1	Distribution of temperature in two different cross-sections (beginning and end) of a test tube.	70
5.2	Distribution of temperature in the radial direction at the beginning, in the middle and at the end of the tube.	71
5.3	Percentage deviation of the maximum temperature difference along the tube	72
5.4	Deviation between the results of the 2D and 1D models with varying insulation thickness.	72
5.5	Comparison of the outlet temperature (a) heat loss (b) and computational time (c) of a test tube with different model approaches. . .	74
5.6	Percentage deviation of outlet temperature (a) and heat loss (b) with varying insulation thickness: comparison of different 0D models in respect of the 1D model.	76
5.7	Deviation between the results obtained using arithmetic mean and logarithmic mean as gas mean temperature for different values of insulation thickness.	77
5.8	Gas temperature difference between inlet and outlet: comparison of the different models with the experimental measurements	79
5.9	Gas temperature difference between inlet and outlet: sensitivity with insulation imperfection	79
5.10	Temperature of the materials over time.	80
5.11	Gas outlet temperature over time.	81
5.12	Influence of the time step on the percentage deviation of the gas outlet temperature: comparison with $\Delta t = 10$ s.	82
5.13	Influence of the time step on the percentage deviation of the material temperature: comparison with $\Delta t = 10$ s.	82
5.14	Gas outlet temperature over time: comparison of different models ($L = 10$ m).	83
5.15	Gas outlet temperature over time: comparison of different models ($L = 1$ m).	84
5.16	Hybrid power plant global model non adiabatic concept	85

List of Tables

3.1	Thermal and electrical quantities in the electrical analogy.	23
4.1	Gas species involved in the hybrid power plant simulation	37
4.2	Comparison of the computational time necessary to calculate the gas mixture properties with a the Wassiljeva's mixture formula and with the simplified weighted mean.	39
4.3	Computational time for the simulations of the recirculation blower with the two different strategies.	59
5.1	Characteristics of a test tube typical of the hybrid power plant, used to compare the different model paradigms.	69
5.2	Materials of the test tube.	69
5.3	Comparison of the results obtained with a 2D and a 1D model (radial discretization).	71
5.4	Zero-dimensional approaches.	73
5.5	Deviation of the results of the 0D models from the 1D.	75
5.6	Computational time for the simulations with arithmetic mean and logarithmic mean as gas mean temperature.	78
5.7	Characteristics of the tube used to perform experimental measurements at the Institute of Combustion Technology.	78
5.8	Heat losses from the components of the hybrid power plant as predicted by the model.	86

Nomenclature

Acronyms

Symbol	Description
0D	Zero-dimensional
1D	One-dimensional
2D	Two-dimensional
3D	Three-dimensional
ACP	Air Compressor
AMB	Ambient Atmosphere
AND	Anode
ARI	Arithmetic mean model
ASU	Air Supply
BCS	Best Case Scenario model
BFS	Burner Fuel Supply
BUR	Burner
CAT	Cathode
CFD	Computational Fluid Dynamics
CMP	Compressor
ctv	Combined transfer vector
DLR	Deutsches Zentrum für Luft- und Raumfahrt / German Aerospace Center
EGI	Electric Grid Input
EGO	Electric Grid Output
ELO	Electric Load
EXH	Exhaust
FCP	Fuel Compressor
FDM	Finite Difference Method
FEM	Finite Element Method
FST	Fuel Storage
FVM	Finite Volume Method
GEN	Generator
GT	Gas Turbine
HEX	Heat Exchanger
IEA	International Energy Agency
LOG	Logarithmic mean model

Symbol	Description	Unit
MFS	Main Fuel Supply	
MGT	Micro Gas Turbine	
MIX	Mixer	
NFD	Neutral Face Discretization model	
REC	Recirculation	
REF	Reformer	
SEN	Sensor Compartment	
SEP	Separator	
SOFC	Solid Oxide Fuel Cell	
SSM	SOFC Stack Module	
TT	Institut für Technische Thermodynamik / DLR Institute of Engineering Thermo- dynamics	
TUR	Turbine	
Txy	Tube with address xy	
VES	Pressure Vessel	
VT	Institut für Verbrennungstechnik / DLR Institute of Combustion Technology	
WCS	Worst Case Scenario model	

Constants

Symbol	Description	Unit
σ	Stefan-Boltzmann's constant	$5.67 \cdot 10^{-8} \text{ W m}^{-2} \text{ K}^{-4}$
R	Universal gas constant	$8.314 \text{ J mol}^{-1} \text{ K}^{-1}$

Greek Symbols

Symbol	Description	Unit
β	Coefficient of thermal expansion	K^{-1}
Δ	Finite difference	
ϵ	Roughness	m
η	Efficiency	1
μ	Dynamic viscosity	$Pa \cdot s$
∂	Partial derivative	

Nomenclature

Symbol	Description	Unit
Φ	Correction factor by Mason and Saxena	1
ϕ	Energy flow	W
ρ	Density	$kg\ m^{-3}$
ε	Efficiency of the heat exchanger	1
ε	Emissivity	1

Latin Symbols

Symbol	Description	Unit
ΔH_R	Reaction Enthalpy	$kJ\ mol^{-1}$
\dot{C}	Capacity rate	$W\ K^{-1}$
\dot{H}	Enthalpy flow	W
\dot{m}	Mass flow	$kg\ s^{-1}$
\dot{Q}	Heat flow	W
\dot{S}	Heat source	$W\ m^{-3}$
\dot{W}	Mechanical power	W
A	Area	m^2
C	Heat capacity	$J\ K^{-1}$
c	Specific heat capacity	$J\ kg^{-1}\ K^{-1}$
D	Diameter	m
d	Derivative	
E	Emissive power	$W\ m^{-2}$
e	Internal energy	$J\ m^{-3}$
F	View factor	1
f	Darcy friction factor	1
Fo	Fourier number	1
g	Gravity acceleration	$m\ s^{-2}$
Gr	Grashof number	1
h	Heat transfer coefficient	$W\ m^{-2}\ K^{-1}$
I	Electric current	A
k	Thermal conductivity	$W\ m^{-1}\ K^{-1}$
L	Length	m
M	Molar mass	$g\ mol^{-1}$
Nu	Nusselt number	1
p	Pressure	Pa

Nomenclature

Symbol	Description	Unit
Pe	Peclet number	1
Pr	Prandtl number	1
q	Heat flux	$W\ m^{-2}$
R	Resistance	$K\ W^{-1}$
r	Coordinate along the radial direction	m
Re	Reynolds number	1
T	Temperature	K
t	Thickness	m
t	Time	s
u	Speed	$m\ s^{-1}$
V	Electrical potential	V
V	Volume	m^3
X	Molar fraction	mol/mol
x	Coordinate along generic axis x	m
Y	Mass fraction	g/g
y	Coordinate along generic axis y	m
z	Coordinate along the axial direction	m

Superscripts

Symbol	Description
n	Generic time-step n
'	Sub-model input
''	Sub-model output
0	Standard State: $T^0 = 273.15\ K,$ $p^0 = 101325\ Pa$

Subscripts

Symbol	Description
∞	Undisturbed fluid
i	Generic element i
a	Ambient condition
B	Boundary node
b	Blackbody

Nomenclature

Symbol	Description	Unit
c	Characteristic	
c	Cold fluid	
cnd	Conductive	
cnv	Convective	
E	East node	
e	Electrical	
fluid	Fluid	
gas	Gas	
h	Hot fluid	
in	Inlet	
ins	Insulation	
is	Isentropic	
l	Heat loss	
max	Maximum value	
min	Minimum value	
N	North node	
out	Outlet	
P	Generic node	
p	Constant pressure	
rad	Radiative	
S	South node	
surf	Surface	
tbs	Tubes	
th	Thermal	
tot	Total	
tube	Tube	
W	West node	

1 Introduction

According to the International Energy Agency (IEA), an increase in energy demand is to be expected in the next years, together with a further spread of renewable energy devices [26]. This is progressively leading to a change in the configuration of the global energy system, from a concentrated to a distributed one. This requires low-size power generation devices instead of traditional power plants. These applications' efficiencies, though, are not comparable with the biggest plants' ones, due to small scale and simplified configuration. Furthermore, the growing penetration of the renewable energy sources has introduced the problem of aleatory and discontinuous power supply, that is unable to properly follow the energy demand curve.

Therefore, a power plant with the characteristics of reliability, efficiency and modularity can be very helpful in the depicted scenario. A Solid Oxide Fuel Cell/Gas Turbine (SOFC/GT) hybrid power plant meets all these requirements and becomes a promising new technology for providing electrical energy in stationary applications.

First of all, a SOFC/GT hybrid power plant can provide higher efficiencies than those of the single components, being expected to reach an electrical efficiency of about 70% [49, 25]. In this way, pollutant emissions and environmental impact are likely to be reduced.

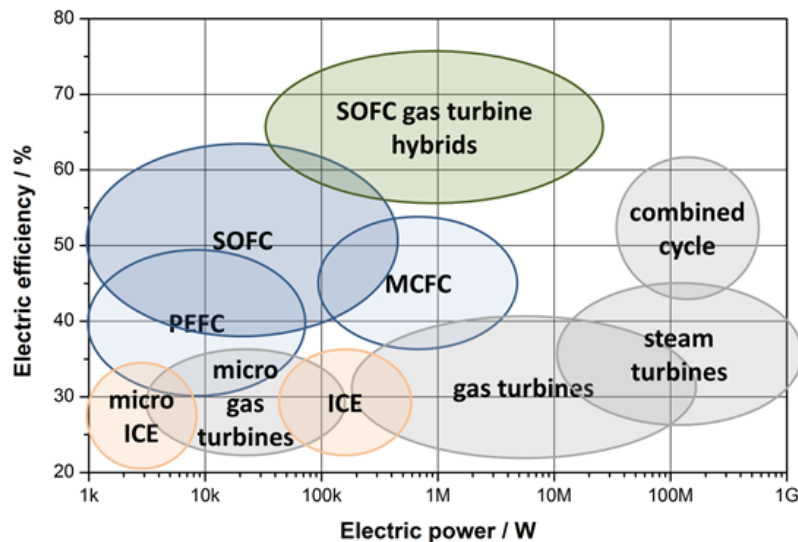


Figure 1.1: Comparison of electrical efficiencies of different power plant types [24].

Fuel flexibility is another advantage of a SOFC/GT hybrid power plant, since this can be operated with different gaseous hydrocarbons fuels plus hydrogen. In the attempt to reduce the use of fossil fuels as energy sources, it is still impossible, in the closest future, to build a scenario in which traditional fuels have been eliminated. In particular, natural gas will remain an essential energy source [26]. Due to its ability to run with different types of fuels including renewable gases, the SOFC/GT hybrid power plant can be relied on as one of the bridge technologies in the transition from fossil fuels to whichever future developments.

Furthermore, unlike the renewable energy resources, a SOFC/GT hybrid power plant is able to guarantee security in power supply, as long as a stream of fuel is provided. The possibility of operating the power plant far from nominal power output while maintaining a high efficiency and the low inertia in changing regime make the power plant suitable for integration with renewable energy sources. For instance, power output can be easily and quickly reduced in presence of a peak in energy production from renewable energy sources, providing a way to swiftly adjust to follow the load demand [2].

Hence, high efficiency, fuel flexibility, operational stability and part-load good performance are the basic aspects that make the SOFC/GT hybrid power plant an interesting field of research.

1.1 Motivation

The present work has been made in collaboration with the research organization DLR (Deutsches Zentrum für Luft- und Raumfahrt - German Aerospace Center), where the project of a demonstration hybrid power plant consisting of a SOFC and a Micro Gas Turbine (MGT) with an overall electric power of around 30 kW is being developed. The prototype power plant is currently under construction and the first operation is expected in late 2017.

The operation of the system is still being investigated by researchers in the Institute of Engineering Thermodynamics (TT - Institut für Technische Thermodynamik). In order to understand the potential of the hybrid power plant and predict its performance and possible operating strategy, an adiabatic model of the overall system has been created.

However, the operating temperature of a solid oxide fuel cell is 950-1125 K and neglecting the system energy losses could lead to an overestimation of the hybrid power plant operating range. Furthermore, temperature gradients are of primary importance in this system, due to the limitations of the materials composing the

fuel cell stacks. Therefore, being able to predict the distribution of temperature in the system is vital for a safe starting process and operation.

In this context, the scope of the present work is to produce a model of the system's heat losses that can be integrated in the overall system model, in order to perform simulations of the hybrid power plant in a more accurate way. It is possible, then, to foresee and prevent severe damages that might occur in the materials if the temperature limitations are not respected.

Moreover, the thermal capacity of the materials composing the system (i.e. tubes and insulation) could be of use as thermal storage during the transient processes of the operation of the hybrid power plant. This possibility can be investigated with the help of a process simulation that includes a precise thermal behavior.

To reach this goal, different modeling strategies will be evaluated. The model that provides the most successful accuracy-computational speed ratio will be considered for further system simulations.

1.2 Outline of the Thesis

The present thesis is divided in four main Sections.

In Section 2, the state of the scientific and technological knowledge regarding the SOFC-GT hybrid power plants and the possible multidimensional models is described. Special attention is paid to the scientific literature outline of the different modeling strategies used for simulating various physical systems. Thus, a first look at the analysis that must be conducted is given.

In Section 3, the theoretical fundamentals that have been referenced to for the present work are illustrated: firstly the theory of heat transfer, essential for calculating the heat losses from a high temperature system such as a SOFC-GT hybrid power plant and, secondly, the computational techniques for implementing and evaluating such heat losses by means of a commercial software.

In Section 4, the various multi-dimensional models of heat losses are depicted. Particular attention is paid to the implementation of thermo-physical properties of the materials involved in the power plant. Since the temperature range can be very broad, the dependence from temperature of each property must not be neglected. Furthermore, the application of the model created to the components of the hybrid power plant at DLR is discussed.

In Section 5, the results of the simulations performed with the different models are evaluated, in order to understand the best accuracy-computational speed ratio.

The related model can therefore be integrated in the overall system model for providing a better understanding of the operation of the SOFC-GT hybrid power plant.

Eventually, the conclusions of the present work are drawn and the future developments are discussed.

2 State of the Scientific and Technical Knowledge

This Section contains a description of the current scientific knowledge regarding the topics of this thesis, including the analysis and characterization of a SOFC/GT hybrid power plant. Hence, the technical gaps that might be filled with further studies can be identified and understood.

Firstly, a review of the concept and the various models created for analyzing a SOFC/GT hybrid power plant is made, in order to understand the developments that are still required.

Then, the possible multi-dimensional model approaches to heat transfer and heat losses from a physical system are summarized.

2.1 SOFC/GT Hybrid Power Plant Concept

A SOFC-GT hybrid power plant is a system made of two major components: a high temperature fuel cell and a gas turbine engine.

2.1.1 Fuel Cell

Fuel cells are electrochemical devices that convert the chemical energy of a fuel directly into electrical energy, without the need for a combustion to occur nor a mechanical-electrical conversion.

The basic components of a fuel cell are two electrodes, called anode and cathode and an electrolyte separating them. Fuel containing hydrogen is supplied to the anode while oxygen available in the atmosphere is supplied to the cathode.

Here, the operation and characteristics of the specific fuel cell used at DLR are described. Oxygen is electrochemically reduced on the cathode surface: oxygen ions are produced and pass through the electrolyte. Hydrogen is electrochemically oxidized on the anode surface: hydrogen ions react with oxygen ions to form water, while the released electrons flow through an external load to the cathode to complete the electrical circuit.

The chemical reactions occurring into the fuel cell are shown in the following (2.1).

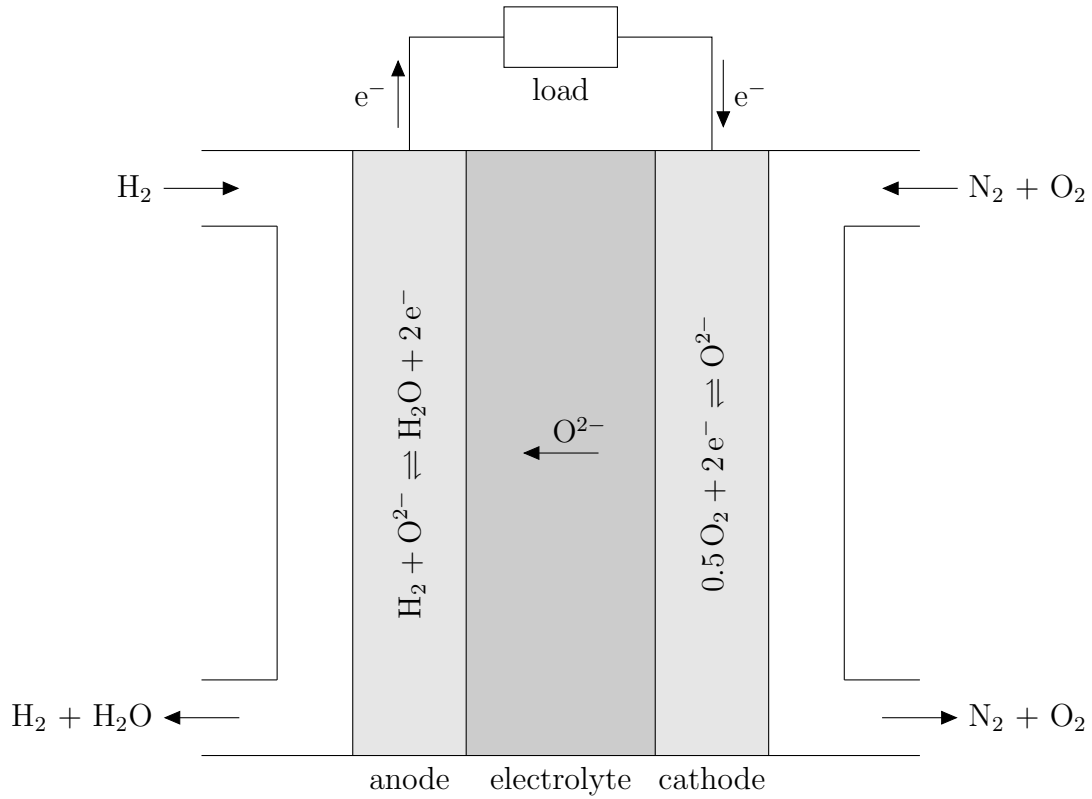
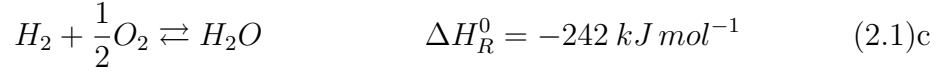
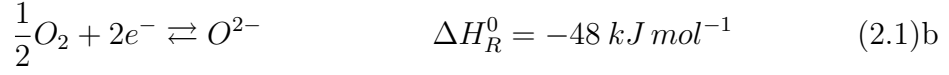


Figure 2.1: Schematic representation of the type of solid oxide fuel cell used at DLR [22]. Oxygen ions are formed at the cathode and conducted through the electrolyte. The ions react with hydrogen at the anode and form water. Electrons flow through an external electrical load.

The different types of fuel cells are distinguished through the electrolyte material. A suitable fuel cell type for coupling with a gas turbine engine is the solid oxide fuel cell (SOFC), due to the higher operating temperature (950-1125 K) that can be beneficial for the gas turbine.

The electrolyte of the SOFC used at DLR is made of a ceramic material that can not bear large temperature differences between the inlet and the outlet. Several

materials are under investigation to improve that behavior. Nonetheless, this has to be taken into account during the project and the operation of the system.

There are three major design types of SOFC: tubular, planar and monolithic. As a single cell usually produces a voltage of about 1 V, typical power supply applications are designed as stacks made of several groups of electrically connected fuel cells, in order to obtain a more useful voltage.

In order to being able to operate SOFCs with fuels different from pure hydrogen and therefore to guarantee fuel flexibility, a reforming process is required. In SOFC systems, steam reforming is a suitable reforming type, since the necessary steam can be provided by recirculating anode off gas [22]. In the case of methane, the steam reforming reaction mainly occurs in the two following steps:



The process is highly endothermic. The necessary heat for the reaction can be supplied, together with the steam, through the recirculation of the anode off gas.

For the pilot hybrid power plant project at DLR, the SOFC Stack Module (SSM) is made up of six insulated compartments, each composed by two towers of stacks. This kind of predefined design, that is part of a mass production line, forms an imperfect insulation system that needs to be accounted for in the modeling process. In fact, insulating each compartment separately increases the surface and the volume of the module without adding benefits.

2.1.2 Gas Turbine

Gas turbines are a type of internal combustion engine (Figure 2.2). Air is compressed by a compressor and heated inside a combustion chamber, where a fuel is supplied, until a high pressure - high temperature thermodynamic state is reached. Then, air is expanded through a turbine and released in the ambient. Therefore, enthalpy contained in the pressurized and hot air flow is converted into mechanical energy which is in its turn converted into electrical energy through a generator.

A suitable gas turbine configuration for coupling with a fuel cell is a Micro Gas Turbine (MGT). In fact, SOFC needs preheated air as cathode inlet flow. A large multistage gas turbine is optimized to use as much off gas enthalpy as possible, therefore giving a low exhaust temperature, while a MGT allows to obtain a high temperature exhaust flow that can be used in a heat exchanger for preheating air. This can be then supplied to the SOFC.

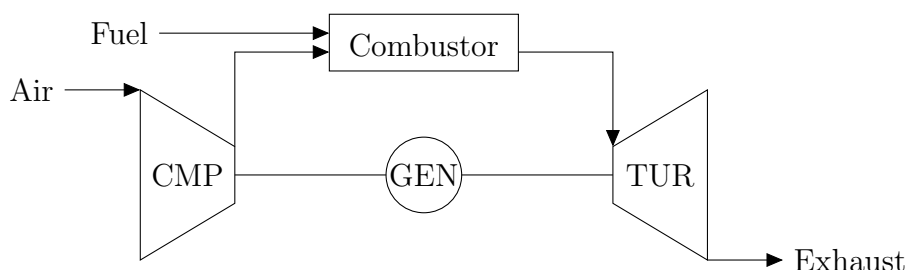


Figure 2.2: Schematic representation of a gas turbine. Air is compressed by the compressor (CMP), heated inside the combustor and expanded through the turbine (TUR), which drives both the compressor and the electric generator (GEN).

Plus, the DLR pilot hybrid power plant is designed with the relatively small size of 30 kW, which matches well with a MGT.

2.1.3 Hybrid Power Plant

The general concept of a hybrid power plant is to combine two or more different power generation devices in order to increase the efficiency, flexibility or energy output of the devices considered separately.

In a SOFC/GT hybrid power plant, a solid oxide fuel cell and a gas turbine work in synergy to enhance fuel to electricity efficiency, due to their complementary behavior (Figure 2.3).

For this purpose, the combustion chamber of the gas turbine is preceded by a SOFC so that it is possible to take advantage of the fuel cell's higher electrical efficiency. Furthermore, there always must be unconsumed fuel in the exhaust of the fuel cell, in order to assure that every cell is constantly provided with fuel. Due to electrochemical reasons, fuel starvation is highly forbidden, otherwise the cell is subjected to an irreversible degradation process [9, 40]. The fraction of fuel that can not be converted inside the fuel cell and would be wasted in a separated SOFC is instead supplied to the turbine together with the SOFC exhaust hot gases. In this way, the waste products of the SOFC become the inlet gas flow for the gas turbine, thus furnishing additional electricity. Furthermore, the residual enthalpy in the gas flow exiting the turbine can be employed to preheat the air to the cathode. The fuel cell must be pressurized in order to achieve the difference of pressure required for the operation of the turbine. Nonetheless, it is known that a SOFC operated with pressurized air and fuel has a better performance than one

operated at atmospheric pressure [52, 22].

To resume, the coupling of the two systems working in a good symbiotic fit is advantageous as:

- Preheated air from the turbine off gas is furnished to the cathode;
- The fuel cell off gas can be expanded in the gas turbine to give additional electricity;
- Unconsumed fuel is reused to provide additional energy to drive the gas turbine;
- The required pressurization can be beneficial for the fuel cell efficiency. It is provided due to the presence of the compressor driven by the gas turbine.

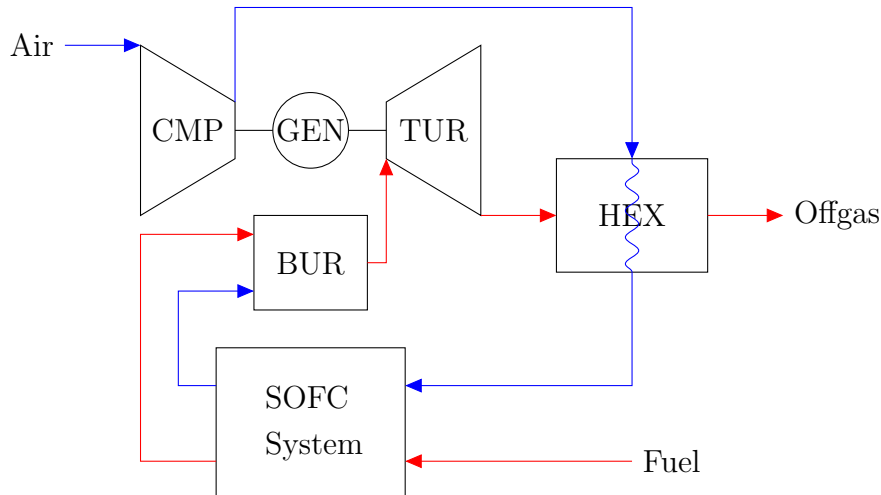


Figure 2.3: Schematic representation of a hybrid power plant made by a SOFC system and a gas turbine [44].

The DLR design for the prototype system considers a directly coupled SOFC/GT hybrid power plant: the configuration is constituted by a direct pressurized cycle with anode recirculation. For this purpose, the SOFC stack modules, the reformer and the relative connecting pipes are placed inside a pressure vessel. Air is compressed by the air compressor and led to the pressure vessel where it is heated up by means of the thermal loss from the high temperature fuel cell stacks. The vessel air is further heated in a heat exchanger and then set to the cathode.

In the mean time, the fuel containing hydrogen is compressed and taken into the pressure vessel, where it is mixed with hot recirculating anode gas. This is followed

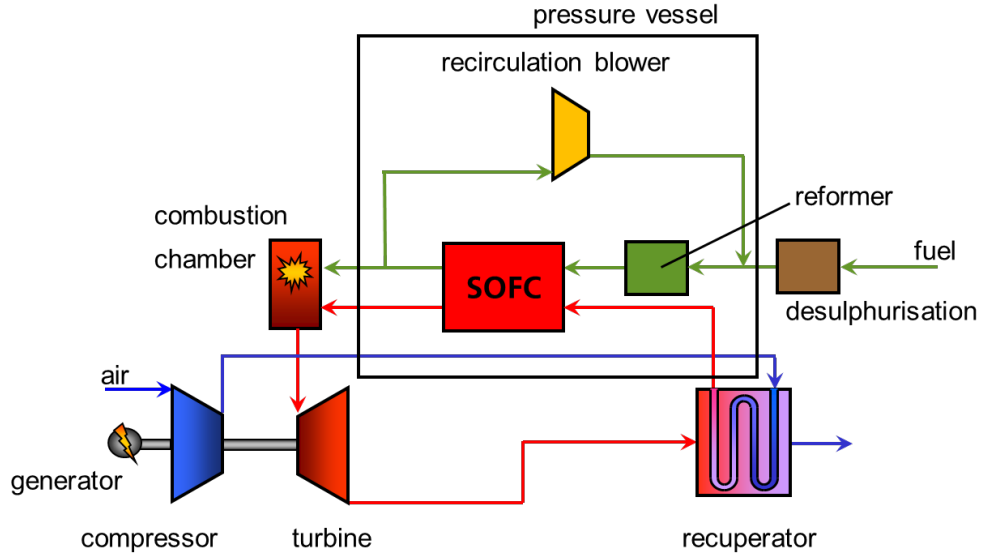


Figure 2.4: Schematic representation of the configuration used at DLR for the prototype SOFC/GT hybrid power plant [23]. The SOFC stack modules, the reformer and the recirculation blower are placed inside the pressure vessel.

by the steam reforming process (Eqs. (2.2)) and the fuel cell reactions (Eqs. (2.1)). The steam reforming is necessary to guarantee the operation with fuels different from hydrogen. Consequently, a recirculation blower is strictly required: steam is a product of the fuel cell, so a fraction of the anode off gas is recirculated to the reformer to allow the steam reforming. The recirculation ratio can be varied to investigate its effect on the performance of the system.

The remaining part of the anode and the cathode exhaust gases are led into the combustor where they are burned. Additional fuel can be added to the combustion process. The hot products of the combustion chamber are expanded in the MGT turbine and, before being released into the ambient, preheat the vessel air by means of the heat exchanger. This final stage enables to recuperate the thermal energy of the turbine outlet flow to raise the temperature of the air provided to the SOFC cathode.

At the bottom of the pressure vessel a sensor compartment is located. The measuring equipment for the thermo-physical parameters of the processes must be kept at a temperature lower than 100 °C to avoid the break-down of the devices.

Additional systems, such as a set of equipment for fuel processing composed of a desulphurizer and a fuel compressor, are included in the design.

2.2 Hybrid Power Plant Modeling

The interest in SOFC/GT hybrid technology was sparked in 2000, when Siemens built and tested a 220 kW hybrid power plant at the University of California, obtaining an electrical efficiency of 52% [27, 49]. Therefore, during the past years, many research groups worldwide, a few of which with real test rigs, have been studying and improving the concept and the application of this technology, producing a large number of publications. The literature regarding the topic has been classified and summarized, from both numerical and experimental points of view, by Buonomano et al. [10].

In particular, the most important research institutions that have been conducting extensive studies on the SOFC/GT are the University of Genoa (Italy) in cooperation with Rolls-Royce Fuel Cell Systems, today LGFCS (UK and USA), the Korea Institute of Energy Research, the National Energy Technology Laboratory (USA) and the German Aerospace Center (DLR).

In scientific research, it is advantageous to have available reliable models that can validly substitute experimental tests and predict operating characteristics of systems under different conditions. Several global system models have been used by the above mentioned research groups especially for increasing the knowledge concerning cycle layout, control strategies and part-load dynamics [19, 17, 29].

DLR is currently working on the realization of a hybrid power plant with an electrical power output of around 30 kW [22]. At the present moment, both modeling and experimental studies are being conducted [29, 45, 52, 22]. A number of possible system configurations for coupling SOFC and GT as well as the DLR preferred one, based on a pressurized cycle, are described by Leucht et al. [29, 28]. The importance of pressurization of the SOFC for performance enhancement and durability has been discussed by Henke in his PhD thesis [22]. The author's final conclusions about the operating range of the hybrid power plant are based on modeling and simulations performed on system level.

But Leucht's [29, 28] and Henke's models [22] do not consider a reliable accounting for energy losses of the system and system's components. In the former, only heat exchange between fuel cell and reformer is modeled, while in the latter heat transfer is calculated only in the SOFC section.

Besides, publications by research groups other than DLR, describing exergy and energy analysis of hybrid power plants, do not provide details on energy losses. Calise et al. [12, 14, 13, 15] investigate design and partial load operation with the general assumptions of steady-state process and absence of heat losses towards the

environment. Barelli et al. [3] consider a thermal loss equal to the 10% of the heat exchanged in the heat recovery section, still no further consideration is made. In a successive study by the same research group [4], a complete dynamic model of the hybrid system, based on the previously analyzed stationary situation [3], is presented. The scope of the work is the optimization of the plant's components through the examination of their transient response and dynamic interaction. But the models of the components lack of a precise calculation of heat transfer to the exterior. Similarly, Wu et al. [53] propose a thermal dynamic modeling of the temperatures occurring in a SOFC/MGT plant, but heat capacities of reformer and fuel cell stacks only are considered. No attention is drawn to the thermal behavior of the other components.

Lastly, in [8] and [41] Brower considers the 220 kW pressurized SOFC/GT hybrid power plant tested at the National Fuel Cell Research Center. Experimental data from the start up process of the system are compared with the results of a dynamic simulation. The author concludes that the dynamic and steady-state performance predictions of the model are remarkable, given the system complexities. Nonetheless, it is clearly affirmed that the model predicts higher temperatures due to inadequate accounting of heat losses throughout the system. Additional work is required in order to accurately quantify heat losses and temperatures associated with the elements composing the plant.

The reasons why a precise accounting for heat losses from the power plant is required in both stationary and transient operation have been highlighted in [8] and in Section 1.1. Such a detailed analysis has not been provided in any other previous work.

In the light of these considerations, further studies are being conducted at DLR, in order to fill this void in technical literature. A new and detailed global system model for the prediction of stationary and transient operation of the demonstration plant has been created. More details regarding this global model concept are given further on in the present thesis (Figure 4.2). In-cooperating the system's heat losses and capacities increases the resolution of this prediction.

In the mean time, it is necessary to maintain a high computational speed, in order to being able to evaluate a broad range of operation possibilities and analyze multiple operating strategies in a short time.

2.3 Multi-dimensional Heat Transfer Modeling

The focus of this work is modeling heat transfer from a SOFC/GT system.

First of all, a description of the multi-dimensional heat transfer model paradigms used in literature for analyzing various physical systems is required. This can be a starting point for understanding the details of the model implementation and the analysis explained in the following Sections.

The usual steps in the development of a numerical model, as it is clearly summarized by Bove and Ubertini in [6], are:

1. The mathematical model: the physical system is understood and translated into mathematical equations, that cannot be usually analytically solved;
2. The numerical model: the equations are discretized and the physical domain is divided into small elements constituting the grid, to allow numerical solution;
3. Boundary conditions: a set of problem-dependent boundary and initial conditions are specified;
4. Simplification of the problem, according to the specific needs of the model and the application. In particular, different approaches regarding the geometry of the problem can be used:
 - (a) Three-dimensional approach (3D): this is used when detailed information on the distribution of variables in the physical domain is required and no geometrical dimensions are neglected. Such problems are usually solved by means of a 3D FEM commercial software and can be very complex and time-consuming;
 - (b) Two-dimensional approach (2D): in this case, one geometrical dimension can be neglected and the system can be reduced to a 2D domain;
 - (c) One-dimensional approach (1D): the assumption is made that the variation of physical properties along two spatial directions is negligible;
 - (d) Zero-dimensional approach (0D): a zero dimensional model is also called box model or lumped model. Spatial variations are not taken into account and mass and energy balances allow to obtain output variables from input ones. Box models are usually employed when the attention is not focused on a single component but on an entire system's performance.

5. Validation of the model: once a model has been developed for a particular application, the results are compared with physical reality;
6. Presentation of results and simplified application.

The above explained scheme can be applied to the computational modeling of any physical system and the preferred approach depends on model requirements and goals.

The selection of the appropriate dimensionality in a model representation, from 0D to 3D, depends on the aim and on the required accuracy of the research study. Zero-dimensional, or lumped parameter, models assume a uniform distribution of the fundamental variables within any particular compartment of the model at any instant in time, whilst the higher dimensional models recognize the variation of these parameters in space [46]. The decision is also driven by the availability of proper boundaries, as no 3D model can give an extended results quality when boundaries can not properly be defined.

Hence, multi-dimensionality (2D or 3D) is recommended, for instance, in modeling thermo-mechanical effects, where geometry, material homogeneity and load distribution of the problem require appropriate attention [39].

On the other hand, where spatial distribution of parameters is not strictly required, the simplified zero-dimensional approach is used in order to save computational time while maintaining an acceptable accuracy in the overall plant performance evaluation [6].

Many studies that model single components, from internal combustion engines to fuel cells, with a 0D approach state that the results of the simulations are acceptable and the zero-dimensional models are fast and reliable allowing for the simulation of many different situation in a short time.

In literature, the concept is widely applied, for instance, to internal combustion engines. Abbe et al. [34] declare that, although there exists a multitude of models for diesel engines, 0D phenomenological models, validated with experimental results, present the advantages of giving fast and accurate computed results. The same is written by Cruz et al. [18]: components such as torch-ignited engines are usually researched by CFD or FEM analysis, but a zero-dimensional code provides a low-cost and useful insight on the way operating conditions affect engine's performance. Furthermore, Payri et al. [38] present the results of a 0D thermodynamics model that takes into account heat transfer, for an internal combustion engine, showing a good capability for accurate predictions of the thermodynamic variables in the system.

In [31] a 0D/1D code for an internal combustion engine is built. A one-dimensional approach is used for describing the flow inside pipes and manifolds, due to the relevance of gas dynamics effects in those elements. Instead, the remaining components and phenomena including heat transfer are modeled by 0D models with a high computational efficiency. On the other hand, multi-dimensional models provide a considerable amount of spatial information but are not appropriate for sensitivity analysis or optimization purposes, due to computational time and storage constraints. Plus, such an accuracy in the distribution of parameters might not be required by the scope of the project.

Moreover, a high number of articles studying the application of the 0D concept to other diverse physical systems involving heat transfer are accessible in literature.

Nguyen et al. [35] study a lumped parameter concept for convective and conductive heat transfer in droplets evaporation. In [43] the lumped heat transfer model is applied to a nuclear reactor simulation where fastness of solution is a matter of concern. Again, Bove et al. [7] reduce a micro-detailed SOFC model to a macro-black-box one, including heat transfer occurring in the system. They emphasize that, when the main purpose of the model is to provide the fuel cell performance, in order to analyze the whole system, the variables variation along the cell are not relevant.

In most of these publications, a comparison with other approaches and models is made and the results obtained with the 0D assumptions are found satisfactory in terms of accuracy, algorithm simplicity and computer cost.

In a different way, Carnogurská et al. [16] determine heat losses from the pipes of a distribution network with a simpler method based on dimensional analysis. The dimensionless criteria that describe heat losses, though, are determined from direct measurement for limited cases and variable ranges. Whereas reliable experimental values are not available, as in the case of DLR hybrid power plant's components, this procedure should not be considered.

It is clear that modeling heat transfer is a significant part in the major part of physical systems studied in literature. This is now applied to each components of a SOFC/GT hybrid power plant, in order to understand and integrate energy losses in the global system.

It is once again of great importance to highlight the need for a balance between model's accuracy and computational speed. A fast global system simulation allows to investigate, in a short time, many different stationary points as well as transient behaviors. Hence, it is possible to predict operating ranges and strategies for the exercise of the SOFC/GT hybrid power plant at DLR.

2. State of the Scientific and Technical Knowledge

The attempt to build a set of models that are able to predict heat losses from the system's components in various operating conditions, with a feasible accuracy and a low computational time, is described later in the present work (Sections 4 and 5).

3 Theoretical Fundamentals

This section contains the basic theory of analytical and computational heat transfer. The description of the physical mechanisms and equations that regulate heat transfer processes is followed by an outline of the computational techniques and algorithms that can be used for solving complex situations for which an analytical solution cannot be provided.

This gives an understanding of the modeling strategies adopted and described later in this work.

3.1 Heat Transfer

According to a definition given by Özisik [36, p. 1], the energy given up by the constituent particles such as atoms, molecules, or free electrons of the hotter regions of a body to those in cooler regions is called *heat*. The different types of heat transfer mechanisms are referred to as modes. The three basic modes of heat transfer are conduction, convection and radiation.

3.1.1 Conduction

Conduction is the mode of heat transfer in which energy exchange takes place in solids or in fluids in rest, from the region of high temperature to the region of low temperature, due to the presence of a temperature gradient in the body.

Once the temperature distribution T within a body is determined as a function of position and time, then the heat flow in the body is readily computed from the laws relating heat flow to the temperature gradient.

The basic law that gives the relationship between the heat flow and the temperature gradient is the Fourier's law of heat conduction:

$$q = -k\nabla T \tag{3.1}$$

The vector q is the heat flux, representing heat flow per unit of time and per unit of area. The heat flux is normal to the isothermal surface of the body, as the temperature gradient. The negative sign means that the direction is the one of the decreasing temperature.

k is called the thermal conductivity of the material and is a positive scalar quantity. The thermal conductivity of the material varies with temperature and controls the rate of heat flow in the medium. Therefore, in the analysis of heat conduction, it's very important to evaluate the property for each material correctly.

For most materials, thermal conductivity increases with increasing temperature. Among the materials with the highest values of thermal conductivity, pure metal can be identified. Insulating materials have lower values compared to the other solid materials, since their purpose is to reduce heat flow.

The description of how thermal conductivity of materials has been calculated in the present work is given in Section 4.1.

3.1.2 Convection

Convection is the mode of heat transfer affected by the flow of fluids, therefore it is strictly linked to fluid mechanics. If the fluid motion is induced by a pump, a blower or some similar device, the process is called *forced* convection. If the fluid motion occurs as a result of the density difference produced by the temperature gradient, the process is called *free* or *natural* convection.

The velocity and thermal fields are strictly linked and should be simultaneously solved, in order to calculate the convective heat flow. This is an incredibly complex problem that can be solved only in simple cases or with numerical methods. Therefore, in the study of convective heat transfer, experimental analysis on physical models is essential. Generalization of empirical results is achieved through dimensionless numbers that characterize the fluid's conditions.

Typically, convection concerns heat transfer between a solid surface and a fluid in motion compared to it. The relationship between heat flow and the difference of temperature between the two interested parts is called Newton's law of cooling:

$$q_{\text{cnv}} = h (T_s - T_{\text{fluid}}) \quad (3.2)$$

$$\dot{Q}_{\text{cnv}} = hA (T_s - T_{\text{fluid}}) \quad (3.3)$$

where h is called convective heat transfer coefficient, T_s and T_{fluid} are the temperatures of the surface and the fluid respectively and A is the wet surface. The heat transfer coefficient is not a thermo-physical property of the fluid, but an operative coefficient that depends on:

- geometry of the problem;
- characteristics of the motion (i.e. fluid velocity);
- thermo-physical properties of the fluid.

The heat transfer coefficient can be evaluated for each case by means of the non-dimensional analysis.

The Nusselt number Nu represents the ratio between convective and conductive thermal fluxes in the fluid:

$$Nu = \frac{hL_c}{k} \quad (3.4)$$

Nu is given by heat transfer correlation that were derived by experimental analysis and empirical considerations on the basis of non-dimensional groups, as stated previously. For forced convection:

$$Nu = f(Pr, Re) \quad (3.5)$$

while for natural convection:

$$Nu = f(Pr, Gr) \quad (3.6)$$

where:

$$Re = \frac{\rho u_\infty L_c}{\mu} \quad (3.7)$$

$$Pr = \frac{c_p \mu}{k} \quad (3.8)$$

$$Gr = \frac{g\beta(T_{\text{surf}} - T_\infty)\rho^2 L_c^3}{\mu^2} \quad (3.9)$$

Re is the Reynolds number and represents the ratio between inertial and viscous forces in the flow. Therefore, it defines the motion regime: high Reynolds numbers indicate a turbulent flow due to the predominance of the inertial forces, while low Reynolds numbers give a laminar flow (i.e. $Re < 2000$ for ducts).

Pr is the Prandtl number, dependent only on the fluid and its state.

Gr is called Grashof number and is used exclusively in natural convection, when gravity forces play a big role in the fluid motion.

The other quantities involved are:

- k thermal conductivity of the fluid, already defined in Section 3.1.1;
- ρ density of the fluid;
- μ dynamic viscosity of the fluid;
- u_∞ undisturbed fluid's speed;
- c_p specific heat at constant pressure of the fluid;
- g gravity acceleration;
- β coefficient of thermal expansion of the fluid, equal to $1/T$ for an ideal gas;

- T_{surf} surface temperature;
- T_{∞} undisturbed fluid's temperature;
- L_c characteristic length of the problem. The characteristic length is equal to the internal tube diameter, while for a flow along a flat plate it is equal to the length of the plate in the direction of the fluid flow.

The physical quantities must be evaluated at the film temperature, that is the mean between surface temperature and gas undisturbed one, due to the presence of the thermal boundary layer. The assumption of fully developed velocity and thermal profiles is made. More information on these mechanisms, that go beyond the scope of the present work, can be found in specific texts available in literature [5, p. 30], [42, p. 1.6].

Also a large number of heat transfer correlation for Nu can be found in literature. Those that have been considered for this analysis are here resumed.

Forced flow inside ducts

In laminar regime inside tubes, for $Re < 2000$, the commonly used value is:

$$Nu = 3.66 \quad (3.10)$$

The local Nusselt number for fully developed turbulent flow inside smooth tubes can be evaluated by means of the Colburn equation, valid for $Re > 10000$:

$$Nu = 0.023 \cdot Re^{0.8} Pr^{1/3} \quad (3.11)$$

The Gnielinski correlation gives a higher accuracy and is considered valid for a broader range of Reynolds numbers (i.e $2000 < Re < 5 \cdot 10^6$):

$$Nu = \frac{\frac{f}{8} (Re - 1000) Pr}{1 + 12.7 \left(\frac{f}{8}\right)^{1/2} (Pr^{2/3} - 1)} \quad (3.12)$$

Furthermore, this correlation takes into account the roughness ϵ of the internal tube surfaces through the Darcy friction factor between wall and fluid, derivable from the Colebrook-White equation:

$$\frac{1}{\sqrt{f}} = -2 \log_{10} \left(\frac{\epsilon}{3.7D} + \frac{2.51}{Re\sqrt{f}} \right) \quad (3.13)$$

Flat plate in parallel forced flow

The averaged Nusselt number for laminar flow over a flat plate is given by:

$$Nu = 0.664 \cdot Re^{1/2} Pr^{1/3} \quad (3.14)$$

This is valid for the Reynolds' numbers up to $5 \cdot 10^5$. For higher values the flow becomes turbulent and is described by:

$$Nu = 0.037 \cdot Re^{4/5} Pr^{1/3} \quad (3.15)$$

Only the correlations for forced convection have been mentioned, as the hypothesis of forced convection is maintained for all the flows considered. This is applied especially to external flows, since the system is located inside a laboratory where fixed conditions are kept by a ventilation system.

3.1.3 Radiation

Radiation is the mode of heat transfer caused by electromagnetic waves, which are emitted by bodies by virtue of their temperature and at expense of their internal energy. All materials continuously emit and absorb electromagnetic waves, or photons, by lowering or raising their molecular energy level. The strength and wavelength of emission depend on the temperature of the emitting material.

Thus, thermal radiation does not require a medium for its transfer and is higher in vacuum. When an electromagnetic wave travels through a medium without any attenuation, the medium is called transparent, while if attenuation is complete, it is known as opaque. An opaque body that absorbs all incident radiation is called blackbody. A blackbody absorbs and emits the maximum possible amount of radiative energy and its thermal radiation is isotropic, thus it is a perfect absorber and emitter at every wavelength and for every direction.

On a macroscopic level, the calculation of thermal radiation is based on the Stefan-Boltzmann law, which relates the heat flux emitted by a blackbody to its temperature:

$$E_b = \sigma T^4 \quad (3.16)$$

where σ is the Stefan-Boltzmann constant.

Real materials don't usually act as blackbodies. The ability of a surface to emit radiation in comparison with the ideal emission by a blackbody is defined as the emissivity of the surface. Emissivity is usually a function of wavelength and of outgoing direction. A surface whose properties are independent of wavelength is

called gray, while a surface whose properties are independent of direction is diffuse, also known as Lambert surface.

In the systems analyzed in the present work, radiation is not the dominant heat transfer mode, so the assumption of gray and diffuse bodies is made, in order to simplify the computation of radiative exchange among surfaces. Under these hypothesis, the emissivity of the surfaces is:

$$\varepsilon = \frac{E}{E_b} \quad (3.17)$$

Hence, the total emissive power of a gray and diffuse surface is:

$$E = \varepsilon \sigma T^4 \quad (3.18)$$

The heat exchanged by radiation between a surface and the external ambient, considered as a black body, follows the Stefan-Boltzmann's law as well:

$$Q_{\text{rad}} = \varepsilon \sigma A F (T_{\text{surf}}^4 - T_a^4) \quad (3.19)$$

where A is the area of the emitting surface and F is the view factor. In this case, the view factor is defined as the fraction of radiation emitted by the surface that goes directly into the ambient, so it is a pure number in the interval $[0, 1]$.

Here, the view factors are considered always unitary for simplification:

$$Q_{\text{rad}} = \varepsilon \sigma A (T_s^4 - T_a^4) \quad (3.20)$$

As a matter of fact, the system analyzed is complex and made of a high number of components. The effort to compute accurately view factors between the various bodies would be worthless, as radiation is not a dominant mode of heat transfer. Moreover, the highest possible value for F leads to a slight overestimation of the radiation effects: this is beneficial in case the worst case heat losses are desired.

A further detailed description of radiation phenomena is not a purpose of the present thesis and is sent to more specific texts [33, p. 131][42, p. 7.1].

3.1.4 Thermal Resistance

In every physical system, the three modes of heat transfer are combined. The most common and intuitive way for the visualization of heat transfer in steady-state conditions is through the electrical analogy. Table 3.1 and Figure 3.1 briefly show this concept.

Table 3.1: Thermal and electrical quantities in the electrical analogy.

Thermal quantity	Electrical quantity
\dot{Q}	I
ΔT	ΔV
R_{th}	R_e

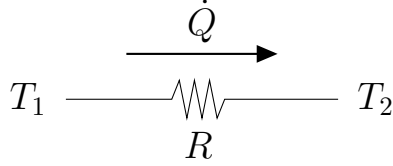


Figure 3.1: Thermal resistance.

As electrical current I is conducted through an electrical resistance R_e due to a difference of potential ΔV , heat flow is associated with a thermal resistance and is due to a difference of temperature (Eq. (3.21)):

$$\dot{Q} = \frac{T_1 - T_2}{R_{\text{th}}} \quad (3.21)$$

It is possible to obtain the thermal resistances for each of the three heat transfer modes described in Sections 3.1.1-3.1.3 as follows:

1. Conduction: Fourier's law (Eq. (3.1)) is rearranged in a one dimensional shape for a cartesian coordinate system:

$$\dot{Q} = -kA \frac{dT}{dx} \quad (3.22)$$

and compared with (3.21) to give:

$$R_{\text{cnd}} = \frac{t}{kA} \quad (3.23)$$

which is the conductive thermal resistance for a flat plate of thickness t , surface A and constant thermal conductivity k .

Similarly, in cylindrical coordinate system:

$$R_{\text{cnd}} = \frac{\log\left(\frac{r_2}{r_1}\right)}{2\pi Lk} \quad (3.24)$$

which is the conductive thermal resistance of a cylindrical shell of internal and external radius r_1 and r_2 respectively, length L and constant thermal conductivity k (Figure 3.2).

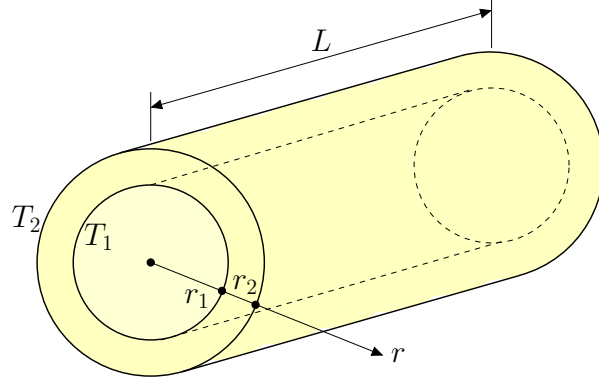


Figure 3.2: Cylindrical shell.

2. Convection: Eqs. (3.3) and (3.21) are compared to obtain the convective thermal resistance:

$$R_{\text{cnv}} = \frac{1}{hA} \quad (3.25)$$

3. Radiation can not be directly coupled to the other two modes because of its dependence on the fourth power of temperature. However, in simple passages Eq. (3.20) can be rearranged in a linear form, similar to the one of the convective heat transfer:

$$Q_{\text{rad}} = \varepsilon\sigma A (T_s^4 - T_a^4) = h_{\text{rad}}A (T_s - T_a) \quad (3.26)$$

where:

$$h_{\text{rad}} = \varepsilon\sigma (T_s^2 + T_a^2) (T_s + T_a) \quad (3.27)$$

As before, the radiative thermal resistance is obtained:

$$R_{\text{rad}} = \frac{1}{h_{\text{rad}}A} \quad (3.28)$$

Energy conservation requires that heat conduction through a wall equals the heat leaving the surface by convection and radiation. Therefore, as it is shown in Figure 3.3, it is common practice to couple radiation and convection from a surface with a total resistance, that is the parallel of the two. For a certain surface A , Eq. (3.29) is obtained:

$$R_{\text{cnv+rad}} = \frac{1}{(h_{\text{cnv}} + h_{\text{rad}})A} \quad (3.29)$$

Eventually, the steady-state analysis of heat transfer is reduced to the solution of a grid of thermal resistances. Let us take, as example, a tube of length L with a gas flowing inside and ambient air outside, represented in Figure 3.4.

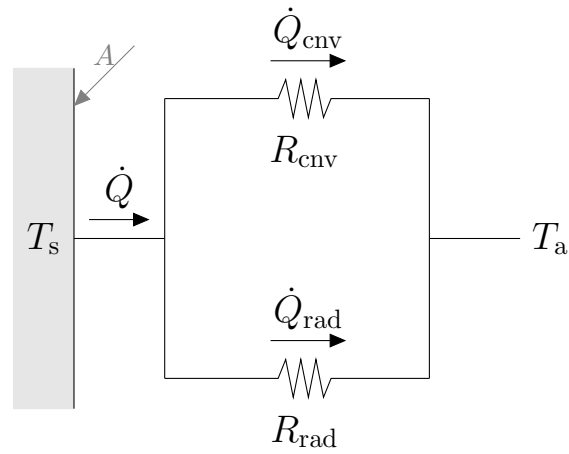


Figure 3.3: Convective and radiative thermal resistances from a surface to the ambient. The total thermal resistance is the parallel of the two.

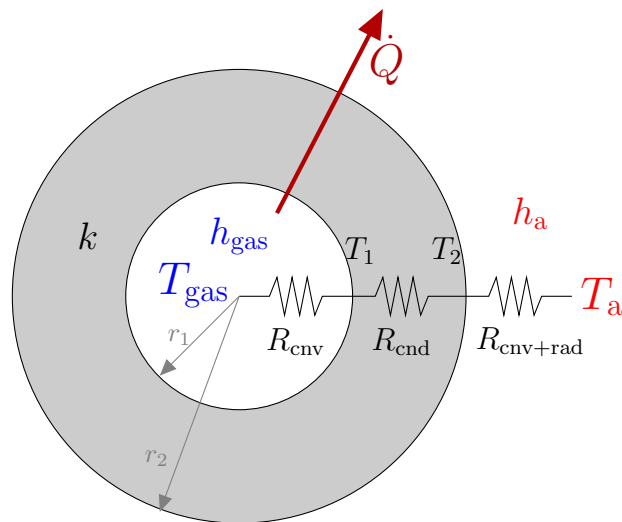


Figure 3.4: Representation of the thermal resistances of a tube with a gas flowing inside and ambient air outside. Heat flows through convection with the gas stream, conduction in the tube and convection and radiation with the external ambient.

Heat is transferred from the gas stream to the external ambient through convection with the gas stream, conduction in the tube and convection and radiation to the outside. The total resistance is the series of these three. If the tube is composed by more than one layer, each cylindrical shell gives its own conductive resistance, depending on its thickness and conductivity.

Hence, the global thermal resistance for a tube with n layers is:

$$R_{\text{tot}} = \left(\frac{1}{h_{\text{gas}} r_1} + \sum_{i=1}^n \frac{\log\left(\frac{r_{i+1}}{r_i}\right)}{k_i} + \frac{1}{h_a r_{n+1}} \right) \frac{1}{2\pi L} \quad (3.30)$$

and the total heat flow that is transferred between gas and ambient is:

$$\dot{Q} = \frac{T_{\text{gas}} - T_a}{R_{\text{tot}}} \quad (3.31)$$

In the same way, every other stationary system, with the applicable simplifications, can be solved.

3.1.5 Transient Heat Transfer

Heat transfer in non-stationary conditions is required in transient processes such as start-up, shut-down and any change in the load.

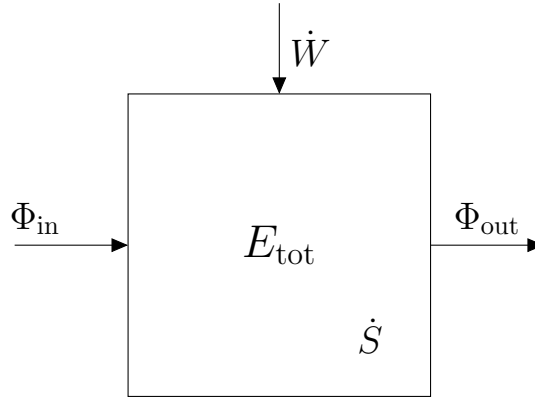


Figure 3.5: Control volume with internal energy, inlet and outlet energy flows through the boundaries, mechanical work and internal energy source.

The starting point is the principle of energy conservation applied to a generic control volume:

$$\frac{\partial E_{\text{tot}}}{\partial t} = \sum \phi_{\text{in}} - \sum \phi_{\text{out}} + \dot{W} + \dot{S} \quad (3.32)$$

where:

- E_{tot} is the energy associated with the control volume;
- ϕ are the inlet or outlet energy flows through the boundaries of the control volume;
- \dot{W} is the mechanical power;
- \dot{S} is the internal energy source or sink.

For heat transfer processes, the values of ϕ are given by the previously specified equations of the three modes of conduction (Eqs. (3.1), (3.3), (3.20)), depending on the applied boundary conditions. Moreover, the mechanical power is usually null in this kind of analysis.

The example of heat conduction in a solid system is taken. Terms associated with kinetic energy, potential energy and mechanical power are for obvious reasons neglected. The assumption of absence of heat sources or sinks is made as well to simplify the procedure explained hereafter. The solution of a problem with a heat source or sink term is totally alike.

The energy associated with a unit volume of the system is the internal energy, which depends on its temperature:

$$e_{\text{tot}} = \rho c_p T \quad (3.33)$$

Considering Eqs. (3.1), (3.32) and (3.33), the transient heat transfer equation is obtained:

$$\frac{\partial (\rho c_p T)}{\partial t} = -\nabla q = -\nabla (k \nabla T) \quad (3.34)$$

It can be useful to write the heat transfer equation in its integral form:

$$\frac{\partial}{\partial t} \int_V \rho c_p T dV = \int_{\partial V} k \nabla T \cdot dA \quad (3.35)$$

This is a problem in partial differential equations that require appropriate:

1. Initial condition: the distribution of temperature in the entire domain of interest known at the initial time;
2. Boundary conditions: specified conditions set on the external surfaces of the domain of interest, known at every time.

If density and specific heat are constant in the considered volume, the heat capacity can be defined as:

$$C_{\text{th}} = \rho c_p V \quad (3.36)$$

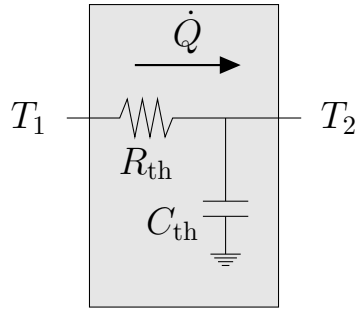


Figure 3.6: Thermal resistance and thermal capacity of a material. Heat flows from a higher temperature T_1 to a lower one T_2 through the resistance and can be stored in the thermal capacity or given back, depending on the conditions.

This leads to the possibility to apply the electrical analogy described in 3.1.4 also to the transient case. As before, heat is transferred through a certain system, that oppose a resistance (i.e. thermal resistance) to the flow. In transient applications, the heat capacity C_{th} of the system is considered: energy can be stored in the capacity or given back, depending on the conditions. Hence, the thermal capacity in a heat transfer problem plays the same role as an electrical capacity in an electric grid. The concept is represented in Figure 3.6.

For the sake of simplicity, from now on thermal resistance and thermal capacity will be called R and C respectively.

The analytical solution of the transient heat transfer equation requires the application of the method of separation of variables [36, p. 37], that is not recalled here, as a solution in closed form is possible only in very simple geometries and cases.

3.2 Computational Heat Transfer

As mentioned in the previous Section, the physical processes of heat transfer are usually described by sets of differential equations and non-linear expressions. This makes it impossible to obtain an exact analytical solution. Only a small fraction of heat transfer problems with simple geometries and limiting assumptions can be solved in closed form. The development of numerical methods, though, allowed to arrive at an approximate solution that is in most of the cases sufficient for the practical purpose for which the problem has been formulated. Indeed, a numerical solution of a differential equation consists in a finite number of values of the dependent variable at a finite number of locations in the calculation do-

main. The distribution of the dependent variable can therefore be constructed. The differential equations, with boundary and initial conditions, representing the mathematical model of the physical process must be discretized and converted to a set of algebraic equations. These can be, in their turn, numerically solved by means of a well-known method for solving linear or non-linear systems.

The techniques for the numerical analysis applied to heat transfer and thermo-fluid dynamics are thoroughly presented in Patankar's *Numerical Heat Transfer and Fluid Flow* [37]. Here only the basics and the concept employed in the present work are briefly summarized. Every further in-depth examination is sent to the specific literature.

The three most commonly used discretization schemes for differential equations are:

- Finite Difference Method (FDM): the derivatives in the governing equations are substituted with expressions based on finite differences of the independent variable and of space and time increments;
- Finite Volume Method: (FVM) the governing equations are integrated over control volumes in which the overall domain is subdivided. The conservation principles are satisfied in every finite control volume.
- Finite Element Method (FEM): the domain is divided into a finite number of elements, in which the variation of each variable follows a certain local approximating function.

As result, algebraic equations in the nodal values of the unknown variable are obtained.

According to the Finite Volume Method, the calculation domain is divided into a number of non-overlapping control volumes (Figure 3.7). In this way, each grid point is surrounded by one of these control volumes. The variables defined in the nodes are representative of the mean value in the volume. The differential equation is integrated over each control volume as in Eq. (3.35). The discretization equation obtained in this manner expresses the conservation principle for the variable of interest for the finite control volume, just as the differential equation expresses it for an infinitesimal control volume.

In this thesis, the Finite Volume Method is chosen, in order to assure that energy conservation during computation is verified.

The steady-state heat conduction equation in two dimensions is considered as

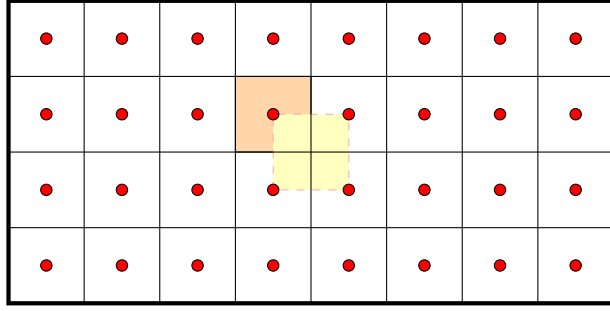


Figure 3.7: Grid or mesh centered in the volume. The computational domain is divided into control volumes. Each grid point (red dots) is surrounded by one of the control volumes.

FVM: red square

FEM: yellow square

example. Eq. (3.35) becomes:

$$\int_{\partial V} k \nabla T \cdot dA = 0 \quad (3.37)$$

The computational domain is divided into a conveniently high number of control volumes in which Eq. (3.37) is solved. An intuitive geographical notation is used: given a certain node P , in the middle of the relative control volume, the surrounding nodes are named as the cardinal points (i.e. E for east, W for west, N for North, S for South). The concept is clarified in Figure 3.8.

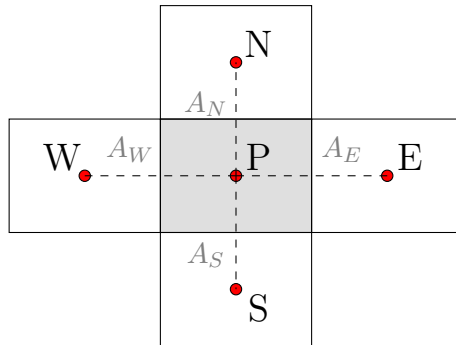


Figure 3.8: Control volume P and its surrounding ones for the two-dimensional situation. An intuitive cardinal points notation is used.

The surface integrals become the sum of the integrals on each face A_i of the control volumes:

$$\int_{A_W} k \frac{\partial T}{\partial x} dA + \int_{A_E} k \frac{\partial T}{\partial x} dA + \int_{A_N} k \frac{\partial T}{\partial y} dA + \int_{A_S} k \frac{\partial T}{\partial y} dA = 0 \quad (3.38)$$

Each derivative is then discretized with the respective finite difference, to obtain:

$$\begin{aligned} & \frac{k_W A_W (T_W - T_P)}{\Delta x_W} - \frac{k_E A_E (T_P - T_E)}{\Delta x_E} + \dots \\ & \dots + \frac{k_N A_N (T_N - T_P)}{\Delta y_N} - \frac{k_S A_S (T_P - T_S)}{\Delta y_S} = 0 \end{aligned} \quad (3.39)$$

where Δx and Δy are the directional space increments, which can change depending on the chosen grid. The thermal conductivity can change as well depending on temperature. Opportune hypothesis must be made for each situation in order to compute the value of these quantity through all the computational domain.

It is useful to cast Eq. (3.39) into the following form:

$$a_P T_P = a_W T_W + a_E T_E + a_N T_N + a_S T_S \quad (3.40)$$

where the coefficients are:

$$a_W = \frac{k_W A_W}{\Delta x_W} \quad (3.41)a$$

$$a_E = \frac{k_E A_E}{\Delta x_E} \quad (3.41)b$$

$$a_N = \frac{k_N A_N}{\Delta y_N} \quad (3.41)c$$

$$a_S = \frac{k_S A_S}{\Delta y_S} \quad (3.41)d$$

$$a_P = a_W + a_E + a_N + a_S \quad (3.41)e$$

In this way, the temperature of the grid point T_P is expressed as function of the temperatures of the surrounding nodes. Similar equations are written for all the control volumes of the entire domain. In the boundary nodes, the given boundary conditions of the problem must be applied.

The example of a convective boundary condition in the west side of the domain is here resumed. The generic volume in the west side of the domain is typically a half control volume and its grid point (i.e. T_B , for convenience) is located on the boundary surface. It is facing an external fluid with a given temperature T_{fluid} and a certain convective heat transfer coefficient h . An enlarged view of this control volume is given in Figure 3.9.

The conservation of energy is then integrated in this half volume, taking into consideration that the heat flow through the boundary face is given by:

$$\dot{Q}_B = h A_B (T_B - T_{\text{fluid}}) \quad (3.42)$$

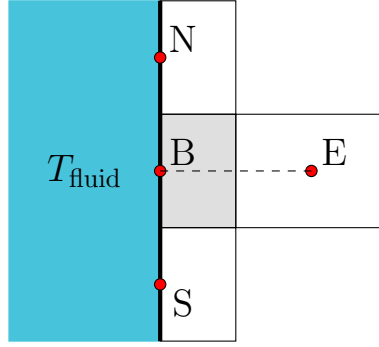


Figure 3.9: Boundary control volume B with a convective boundary condition.

Eq. (3.39) therefore becomes:

$$\begin{aligned} & hA_B(T_B - T_{\text{fluid}}) - \frac{k_E A_E (T_B - T_E)}{\Delta x_E} + \dots \\ & \dots + \frac{k_N A_N (T_N - T_B)}{\Delta y_N} - \frac{k_S A_S (T_B - T_S)}{\Delta y_S} = 0 \end{aligned} \quad (3.43)$$

Thusly, an equation similar to Eq. (3.40) can be written for each boundary grid point.

Eventually, a system of algebraic equations, where the unknown variables are the temperatures of the central points of each control volume, is obtained and solved with a numerical method.

The same procedure can be followed for every other heat transfer problem with both simplifications or more complex features: for example, the term of heat source can be added, the problem can be reduced to one dimension or, furthermore, different boundary conditions as well as a cylindrical coordinate system can be implemented.

In transient problems, Eq. (3.35) is considered again. The spatial discretization exactly follows the above-described procedure. A time-discretization must be operated as well: the time scale is divided in intervals and the time derivative is discretized with the finite difference approach. The assumption is made that the system's parameters are constant in each control volume for each time interval, so the following discretized equation can be written for each time-step:

$$\rho c_p V \frac{T^{n+1} - T^n}{\Delta t} = \sum_i (q_i A_i) \quad (3.44)$$

where the generic term of heat flux through the surfaces control volume has been written as q_i for simplicity. This equation, written for every time-step, allows to

obtain the distribution of temperature both in the spatial and time domain:

$$T^{n+1} = T^n + \sum_k \left(q_i \frac{A_i}{C} \Delta t \right) \quad (3.45)$$

However, the way of evaluating inlet and outlet heat flows must be chosen. Various possibilities are available, two of which are here summed up:

- Explicit method: heat flows for calculating the temperature of the control volume at the time step $n + 1$ are evaluated at the previous time step n . It essentially assumes that the old value of the temperature T^i prevails throughout the entire time step. This means that T^{i+1} is explicitly obtainable in terms of the surrounding temperatures at the previous time step, that has been already calculated. This convenience is however offset by the need to comply with the stability criterion which, in case of one-dimensional model, is:

$$Fo = \frac{k}{\rho c_p} \frac{\Delta t}{(\Delta x)^2} < 0.5 \quad (3.46)$$

where Fo is called Fourier's number. If this condition is violated, physically unrealistic results could emerge [37, p. 57].

- Implicit method: heat flows for calculating the temperature of the control volume at the time step $n+1$ are evaluated at the time step $n+1$. In this case, the new temperatures at the time step $n+1$ are strictly interlinked and must be solved together as in a system. This scheme is, therefore, computationally heavier than the previous one. Nonetheless, it is unconditionally stable and no limitations on the choice of the time-step Δt are necessary.

Due to its characteristics of stability and flexibility, the latter scheme is chosen for the transient simulations in this work. The possibility to choose an arbitrary time-step or enhance the spatial accuracy, if required, justifies the higher computational time.

In such a way, Eq. (3.45) becomes:

$$T_i^{n+1} = T_i^n + k_{i-1} \frac{T_i^{n+1} - T_{i-1}^{n+1}}{\Delta x_{i-1}} \frac{A_{i-1}}{C_i} \Delta t + k_{i+1} \frac{T_{i+1}^{n+1} - T_i^{n+1}}{\Delta x_{i+1}} \frac{A_{i+1}}{C_i} \Delta t \quad (3.47)$$

For instance, a one-dimensional configuration has been considered. The equation is written for a generic control volume i between time steps $n + 1$. It can be cast in the intuitive shape as Eq. (3.40), applied to the whole domain and then solved for each time step.

One last topic needs to be recalled here. In the next Sections of this thesis, heat conduction in solids is usually coupled with gas flows exchanging energy with them. The velocity field is not a focus of the analysis here presented. Nonetheless, when a convective term is part of a transient problem, the *upwind* scheme is usually adopted [37, p. 83]. This scheme is developed for strong convective flows, where the diffusion effect can be neglected. A non-dimensional parameter, called Peclet number (Eq. (3.48)), determines the comparative strengths of convection and diffusion in a fluid of speed u and density ρ and a system of length L .

$$Pe = \frac{\rho u L}{k} \quad (3.48)$$

where k is the conductivity of the fluid and represents the diffusive contribution. For $Pe > 1$, convection dominates the flow and the variables of the flow in the control volume are assumed to be those of the incoming fluid, according to the upwind approach.

In the components of the hybrid power plant at DLR, the fluid flows are typically gaseous and have therefore a low value of thermal conductivity. Moreover, the speed of the flows is usually of the order of magnitude of 10 m/s , hence giving a high Peclet number.

4 Model Implementation

This Section contains the details regarding the building of a model that is able to predict heat losses from the system's components in various operating conditions, with a feasible accuracy and a low computational time. The model is implemented in the MATLAB environment [47].

The general approach adopted first for the stationary and then for the transient model implementation is described. It is followed by a summary of the simplifications that it is possible to apply in order to speed up the computation. Eventually, more peculiar considerations concerning the modeling of each specific component are made.

Before going into details, a preliminary description of the global model approach is necessary to give an idea of the programming style that the new heat losses models should match.

The hybrid power plant is modeled at system level, where each component is an open sub-system schematized as a black box (Figure 4.1).

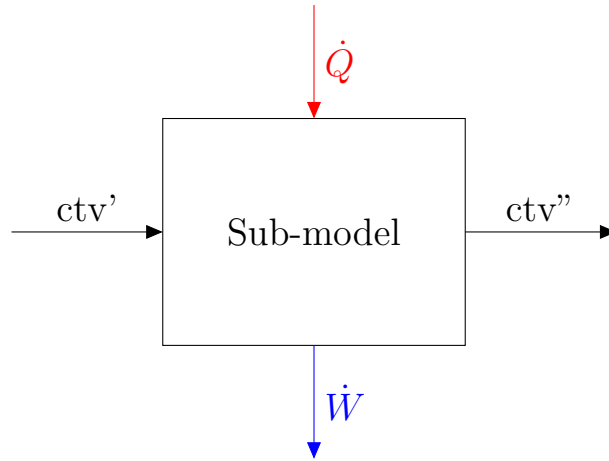


Figure 4.1: Black-box concept. Each sub-model has a combined transfer vector as input (ctv') and a combined transfer vector as output (ctv''). Additional inputs or outputs are the energy flows (\dot{Q} , \dot{W}).

The input and output of each block are combined transfer vectors (ctv) that identify the gas flow and consist of three fundamental parameters:

1. Temperature;
2. Pressure;
3. Composition of the stream.

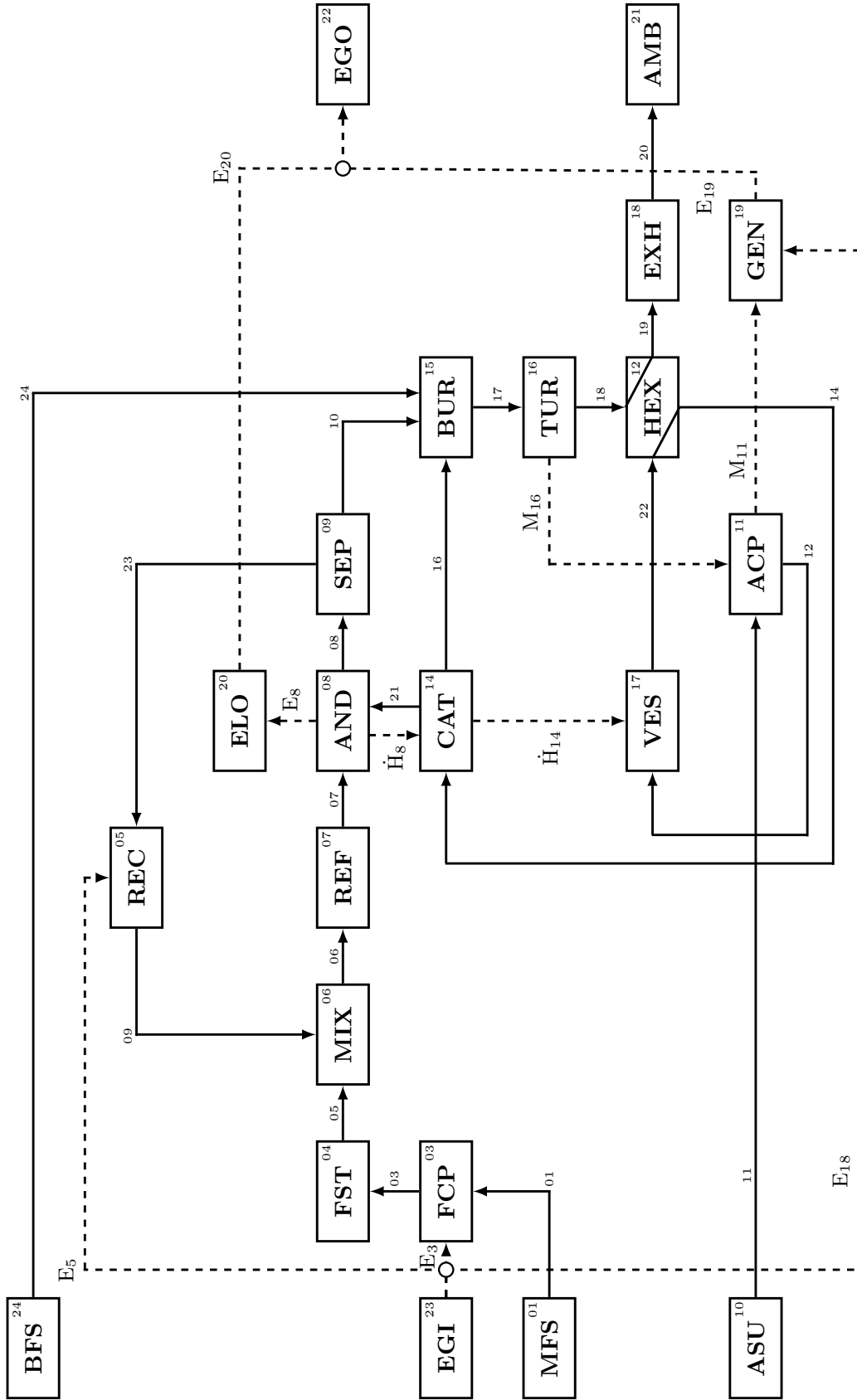


Figure 4.2: Hybrid power plant global model concept. For the meaning of the abbreviations, see Nomenclature.

Additional outputs of the blocks are typically energy flows (i.e. heat or power). The blocks of the components and any other relevant sub-model such as the calculation of properties or the definition of the boundary conditions are stored in a Library and then called for running the global system simulation.

The block diagram of the entire system is shown in Figure 4.2. The modular approach and the various components of the hybrid power plant can be recognized. The complexity of the global model, characterized by a high number of blocks and loop-type interactions between them, is clear. New blocks that compute heat losses for the system must then be included in the Library, in order to perform the global simulation in both adiabatic and non adiabatic way.

4.1 Computation of Thermo-physical Properties

The temperature range of interest in the system is $300 - 1200\text{ K}$. The thermo-physical properties of gas flows and solid materials are subject to significant variations in that range. For this reason, a deepened analysis is performed in order to accurately estimate the material properties for calculation.

4.1.1 Gas Properties

In the present work, the assumption of ideal gas is made. The gaseous species involved are summarized in Table 4.1.

Table 4.1: Gas species involved in the hybrid power plant simulation

Gas species						
1	2	3	4	5	6	7
CH_4	H_2	CO	CO_2	H_2O	O_2	N_2

The composition of gaseous flows changes in some components throughout the hybrid power plant. Hence, sub-models are required to compute properties for a gas mixture. The relevant properties are calculated as follow:

- Density is calculated according to the ideal gas law:

$$\rho = \frac{p \cdot M}{R \cdot T} \quad (4.1)$$

where p , M and T are respectively pressure, molar mass and temperature of the gas and R is the universal gas constant;

- Specific heat for each species is a function of temperature through the 7-coefficient NASA polynomials [11]. The specific heat of a gas mixture is the average mean of the specific heats of each component weighted with the relative molar fractions:

$$c_p = \sum_i X_i c_{p_i} \quad (4.2)$$

When the specific heat of a gas mixture between two temperatures T_{in} and T_{out} is needed, an average value is calculated according to Eq. (4.3).

$$\bar{c}_p = \frac{\int_{T_{\text{in}}}^{T_{\text{out}}} c_p dT}{T_{\text{out}} - T_{\text{in}}} \quad (4.3)$$

- Dynamic viscosity of a pure species is a function of temperature through a polynomial fitting based on data from NIST database [30]. The fitting is operated for the relevant temperature range. The dynamic viscosity of a gas mixture is calculated according to Wassiljeva's rule [1]:

$$\mu = \sum_i \frac{X_i \mu_i}{\sum_j X_j \Phi_{ij}} \quad (4.4)$$

where Φ_{ij} is a correction factor as indicated by Mason and Saxena in [32]:

$$\Phi_{ij} = \frac{1}{2\sqrt{2}} \left(1 + \frac{M_i}{M_j}\right)^{-1/2} \left[1 + \left(\frac{\mu_i}{\mu_j}\right)^{1/2} \left(\frac{M_i}{M_j}\right)^{1/4}\right]^2 \quad (4.5)$$

- Similarly, thermal conductivity of a single species is function of temperature through a polynomial fitting based on data from NIST database [30]. The calculation of the thermal conductivity of a gas mixture is analogous to the one for dynamic viscosity through equations (4.4) and (4.5).

The computation of dynamic viscosity and thermal conductivity is complex and computationally inefficient. The attempt to speed up this part of the code through a simplification has been successful. Data obtained with equations (4.4) and (4.5) are compared with the values obtained as average mean of each component weighted with the relative mass fractions as in Eq. (4.6):

$$\mu = \sum_i Y_i \mu_i \quad (4.6)$$

Table 4.2: Comparison of the computational time necessary to calculate the gas mixture properties with a the Wassiljeva’s mixture formula and with the simplified weighted mean.

	Mixture Formula	Weighted Mean	Percentual Gain
Dynamic Viscosity	0.103 <i>s</i>	0.045 <i>s</i>	56%
Thermal Conductivity	0.095 <i>s</i>	0.024 <i>s</i>	75%

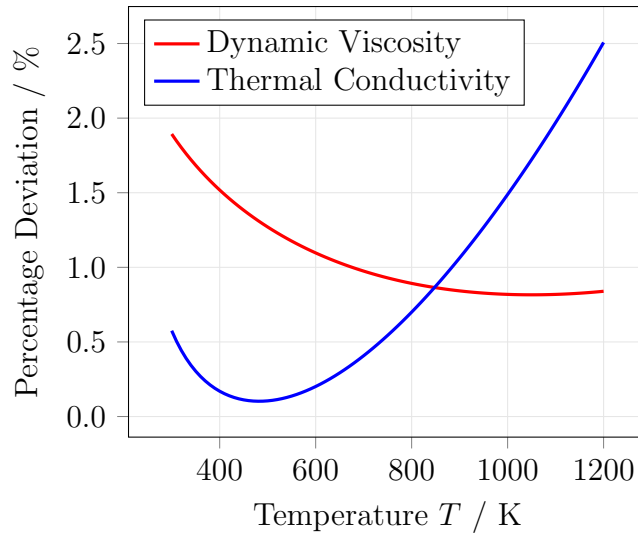


Figure 4.3: Percentage deviation of dynamic viscosity and thermal conductivity of a generic gas mixture calculated with the simplified weighted mean from the values calculated with the Wassiljeva’s mixture formula.

The results of this comparison are shown in Figure 4.3 and Table 4.2.

The deviation between the two chosen methods for the calculation of viscosity of gas mixtures on varying of temperature is not relevant for the required accuracy. On the other hand, the computational time spent with the wighted average method (Eq. (4.6)) is significantly lower. Therefore the latter can be chosen a sub-model for the global simulations.

4.1.2 Solid Material Properties

The solid materials associated with the operation of the hybrid power plant are those composing the pipings, the components and the relative insulation. Due to the broad changes in temperature occurring along the entire system, it is necessary to account for the variation with temperature of the properties of the solid

materials as well. For this purpose, a materials database is created.

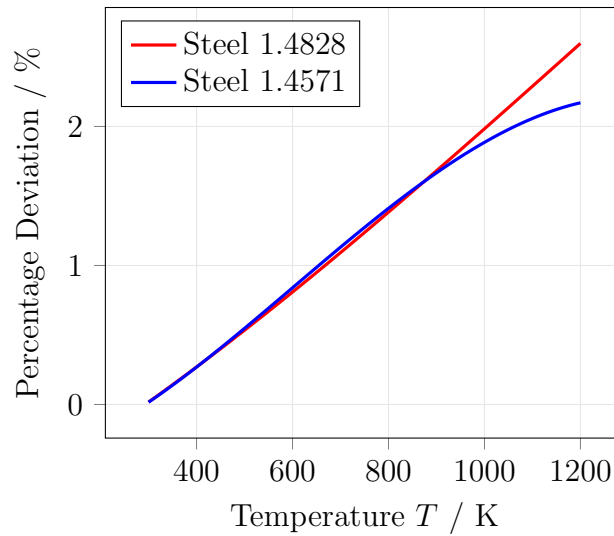


Figure 4.4: Percentage deviation of the density of the two types of stainless steel used for the hybrid power plant at DLR from the values at ambient temperature. The density does not relevantly change with temperature.

The properties of interest for the solids are:

- Thermal conductivity: polynomial fittings of values provided by the manufacturers for each material are made;
- Specific heat: the same procedure as for thermal conductivity is followed;
- Density: it does not relevantly change with temperature (Figure 4.4).

The database is fulfilled with the real system parameters and can be easily updated in case of any changes.

4.2 Stationary Model

The complexity of the system is clear from the representation of the hybrid power plant in Figure 4.5. The components that can be source of high thermal losses are many. In particular, there is a high number of pipings leading gas whose temperature is high compared to the ambient one.

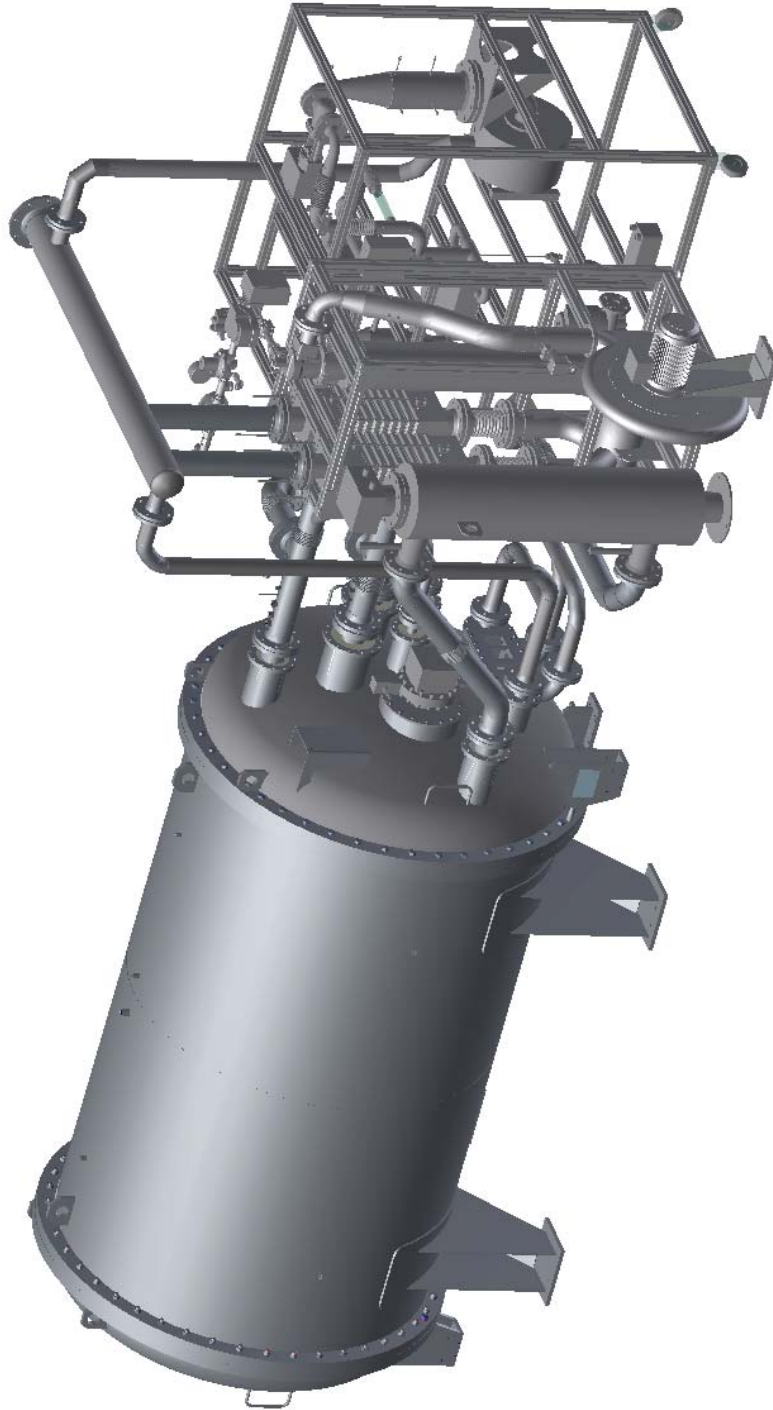


Figure 4.5: Hybrid power plant 3D drawing.

The model must satisfy the following requirements:

- Integration in the global system model, as described at the beginning of Section 4;
- Switch for adiabatic mode, in order to allow simulations in both adiabatic and non-adiabatic modes and perform a comparison;
- Use of real system parameters (i.e. geometry and materials);
- High computational speed: the high number of components, the loop-type interactions between them and the amount of relevant operating points disclose the need for low computing time;
- Feasible accuracy.

In order to choose the modeling concept that best matches the requirements, a comparison of different strategies must be made. Here, the details of the multi-dimensional models of a tube with a fluid exchanging energy with the ambient in steady state conditions are explained and compared.

4.2.1 Two-dimensional approach

The theory of computational heat transfer (Section 3.2) is adapted for a cylindrical coordinate system and applied.

The two-dimensional concept applied to the tube is represented in Figure 4.6. The following assumptions are made:

1. The tube is axisymmetric;
2. The variables change in axial and radial directions;
3. The grid is built discretizing the tube in axial slices of length Δz and in cylindrical shells of thickness Δr ;
4. According to the FVM, the variables are uniform in the generic finite volume where the energy balance is applied;
5. The thermal conductivity of the materials is highly dependent on temperature so it is not considered constant throughout the system;
6. The variation of the gas temperature is accounted along the tube's axis;
7. Boundary conditions:

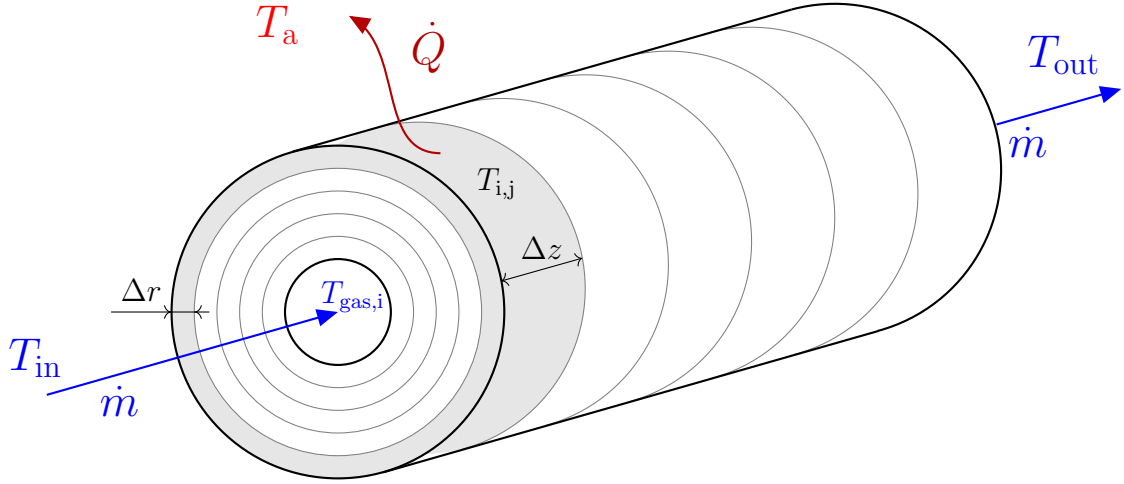


Figure 4.6: Schematic representation of the two-dimensional model. The generic finite volume with temperature $T_{i,j}$ is highlighted.

- (a) In the extreme cross-sections of the tube, the heat flux is assigned equal to zero;
- (b) In the inner surface of the tube, a convective condition is assigned. Eq. (3.12) is used for the implementation of the internal heat transfer coefficient, as it allows to account for the tube's roughness;
- (c) In the outer surface of the tube, a convective condition is assigned. Eq. (3.14) is used for the implementation of the external heat transfer coefficient.

Under these considerations, an algebraic system of equations analogue to Eq. (3.40) is built. The solution of the system depends on the temperature of the gas flowing inside the tube. The multi-dimensional solver developed at DLR is able to solve the system and obtain heat losses and outlet conditions of the gas.

4.2.2 One-dimensional approach

As mentioned before in the work, one of the most important requirements for the model is its computational time, in order to maintain a fast overall model. Simplifications must be done and verified.

According to the one-dimensional approach, represented in Figure 4.7, the following further assumptions are made:

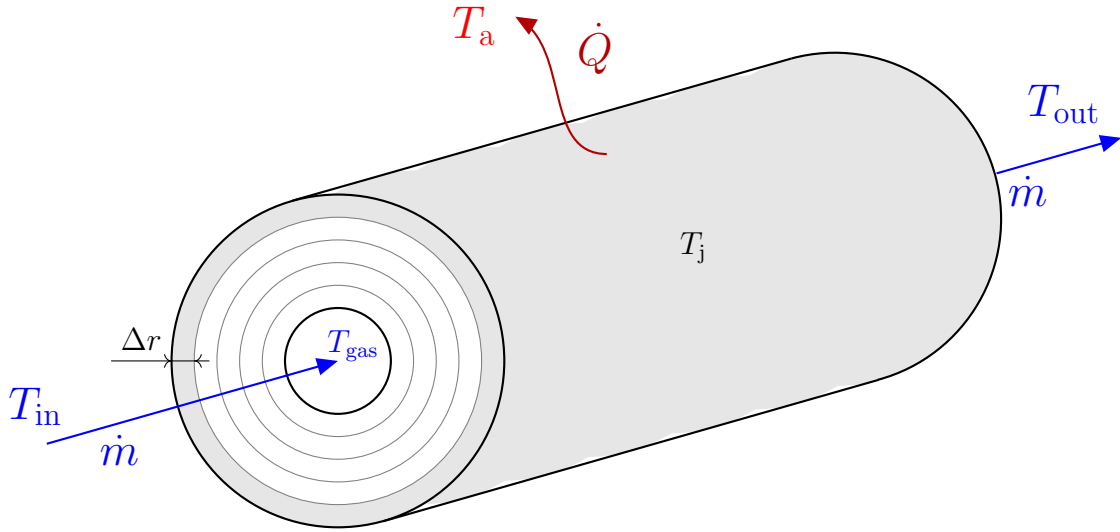


Figure 4.7: Schematic representation of the one-dimensional model. The generic finite volume with temperature T_j is highlighted.

1. The temperature gradients are expected to be higher in the radial direction than in the axial one. As a matter of fact, the temperature of the gas stream inside the tube can vary in the range of interest in a significant way, in comparison with the environment. Hence, the variables only change in the radial direction;
2. The tube is discretized only in cylindrical shells of thickness Δr ;
3. Heat flow in the axial direction is zero as every cylindrical shell is considered isothermal;
4. Thermal conductivity varies with temperature, therefore each shell has a different conductive thermal resistance calculated as in Eq. (3.24);
5. A mean gas temperature along the tube is considered;
6. Boundary conditions:
 - (a) Convection with the internal gas is calculated through Eq. (3.25), where the heat transfer coefficient is given by Eq. (3.12);
 - (b) Similarly, the heat transfer coefficient for external convection is given by Eq. (3.14).

Heat flow to the environment is calculated by means of Eqs. (3.31) and (3.30). The total thermal resistance accounts for all the material layers which, in their turn, account for the variation of temperature.

In a stationary problem, heat exchanged to the outside must be equal to the heat lost or gained by the fluid itself. An iterative procedure to find this quantity is performed by the solver, as it is explained better in the next Section.

4.2.3 Zero-dimensional approach

According to the zero dimensional approach, the parameters are uniform in the system considered.

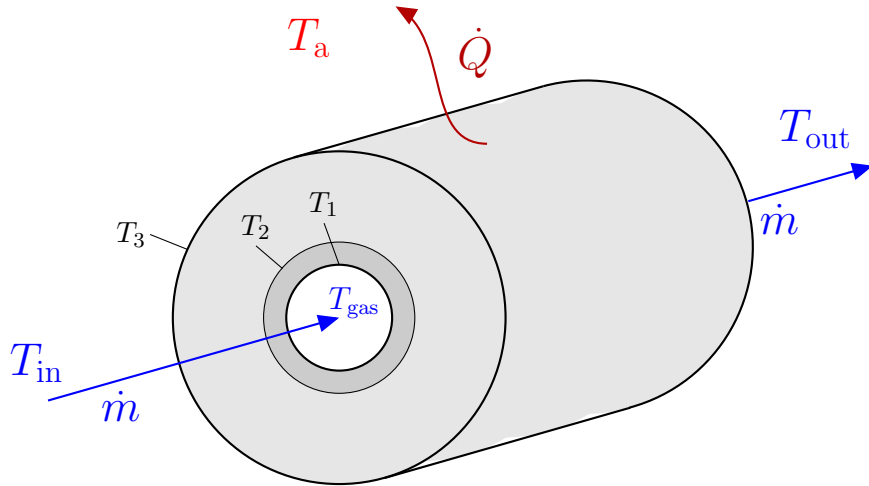


Figure 4.8: Schematic representation of the zero-dimensional model with two materials.

The components of the real system, though, are made of different materials: the tubes, in particular, have multiple radial layers of insulation. It is necessary to evaluate the material properties at a temperature which is as accurate a possible, due to the consistent variation that especially the conductivity is subjected to.

For this purpose, the evaluation of the temperatures at the interfaces can be beneficial to obtain a better accuracy.

As the radial distribution of temperature is unknown, it is necessary to compute an iterative procedure. The algorithm created for computing heat losses is represented in Figure 4.9.

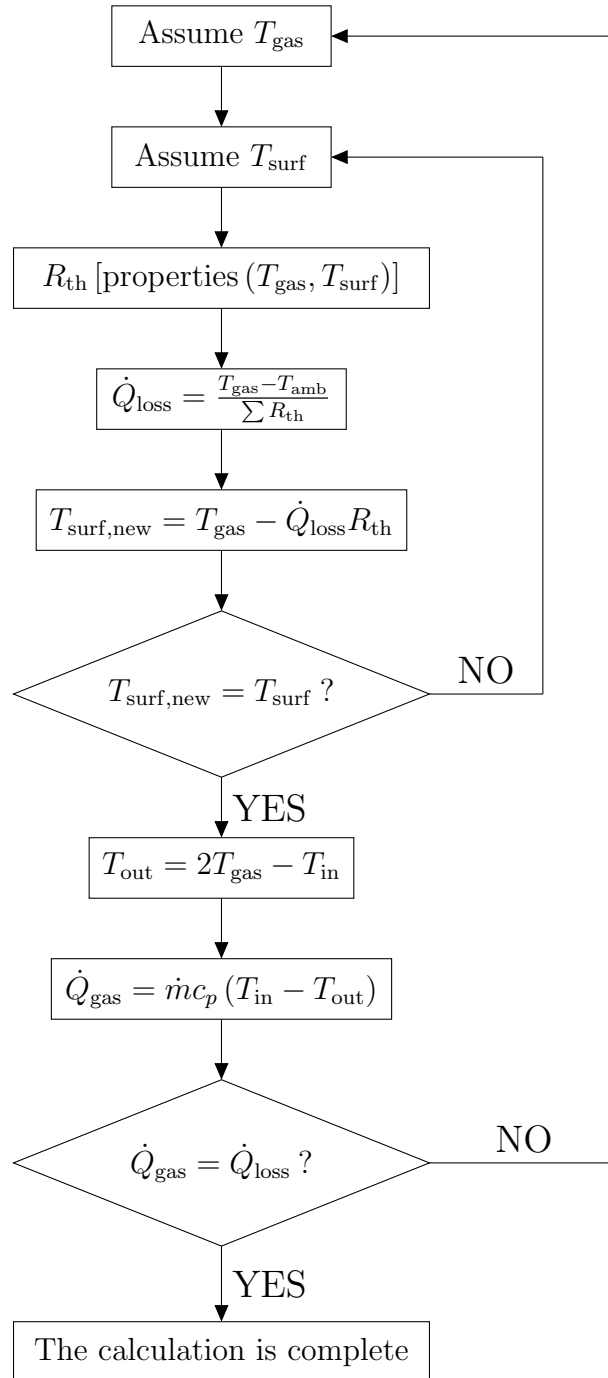


Figure 4.9: Algorithm implemented in MATLAB for the computation of heat losses of an insulated tube.

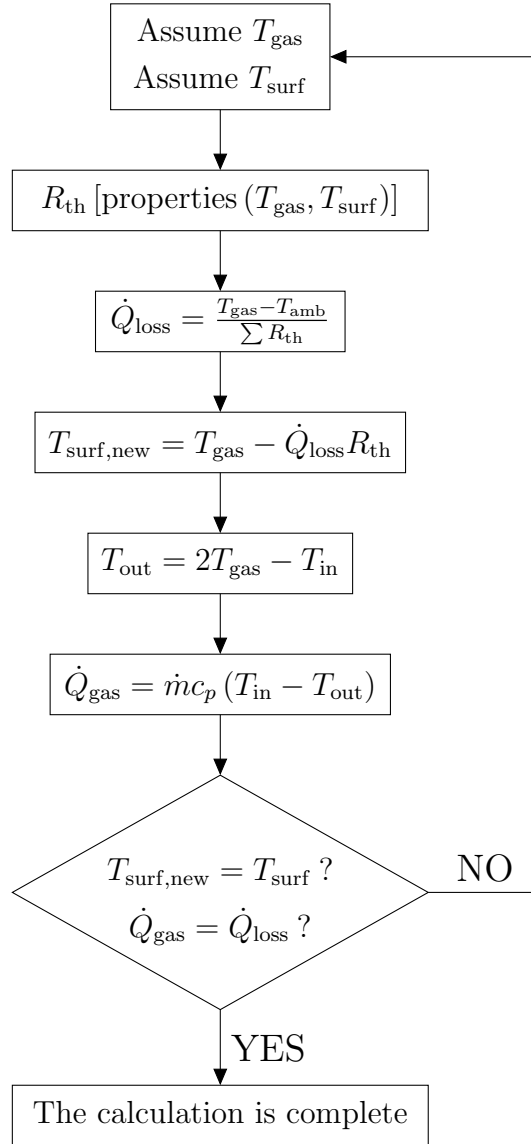


Figure 4.10: Algorithm implemented in MATLAB for the computation of heat losses of an insulated tube with the use of the DLR in-built multi-dimensional solver. A loop is eliminated with a consistent gain in computational efficiency.

T_{gas} is the gas mean temperature between inlet and outlet of the tube, while T_{surf} is an array containing the temperatures of the surfaces of the layers composing the tube (i.e. piping and insulation layers). T_{gas} and T_{surf} are assumed and the material properties are estimated on the base of the assumed values. The thermal resistances are calculated according to heat transfer theory (Section 3.1.4). A first guess of the heat flowing from the gas stream towards the environment is therefore evaluated by Eq. (4.7):

$$\dot{Q}_{\text{loss}} = \frac{T_{\text{gas}} - T_{\text{a}}}{\sum_i R_{\text{th},i}} \quad (4.7)$$

Knowing the heat flow, it is now possible to calculate the new real surface temperatures reapplying Eq. (4.7) with the proper resistances. If the new values differ from the first guesses of more than the desired tolerance, a new T_{surf} array is guessed until the equivalence is reached. Then, the outlet temperature is calculated by the assumption of the mean temperature T_{gas} . Hence, the inlet and outlet enthalpy flows can be evaluated and the heat lost by the gas inside the tube is found (Eq. (4.8)).

$$\dot{Q}_{\text{gas}} = \dot{m}c_p(T_{\text{in}} - T_{\text{out}}) \quad (4.8)$$

According to the principle of conservation of energy, the fluid enthalpy difference between inlet and outlet \dot{Q}_{gas} must be equal to the energy exchanged with the environment through the tube \dot{Q}_{loss} . In this way, the enthalpy balance on the fluid flow is respected:

$$\dot{H}_{\text{in}} - \dot{H}_{\text{out}} = \dot{Q}_{\text{loss}} \quad (4.9)$$

If this does not happen, a new T_{gas} is guessed and the iteration loops are repeated until convergence to the desired tolerance is reached. Heat loss and gas outlet conditions are then obtained.

The use of the MATLAB function *fzero* in the solving process allows to solve only one-variable functions at a time. Thus, a double-loop algorithm is needed. An in-house multidimensional solver, developed at DLR in the MATLAB environment, allows instead to find quickly the solution to multi-variable functions. A simplified algorithm with one iteration loop can be implemented (Figure 4.10). T_{gas} and T_{surf} are simultaneously assumed by the solver and the residuals in Eqs. (4.10) and (4.11) are simultaneously solved. A loop is then eliminated and the calculation is completed with a consistent gain in computational efficiency.

$$dT = T_{\text{surf,new}} - T_{\text{surf}} \quad (4.10)$$

$$d\dot{H} = \dot{H}_{\text{in}} - \dot{H}_{\text{out}} - \dot{Q}_{\text{loss}} \quad (4.11)$$

4. Model Implementation

Now a problem arises. It is acknowledged that SOFCs are high temperature systems and require a considerable amount of insulation. Consequently, temperature variation in the radial direction, from gas flow to the environment, can be significant. In a zero-dimensional approach, the distribution of temperature in the insulation can not be accounted for and the evaluation of the conductivity is not accurate. Different assumptions can be made as follows for choosing the temperatures for the calculation of the properties:

1. Temperature of the hotter surface for each layer. Generally, thermal conductivity increases with temperature, so this approach leads to the highest losses;
2. Temperature of the coldest surface for each layer, which leads to the lowest losses;
3. Arithmetic mean between the temperatures of the two sides of each layer. This is an intermediate situation between the first two;
4. Logarithmic mean between the temperatures of the two sides of each layer. This approach is evaluated since, in a cylindrical coordinate system with constant k , the temperature profile in the radial direction is logarithmic;
5. The neutral face of each layer is considered in the solving process instead of the external surfaces (Figure 4.11). Each thermal resistance is calculated as a series of two resistances.

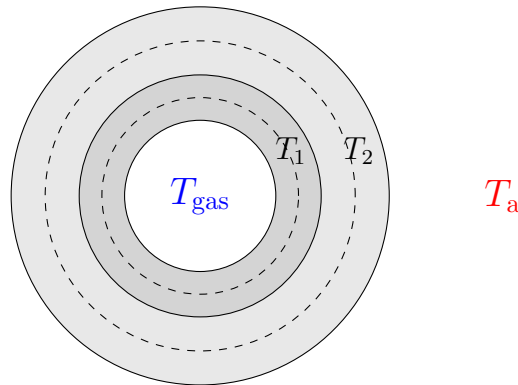


Figure 4.11: Representation of the neutral surfaces in a tube with two layers.

These different approaches are analyzed and compared in Section 5.2. Methods 1 and 2 allow to understand which are the boundaries of the solution given by the model, while the other methods constitute an engineering guess of the solution.

Of all the approaches described, the one that gives the best ratio accuracy - computational time must be chosen and applied to the global model.

4.3 Transient Model

One of the goals of the present work is to allow the simulation of the transient processes of the hybrid power plant operation. To do so, the stationary models previously described are adapted as transient models.

Each control volume the computational domain is divided in carries a heat capacity, whichever approach described for the steady-state analysis is chosen. This influences the heat transfer, as described in Section 3.1.5, since heat can be stored in the capacity of the materials composing the system.

The hybrid power plant is expected to have a relevant heat capacity, due to the high number of components and, especially, their insulation (Figure 4.5), that can work as a heat storage system. Knowing the temperature of this heat storage can be beneficial to investigate the behavior of the system over time.

The strategy used to build the transient models follows the rules described in Section 3.2. The following assumptions are made:

- The Finite Volume Method for the spatial discretization is here applied as well;
- The time-step Δt is an outer boundary of the problem. A shorter time-step can be given as input when a relatively fast change in operation must be evaluated. A longer time-step is given when the system gets closer to a steady-state, in order to save computational-time;
- The implicit method for the time-discretization is adopted. This scheme is unconditionally stable and there is not any limitation on the time-step;
- Real system's capacity parameters are used;
- The initial temperature of the capacity is an input to the problem (initial condition);
- The material properties are calculated at the initial temperature;
- The system exchanges heat with the fluid at a mean temperature between inlet and outlet, solved by means of an iterative procedure;
- According to the upwind scheme, diffusion in the fluid is neglected;

- Due to the use of the implicit method, a tridiagonal system is obtained. It is solved with the well-known computationally efficient Thomas algorithm.

The model is solved for the given initial condition and time-step. The outputs of the model are the outlet conditions of the fluid flow, the heat exchanged by the fluid with the materials, that depends on the parametrized properties of the system, and the temperature of the system's capacity. The knowledge of the temperature of the storage system at a given time-step is important for determining the conditions of the heat storage.

The following desired time-step is then solved with the new temperatures as initial conditions.

4.4 Computational Time

In order to speed up the model and reach the goal of a low computational time, both mathematical and conceptual simplifications can be operated on the model itself.

4.4.1 Mathematical Simplifications

Section 4.1 shows the high number of polynomials that must be computed to calculate the necessary thermo-physical properties, as their dependence on temperature is expressed in a polynomial form. Furthermore, due to the loop-type interactions between the hybrid power plant's components, each polynomial is computed a high number of times.

As mathematical simplification, the Horner's method [51] is applied to transform polynomials into computational efficient forms. Given a generic T -dependent polynomial expressed in the following form:

$$p(T) = a_0 + a_1T + a_2T^2 + \dots + a_{n-1}T^{n-1} + a_nT^n \quad (4.12)$$

which requires, depending on the algorithm, $(n^2 + n) / 2$ or at least $2n - 1$ multiplications and n additions. Rearranging Eq. (4.12) in a different form, the polynomial can be written as:

$$p(T) = a_0 + T(a_1 + T(a_2 + \dots + T(a_{n-1} + a_nT) \dots)) \quad (4.13)$$

This latter form requires only n multiplications and n additions. Hence, without losing accuracy, as Horner's method simply writes the same equations in a different and more efficient way, a significant decrease of the computational time is obtained.

This is shown in Figure 4.12, where the deviation of the computational time spent in the calculation of some of the relevant properties with and without Horner's algorithm is represented depending on the number of computed iterations.

The gain is even clearer if a rough example is made: in computing the properties for a transient tube simulation 50000 times, using Horner's algorithm allows to reduce the time from 45 to 25 s, with an increase in efficiency of 45%.

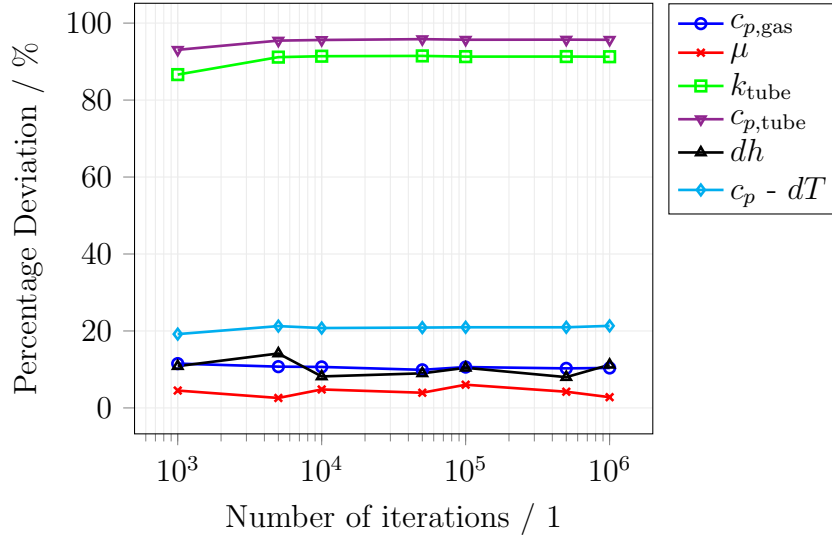
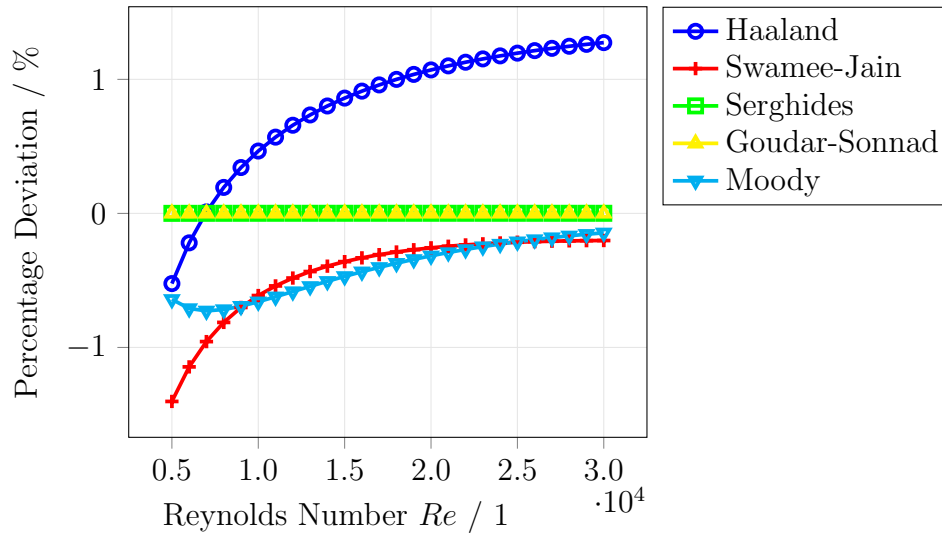


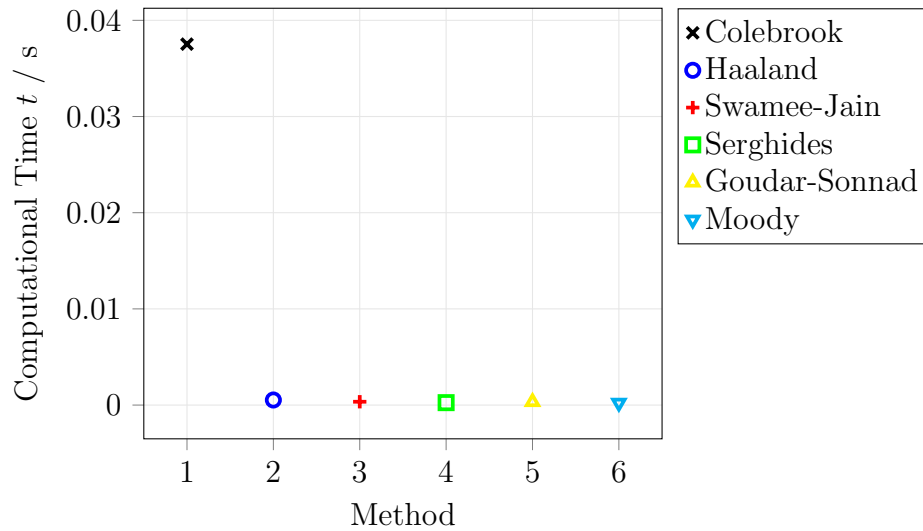
Figure 4.12: Percentage deviation of the computational time spent in the calculation of the thermo-physical properties with and without Horner's method.

4.4.2 Conceptual Simplifications

As mentioned in Section 3.1.2, the Darcy friction factor must be calculated for the internal heat transfer coefficient of the rough components of the system (i.e. pipings). The Darcy friction factor is given by the Colebrook-White correlation (Eq. (3.13)), which is non-explicit and therefore computationally inefficient. Various approximations of the Colebrook-White equations are available in literature [20]. Figure 4.13 shows the influence of each of those methods on the accuracy of the result and on the computational time. The model considered is the one of an insulated tube with a gas inlet temperature of 1125 K. It is clear that the deviation from the value given by the Colebrook-White equation obtained if different approximations are implemented is not significant (Figure 4.13a). Simultaneously, the gain in computational speed of the approximations presented is relevant compared to the use of the Colebrook-White equation (Figure 4.13b). Therefore, the Serghides formulation [20] is here implemented.



(a)



(b)

Figure 4.13: Calculation of Darcy friction factor with different methods: (a) percentage deviation from the Colebrook-White equation, (b) influence on the computational time.

Another conceptual simplification that is operated regards the emissivity of the materials of the system. Particular and necessary attention must be paid to the material properties as functions of temperature. Nonetheless, the emissivity is considered constant throughout the entire temperature range of interest. This is reasonable because radiation is not a dominating mode of heat transfer and the influence on the accuracy of the results is not relevant. The percentage deviation of the heat loss from a test tube obtained supposing different values of emissivity to simulate its dependence on temperature is shown in Figure 4.14. Considering a constant value does not clearly affect the accuracy of the result.

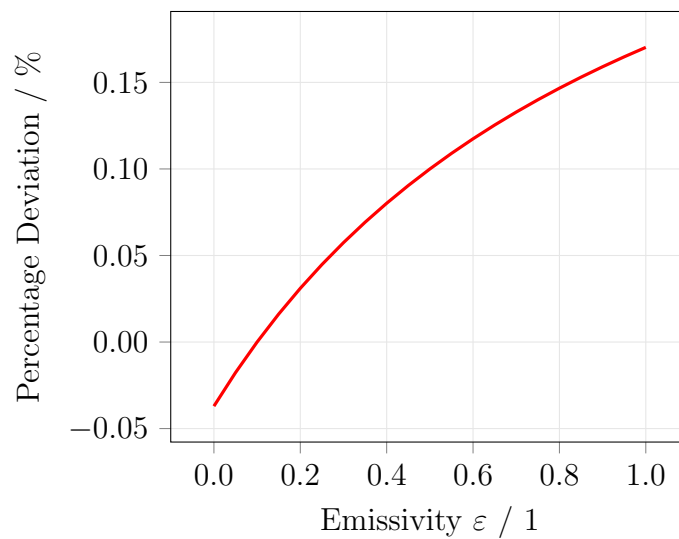


Figure 4.14: Percentage deviation of the heat loss calculated with different values of emissivity to simulate its dependence on temperature.

Lastly, a simplification on the external convection is here recalled. As cited previously in Section 3.1.2, the external convection is considered forced in every case, due to the presence of a ventilation system in the DLR facility. As a matter of fact, in order to apply the correct empirical correlation for the natural convection heat transfer coefficient, every case should carry the information regarding the orientation of the external surfaces, thus adding complexity to the calling of each sub-model.

4.5 Models of Components

The procedure that is followed for the analysis of heat losses from the pipings of the system must be applied to the other components of the hybrid power plant. The

real system parameters for each component are implemented as relative boundaries.

4.5.1 Reformer

As mentioned already in Section 2.1, an external reformer is a catalytic active surface that changes heat for chemical energy in favor of the SOFC operation. The external reformer is a necessary safety measure, as it is significantly cheaper compared to the SOFC stacks, so it can be sacrificed during start-up and transition processes, in case of break down due to recirculation problems. It is additionally beneficial to allow the operation of the hybrid power plant with fuel such as methane, natural gas or biogas.

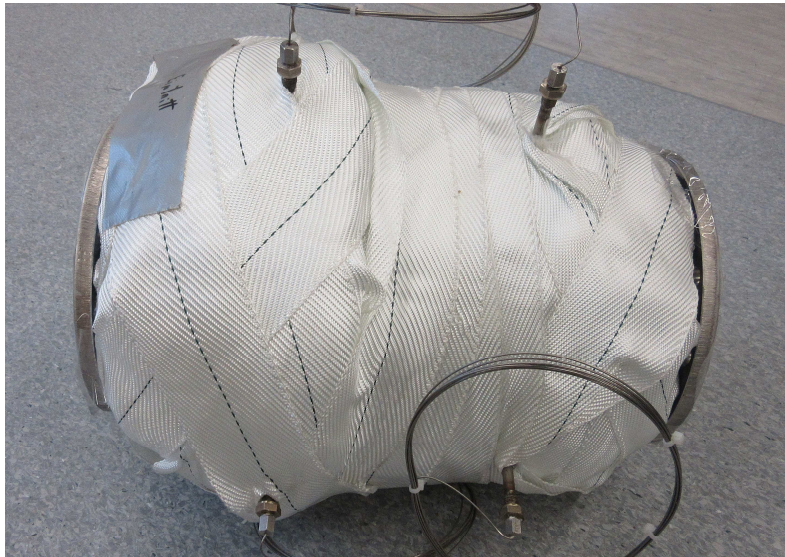


Figure 4.15: Reformer with insulation.

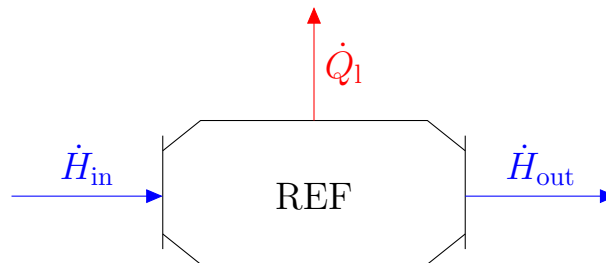


Figure 4.16: Reformer (REF) schematic representation. Heat losses from the component are included in the model.

The external reformer of the pilot power plant at DLR, represented in Figure 4.15

with its insulation, is placed inside the pressure vessel. Compressed fuel is mixed with part of the off gas recirculated from the anode and taken to the reformer to allow the reactions (2.2). Then, the hydrogen rich flow is led to the SOFC anode through a tube.

Heat losses are modeled considering the reformer as an insulated tube. The procedure is similar to the one described in Section 4.2. On the basis of the schematic representation depicted in Figure 4.16, the enthalpy balance is derived as in Eq. (4.14).

$$\dot{H}_{\text{in}} - \dot{H}_{\text{out}} - \dot{Q}_{\text{loss}} = 0 \quad (4.14)$$

The output temperature and composition computation is provided by the software package Cantera through the calculation of thermodynamic equilibrium [21]. The external boundary conditions are those of the pressure vessel.

4.5.2 Recirculation Blower

The importance of recirculating part of the anode off gas has been highlighted in Section 2.1.

The recirculation blower, shown in Figure 4.17, has the operating temperature of around 1125 K and is specifically designed and supplied for the hybrid power plant. It is situated in the pressure vessel's front lid, facing the external ambient through the heat sink.



Figure 4.17: Recirculation blower.

In adiabatic mode, the process of recirculation is modeled as an adiabatic com-

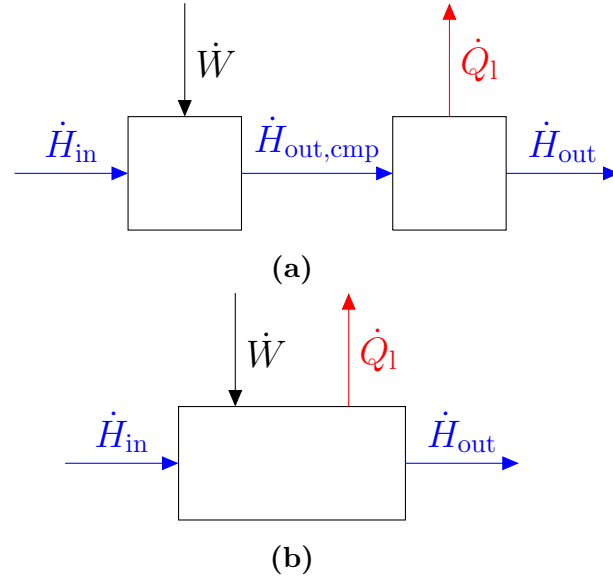


Figure 4.18: (a) Recirculation modeled as an adiabatic compression with after-cooling. (b) Recirculation modeled as a non adiabatic compression.

pression requiring the mechanical power given by Eq. (4.15).

$$\dot{W} = \dot{m}c_p T_{in} \left[\left(\frac{p_{out}}{p_{in}} \right)^{R/c_p} - 1 \right] \frac{1}{\eta_{is,cmp}} \quad (4.15)$$

On the other hand, in non-adiabatic mode, the process involves some cooling, that is the thermal loss from the gas to the environment. Two possible ways to model this situation are explained and compared:

1. The process is assumed to take place in two stages: first an adiabatic compression occurs, followed by a thermal loss to the outside (Figure 4.18a). The enthalpy balance of the compression is as follows:

$$\dot{H}_{in} - \dot{H}_{out,cmp} + \dot{W} = 0 \quad (4.16)$$

where \dot{W} is given by Eq. (4.15) and $\dot{H}_{out,cmp}$ is the theoretical outlet temperature of the compressor. The balance of the second stage of the process is:

$$\dot{H}_{out,cmp} - \dot{H}_{out} - \dot{Q}_{loss} = 0 \quad (4.17)$$

The way in which heat loss \dot{Q}_{loss} is obtained is explained later in this Section. The consequentiality of the two processes is here introduced in order to simplify the model and reduce the computational time.

2. The compression is polytropic. Compression and thermal loss occurs at the same time (Figure 4.18b). The global balance is as follows:

$$\dot{H}_{\text{in}} - \dot{H}_{\text{out}} + \dot{W} - \dot{Q}_{\text{loss}} = 0 \quad (4.18)$$

This concept is approximated to a multi-stage compressor with inter-stage cooling, where the number of stages tends to infinite. For each stage, Eq. (4.18) is solved.

The latter strategy models reality more accurately than the former one, as compression and thermal loss are not consequential but simultaneous. However, it is extremely inefficient from a computational point of view, since it requires the solution of a large number of compression stages.

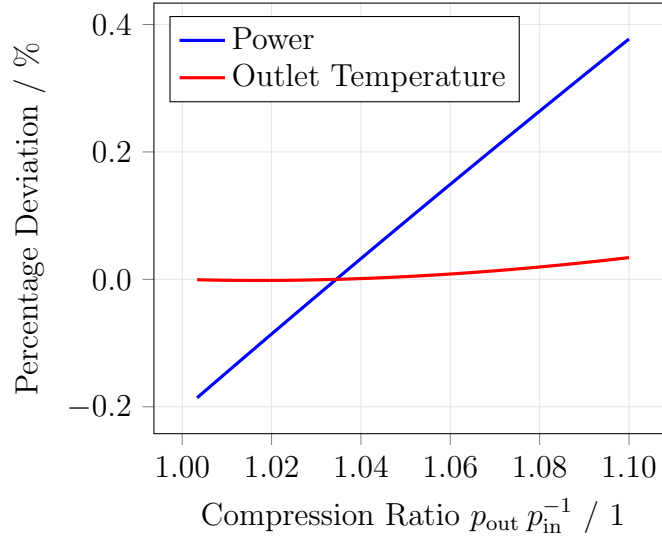


Figure 4.19: Percentage deviation of outlet temperature and mechanical power of the recirculation blower between the two modeling strategies.

Figure 4.19 shows the percentage deviation between the results obtained with the two strategies. Both gas outlet temperature and mechanical power at different compression ratios are compared. For compression ratios typical of the hybrid power plant, represented in the graph, the deviation is insignificant. Hence, being faster as shown in Table 4.3, the first concept can be safely applied for the aim of the present model.

For both cases, the heat loss is given by:

$$\dot{Q}_{\text{loss}} = \frac{T_{\text{in}} - T_{\text{a}}}{R_{\text{REC}}} \quad (4.19)$$

Table 4.3: Computational time for the simulations of the recirculation blower with the two different strategies.

	Strategy 1	Strategy 2
Computational Time	1.05 s	18.5 s

The total thermal resistance R_{REC} is modeled through considerations based on available experimental results from a hot spin test provided by the supplier. The heat flow to the external ambient and the inlet conditions of the gas flow are known, thus the thermal resistance is calculated. Its variation with temperature is accounted for as well. Further experimental analysis would be beneficial for improving the thermal resistance's dependence with temperature. At the present moment, the accuracy of the heat loss model for the recirculation blower is at the best of the current knowledge. Further tests are going to be conducted in the DLR's test rig in early 2017 to improve the model parametrization.

4.5.3 Heat Exchanger

The heat exchanger (Figure 4.20) recovers the enthalpy of the gas turbine's outlet flow to heat up the cathode's inlet air flow.

The analysis of the heat exchanger is conducted with the efficiency method.

The efficiency of the heat exchanger is defined as the ratio between the actual rate of heat transfer and the maximum rate of heat transfer for given inlet conditions of the streams:

$$\varepsilon = \frac{\dot{Q}}{\dot{Q}_{\max}} \quad (4.20)$$

where

$$\dot{Q}_{\max} = \dot{C}_{\min} (T_{\text{h,in}} - T_{\text{c,in}}) \quad (4.21)$$

$$\dot{C}_{\min} = (\dot{m}c_p)_{\min} \quad (4.22)$$

\dot{C}_{\min} is the lowest capacity rate and $T_{\text{h,in}}$ and $T_{\text{c,in}}$ are the inlet temperature of the hot fluid and of the cold one respectively. \dot{Q}_{\max} represents the upper boundary of the heat transfer, occurring in a heat exchanger whose area approaches infinite. As a matter of fact, the cold gas can only be heated up to the temperature of the hot gas, and the hot gas can only be cooled down to the temperature of the cold gas.

In this particular case, ε is given by experimental results. When inlet conditions of the hot and cold streams are known, the actual heat transferred between them



Figure 4.20: Heat exchanger.

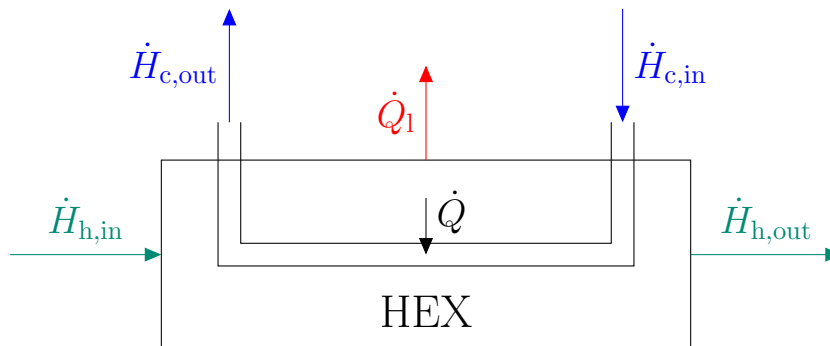


Figure 4.21: Heat exchanger schematic representation. The hot fluid in the primary circuit gives energy to the cold fluid in the secondary circuit. This, on its turn, receives energy from the hot fluid and loses energy to the environment.

is calculated through Eq. (4.21).

A schematic representation of the heat exchanger is presented in Figure 4.21. The fluid in the primary circuit exchanges energy with the one in the secondary circuit that, on its turn, exchanges energy with both fluid in the primary circuit and environment. Heat losses to the environment \dot{Q}_{loss} are computed as in Section 4.2. As the real system's parameters are implemented, the heat exchanger is composed by flat plates, so the thermal resistances are calculated as in Eq. (3.23).

The enthalpy balances on the two fluids must be respected:

$$\dot{H}_{h,\text{in}} - \dot{H}_{h,\text{out}} - \dot{Q} = 0 \quad (4.23)$$

$$\dot{H}_{c,\text{in}} - \dot{H}_{c,\text{out}} + \dot{Q} - \dot{Q}_{\text{loss}} = 0 \quad (4.24)$$

It has to be noticed that Eq. (4.23), (4.24) and Figure 4.21 are showing the case in which hot fluid is flowing in the primary circuit and cold fluid is flowing in the secondary one. The model, though, is valid in the opposite case as well, in order to being able to analyze as many different conditions as possible.

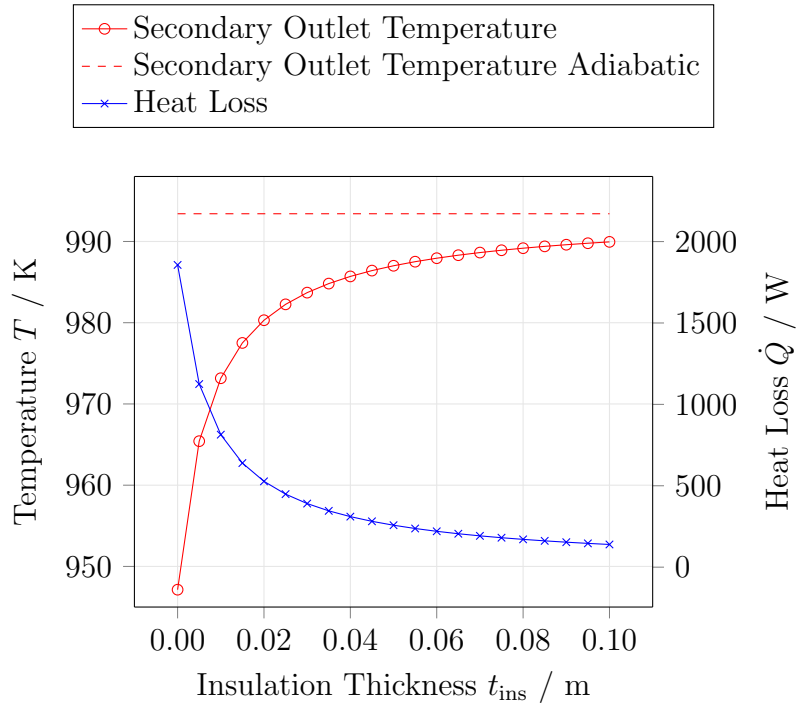


Figure 4.22: Influence of insulation thickness on secondary circuit outlet temperature and heat loss. Secondary circuit outlet temperature is compared to the one obtained when the heat exchanger is considered adiabatic.

In Figure 4.22 the influence of the heat exchanger's insulation thickness on secondary circuit outlet temperature and heat loss is shown. The dashed line represents the secondary circuit outlet temperature for a heat exchanger with absence of heat loss towards the environment. In the situation represented, which is typical of the DLR hybrid power plant operation, the influence of heat losses on the heat exchanger output can be significant.

4.5.4 Burner

In the burner, the combustion of the remaining fuel of the anode outlet flow occurs. Additional fuel can possibly be supplied when needed, for example, in the dynamic processes like start-up of the system.

Figure 4.23 shows the typical single-can configuration of the burner, on the basis of which the component has been modeled [50].



Figure 4.23: Burner with a single-can layout [50].

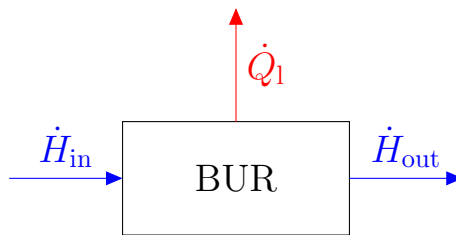


Figure 4.24: Burner (BUR) schematic representation. Heat loss from the component are included in the model.

For modeling heat losses, a tubular simplification with insulation is operated and the usual procedure described in Section 4.2 is used. A schematic representation is depicted in Figure 4.24.

In the real scenario, ambient air is flowing through a cavity at the wall and cooling it down, but all the assumptions give large uncertainties. Due to lack of information and experimental data, the assumption is made that the temperature of the internal wall of the combustion chamber is the combustion temperature which is, in its turn, given by the software Cantera [21]. In this way, a conservative analysis is being conducted by considering the maximum internal temperature.

4.5.5 Gas Turbine

The Micro Gas Turbine produces additional electrical power by means of the expansion of the products of the combustion in the burner. Furthermore, it drives the air compressor, achieving the pressurization for the pressure vessel.



Figure 4.25: 3 kW Micro Gas Turbine studied at the Institute of Combustion Technology at DLR.

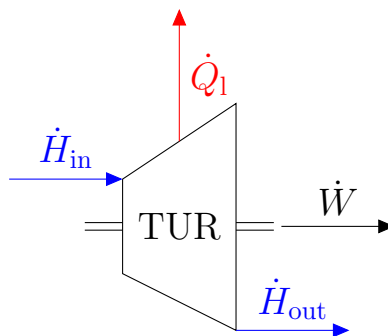


Figure 4.26: Gas turbine (TUR) schematic representation. Heat flow lost towards the environment is included.

At DLR, a 3 kW MGT is being studied by the Institute of Combustion Technology at DLR (Figure 4.25). The aim of this analysis is to create a fast and reliable

model for heat losses from the component. The schematic representation of the energy flows occurring in the component is depicted in Figure 4.26. The enthalpy balance on the gas flow that must be applied is:

$$\dot{H}_{\text{in}} - \dot{H}_{\text{out}} - \dot{W} - \dot{Q}_{\text{loss}} = 0 \quad (4.25)$$

For the evaluation of heat losses, the following assumptions are made:

- A tubular simplification is proposed;
- The heat loss model described in Section 4.2 regarding tubes and cylindrical geometries is applied;
- The strategy used for analyzing the compression process in the recirculation blower (Section 4.5.2) is here adapted as well. It is possible to do so due to the low deviation between the two methods described, as it is shown in Figure 4.27 (for REC, Figure 4.19).

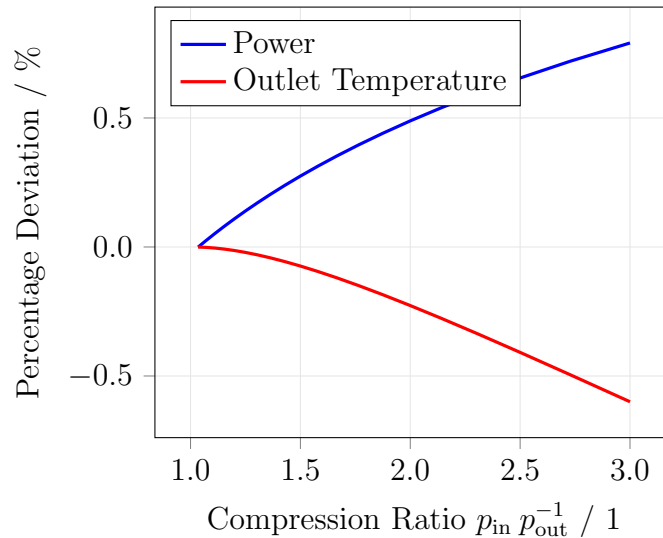


Figure 4.27: Percentage deviation of outlet temperature and mechanical power of the gas turbine between the two modeling strategies.

Analyzing a typical situation of the hybrid power plant, the heat losses obtained with the above-mentioned simplifications are comparable with values from literature [48]. Indeed, a numerical study of heat transfer in Micro Gas Turbines of different sizes is made performing detailed 3D analysis. The values given have the same order of magnitude as the results of the 0D model for this section.

4.5.6 SOFC Stack Modules

The details about the electrochemical processes that occur in the SOFC stack modules and generate the operating temperature are widely analyzed in literature and in the global system models previously implemented in the Institute of Engineering Thermodynamics at DLR [22]. The SOFC thermodynamic model is not included in the present thesis, as the focus of the work is the identification and modeling of thermal losses from the various components.



Figure 4.28: SOFC Stack Modules for the hybrid power plant at DLR. On the front side, the tubes that take the gas flows in and out of both anode and cathode can be noticed. On the bottom of the SOFC box, the sensors compartment is visible.

Therefore, the SOFC stack modules, represented in Figure 4.28, are considered as boxes made of isothermal flat plates, whose temperature is the operating one and constitutes the boundary condition. Hence, heat losses are calculated as in Section 4.2. Insulation of the SOFC stack modules is implemented as a parameter of the real system.

Special attention is paid to the bottom side of the stacks, that is directly connected to the sensors compartment, as shown in Figure 4.29. According to the supplier, this must be kept at a temperature lower than 100 °C, in order not to damage the measurement devices for the parameters of the processes.

$$\dot{Q}_{\text{SEN}} = \frac{T_{\text{SOFC}} - T_{\text{max,SEN}}}{R_{\text{SEN}}} \quad (4.26)$$

It is assumed that heat lost to the sensors compartment, given by Eq. (4.26), goes

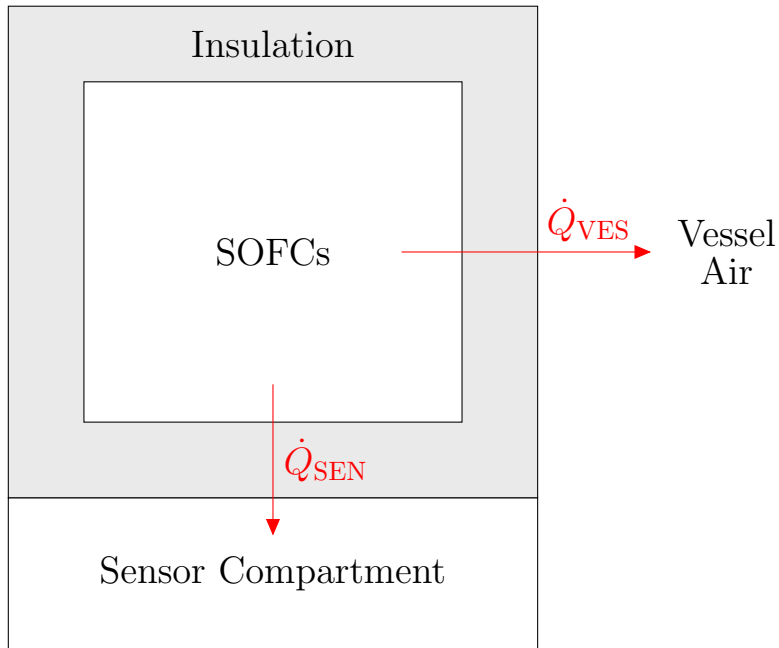


Figure 4.29: SOFC Stack Module schematic representation. Heat is directly lost from the bottom of the stacks to the Sensor Compartment (\dot{Q}_{SEN}) and from the other sides to the pressure vessel’s fresh air (\dot{Q}_{VES}).

to the ambient through the cooling air for the sensors, that is not recirculated anywhere else in the system. Instead, the heat lost from the other sides of the SOFC stacks is given to the vessel’s fresh air, which is afterwards provided to the heat exchanger.

The model of the SOFC stack modules needs to be coupled to the model of the pressure vessel, as it is described in Section 4.5.7.

The value of the total heat losses from the SOFC stack modules obtained with the detailed analysis here described is compatible with previous analysis performed at DLR.

4.5.7 Pressure Vessel

The pressure vessel’s aim is to allow the gas turbine operation by giving a difference of pressure. The gas turbine, in its turn, furnishes preheated air to the SOFCs placed inside the vessel itself. In the mean time, the vessel slightly increases the efficiency of the SOFC stacks permitting the pressurized operation.

It contains the reformer, the recirculation, the SOFCs themselves and the connecting pipes (Figure 4.30).

Fresh air is compressed by the air compressor and then led inside the pressure



Figure 4.30: Open pressure vessel during fabrication.

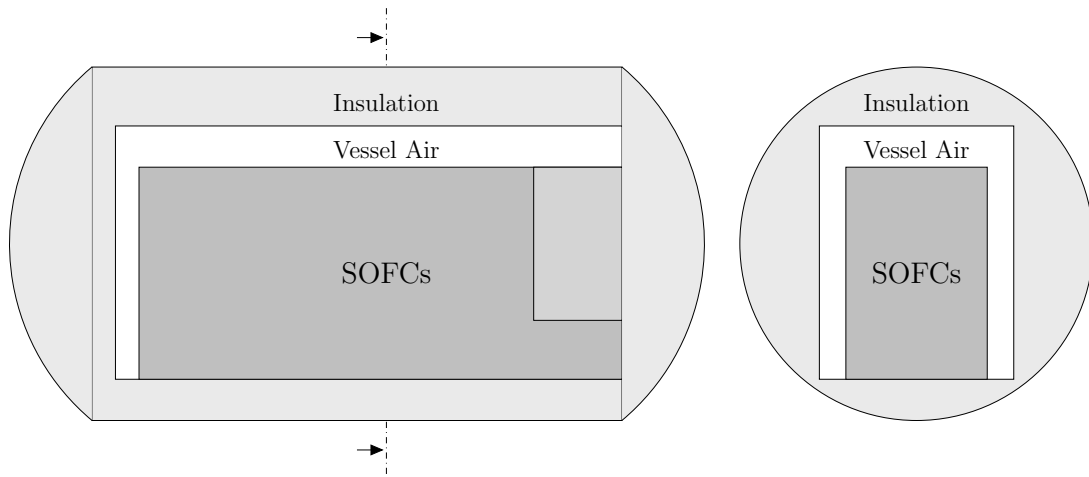


Figure 4.31: Sketch of the pressure vessel's inside, considered as a set of flat plates.

vessel, where its temperature is increased while the SOFC stack modules are kept at the operating temperature. The following heat transfer processes are included in the model:

- Heat transfer from SOFC to fresh air: \dot{Q}_{SOFC} , as explained in Section 4.5.6;
- Heat transfer from connecting pipes located inside the vessel, including the reformer, to fresh air: \dot{Q}_{tbs} . This value is given by the sum of the heat losses of those components;
- Heat loss from fresh air to outside: \dot{Q}_{loss} . This value is obtained with the usual procedure described in Section 4.2 and with some assumptions. The inside of the pressure vessel is considered as a set of flat plates (Figure 4.31), so the correspondent heat transfer coefficient is used. In order to maintain the zero-dimensional simplification, an equivalent insulation thickness is implemented for the entire surface of the vessel.

The enthalpy balance on the cooling air inside the vessel used to compute heat losses and outlet conditions is the following:

$$\dot{H}_{\text{in}} - \dot{H}_{\text{out}} + \dot{Q}_{\text{SOFC}} + \dot{Q}_{\text{tbs}} - \dot{Q}_{\text{loss}} = 0 \quad (4.27)$$

Later in this document, the different heat loss models are compared through the simulation of a typical situation. In particular, rough values of the total heat losses from the components are reported in Section 5.6.

5 Discussion and Results

In this Section, the different model paradigms previously described are compared and the results of the simulations are shown.

A test tube that represents a typical situation for the hybrid power plant at DLR, with a double layer of insulation and an air flow with a inlet temperature of 1125 K, is considered. Its characteristics are summarized in Table 5.1. The materials used are reported in Table 5.2.

Table 5.1: Characteristics of a test tube typical of the hybrid power plant, used to compare the different model paradigms.

	Unit	Value
Inlet Air Temperature	<i>K</i>	1125
Inlet Air Pressure	<i>MPa</i>	0.3
Inlet Molar Flow	<i>g/s</i>	50
Tube Diameter	<i>mm</i>	100
Tube Thickness	<i>mm</i>	3
Tube Length	<i>m</i>	10
First insulation thickness	<i>mm</i>	50
Second insulation thickness	<i>mm</i>	50

Table 5.2: Materials of the test tube.

	Material
Tube	Stainless Steel 1.4828
First Insulation	Silcapor Ultra 950
Second Insulation	Rockwool ProRox LF 970

5.1 Comparison 2D vs 1D

According to the two-dimensional approach described in Section 4.2, the tube is discretized along its axis (direction z) and along the radius (direction r) with the following parameters, so that the variation of temperature and of the properties

in those two directions is considered:

$$\Delta z = 1 \text{ cm}$$

$$\Delta r = 1 \text{ mm}$$

In Figure 5.1 the distribution of temperature in two different cross-sections of the tube is shown.

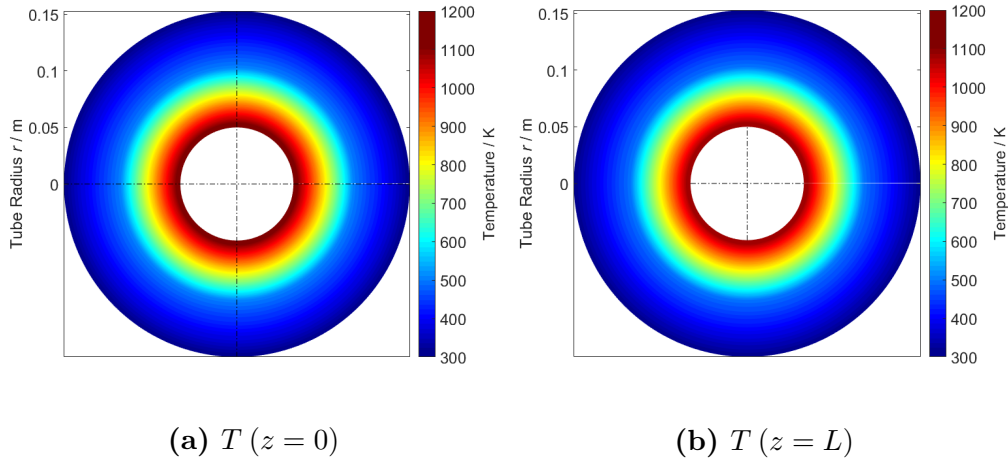


Figure 5.1: Distribution of temperature in two different cross-sections (beginning and end) of a test tube.

Two cross-sections at the two opposite sides of the system have been chosen, in order to understand the influence of the position in the axial direction. It is possible to notice that the distribution of temperature is basically the same in the two cross-sections.

The values are shown more precisely in Figure 5.2: the difference of temperature between the two ends of the tube in the axial direction is orders of magnitude lower than the difference of temperature in the radial direction. For this reason, the axial heat flow through the materials is not significant compared to the radial heat flow to the external ambient.

Another consideration can support this statement: the thermal resistance in the axial direction between the two sides of the tube is higher due to the high length and the small conductive area. A high thermal resistance, together with a low temperature difference, makes it reasonable to neglect the contribution of the heat flow in the axial direction of the tube.

According to the black-box approach of the global model, the results of interest for the analysis are the outlet temperature of the gas stream and the heat flow to

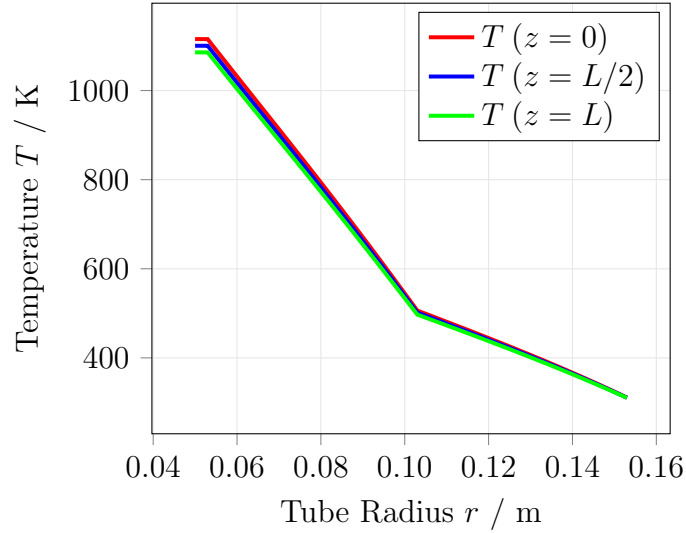


Figure 5.2: Distribution of temperature in the radial direction at the beginning, in the middle and at the end of the tube.

the environment. The distribution of temperature in the system is not required and should be highlighted only if it gives significantly different outputs. For example, the material properties change with temperature (Section 4.1), so its distribution can affect the final results and should be considered.

Though the two-dimensional approach is accurate, as it accounts for the cooling of the gas along the tube and for the variation of the properties in the axial direction, it is also computationally heavy. Table 5.3 shows the results of the simulation made with a 2D model compared with the results of a 1D model with only the radial discretization.

Table 5.3: Comparison of the results obtained with a 2D and a 1D model (radial discretization).

		2D model	1D model	Deviation
Gas Outlet Temperature	K	1115.5	1115.5	$< 0.01\%$
Heat Flow	W	1281	1282	$< 0.01\%$
Computational Time	s	71.6	0.745	

It is clear that the deviation between the result of the 2D model and the result of the 1D model is not relevant, while instead the difference in computational time is huge. In this analysis, it is not necessary to consider the axial variation of the properties. Therefore, the two-dimensional approach can be put aside, as it is too

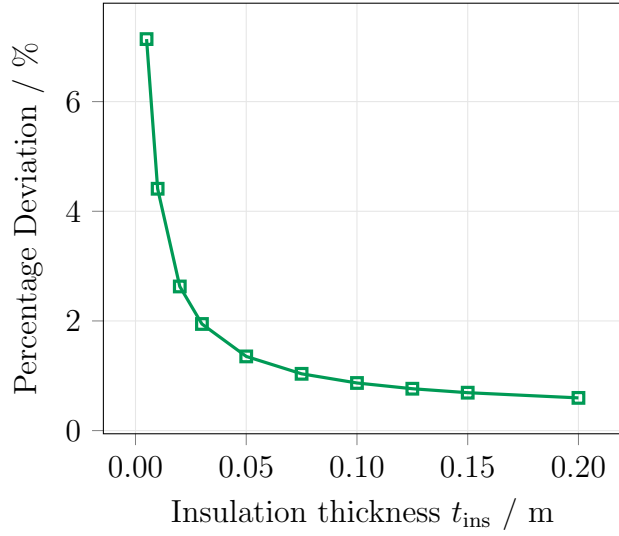


Figure 5.3: Percentage deviation of the maximum temperature difference along the tube: comparison of the inlet and outlet cross-sections.

computationally expensive.

To further affirm these considerations, a sensitivity analysis on the insulation thickness is performed. In fact, a higher ΔT due to a higher heat flow to the environment might give a different effect. The maximum temperature difference in the materials between the two opposite cross-sections is shown in Figure 5.3.

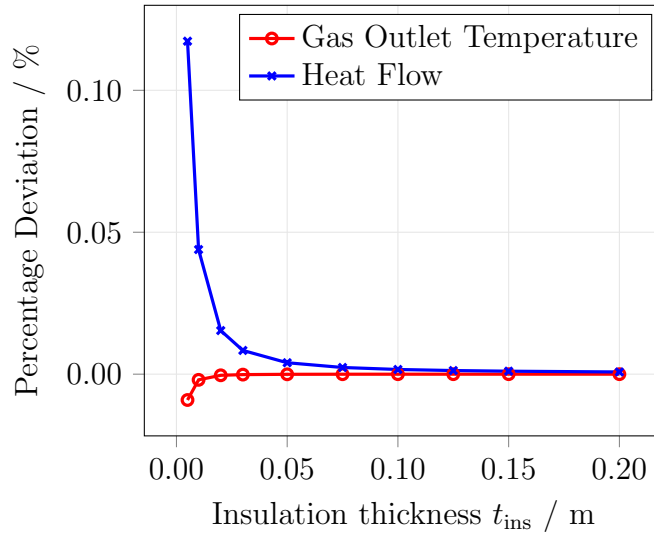


Figure 5.4: Deviation between the results of the 2D and 1D models with varying insulation thickness.

The deviation is kept under 8% even for lower values of insulation thickness. This

does not significantly affect the results of the model. The deviation between the results of 2D and 1D approaches, presented in Figure 5.4, is acceptable for this analysis.

5.2 Comparison 1D vs 0D

It's been proved that the axial discretization is not necessary for maintaining a feasible accuracy of the results.

Nonetheless, the temperature varies significantly in the radial direction, where it spreads from the gas inlet temperature that can typically reach 1125 K to the ambient one of around 300 K. In order to understand if a further speed up of the calculation is possible, a radially discretized one-dimensional approach is compared to the zero-dimensional one.

It has been previously explained (Section 4.2.3) that different ways of computing the 0D model have been presented and applied. These approaches differ on the choice of the temperatures used to evaluate the material properties. They are summarized again in Table 5.4.

Table 5.4: Zero-dimensional approaches.

Model	Abbreviation	Description
Worst Case Scenario	WCS	Properties of each material are evaluated at the temperature of the hottest surface.
Best Case Scenario	BCS	Properties of each material are evaluated at the temperature of the coldest surface.
Arithmetic Mean	ARI	The chosen temperature is the arithmetic mean between the two surfaces of each material.
Neutral Face Discretization	NFD	The temperature is evaluated at the neutral surface of each layer.
Logarithmic Mean	LOG	The chosen temperature is the logarithmic mean between the two surfaces of each material.

The results obtained by the simulation of the test tube with these different approaches are again compared. In Figure 5.5 the gas outlet temperature, the

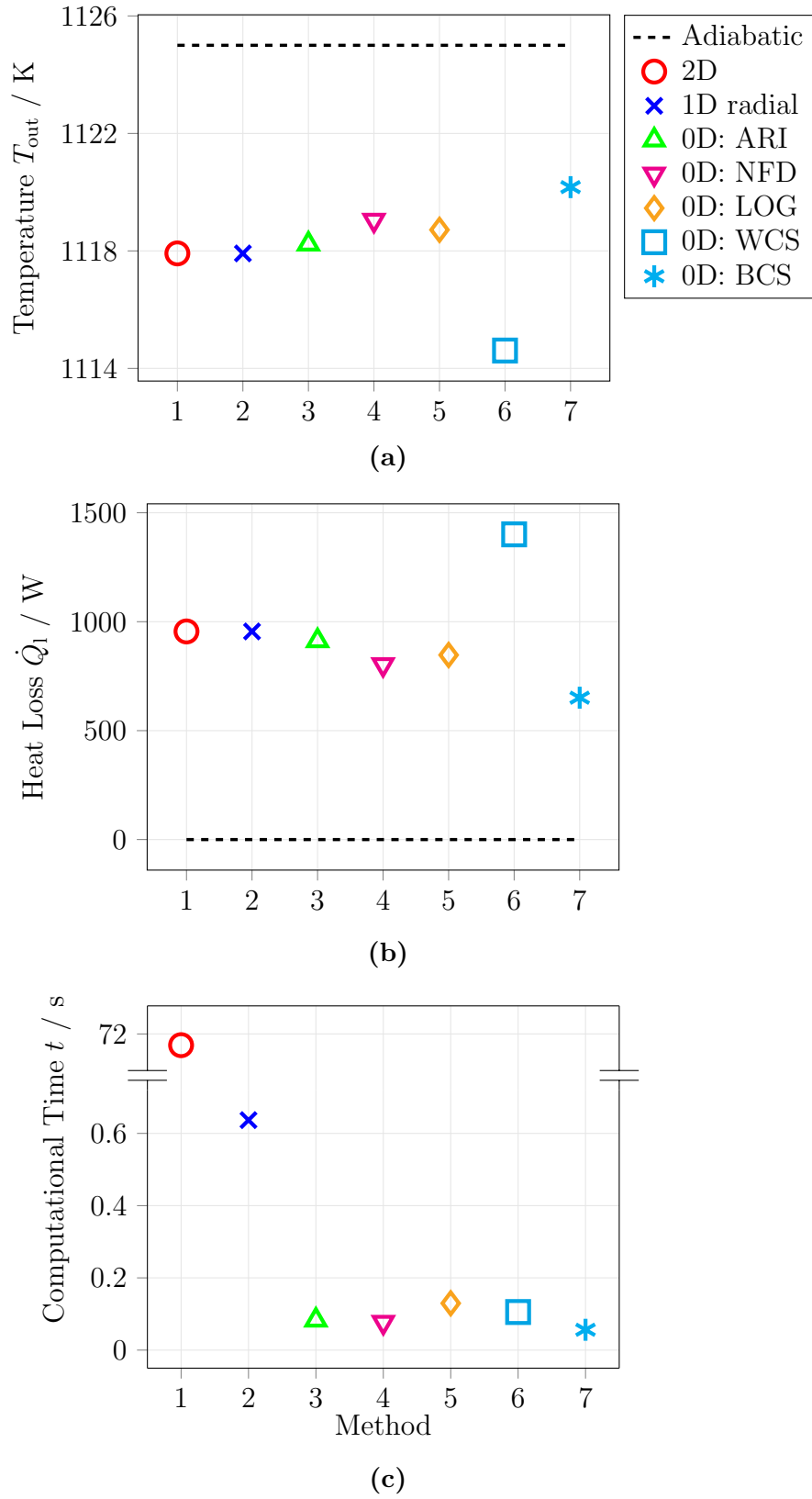


Figure 5.5: Comparison of the outlet temperature (a) heat loss (b) and computational time (c) of a test tube with different model approaches.

heat loss and the computational time are shown. The difference between the computational time of the two-dimensional and one-dimensional models has already been shown in Section 5.1, so it is not recalled here.

The graphs affirm that using a zero-dimensional model for computing the heat losses of the system is feasible. The gain in computational time is relevant, as the radially discretized 1D model is an order of magnitude slower than the 0D ones. Simultaneously, a feasible accuracy is maintained. Table 5.5 sums the accuracy deviation up.

Table 5.5: Deviation of the results of the 0D models from the 1D.

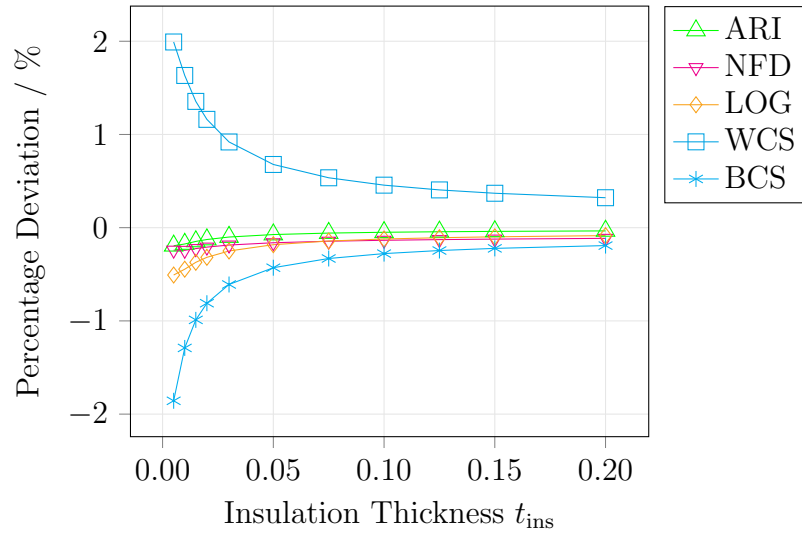
Model	Outlet Temperature Deviation	Heat Loss Deviation
	%	%
ARI	−0.028	2.1
NFD	−0.1	8.9
LOG	−0.029	6.5
WCS	−0.2	27.3
BCS	0.3	16.2

The 0D model that gives results closer to the more accurate 2D and 1D ones is the ARI. Additionally, it predicts a higher heat flow compared to the other 0D models, hence allowing to be on a safe side. The WCS and BCS predict the upper and lower boundaries of the solution respectively, that are the higher and lower heat losses.

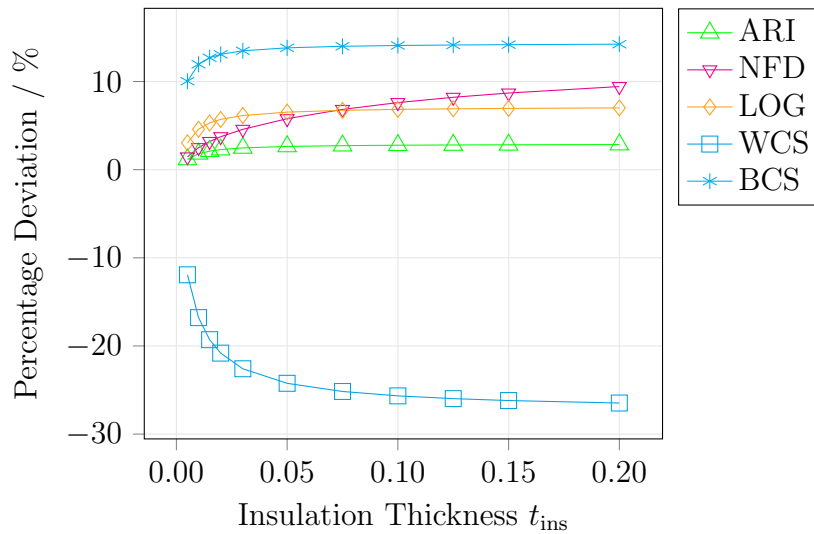
A sensitivity analysis based on the variation of the insulation thickness is performed to affirm this choice (Figure 5.6). The behavior of the curves can be explained as follows:

- Outlet temperature (Figure 5.6a): while the insulation thickness decreases, the outlet temperature decreases as well due to the lower thermal resistance. Hence, the influence of the model approach grows;
- Heat loss (Figure 5.6b): the difference between the models decreases if the insulation thickness go to zero, as the calculation of the temperatures becomes approximately the same.

The model that applies the concept of the arithmetic mean is the one that maintain a deviation of the heat loss lower than 3% and therefore is considered for the global model.



(a)



(b)

Figure 5.6: Percentage deviation of outlet temperature (a) and heat loss (b) with varying insulation thickness: comparison of different 0D models in respect of the 1D model.

5.3 Implementation of Gas Mean Temperature

A further comparison must be done to conclude the stationary analysis. The zero-dimensional solution process evaluates the heat losses on the basis of the gas mean temperature, as this cools down while flowing through the tube or the component.

Two possible ways to evaluate the gas mean temperature over its path have been implemented:

1. Arithmetic mean as in Eq. (5.2);

$$T_{\text{gas}} = \frac{T_{\text{in}} + T_{\text{out}}}{2} \quad (5.2)$$

2. Logarithmic mean.

$$T_{\text{gas}} = \frac{T_{\text{in}} - T_{\text{out}}}{\log(T_{\text{in}}) - \log(T_{\text{out}})} \quad (5.3)$$

Figure 5.7 and Table 5.6 show that, while the accuracy does not see any changes, the computational speed is neatly in favor of the arithmetic mean. This happens also for very low values of insulation thickness, for which the difference of temperature is more relevant. This latter way of computing the gas mean temperature along the component is therefore chosen.

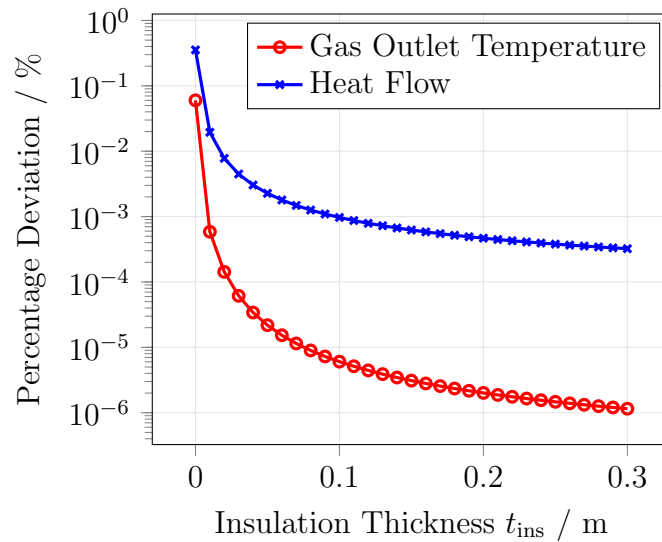


Figure 5.7: Deviation between the results obtained using arithmetic mean and logarithmic mean as gas mean temperature for different values of insulation thickness.

Table 5.6: Computational time for the simulations with arithmetic mean and logarithmic mean as gas mean temperature.

	Arithmetic Mean	Logarithmic Mean
Computational Time	2.0 s	2.9 s

5.4 Comparison with Experimental Results

In order to verify the results provided by the different models proposed, they are compared with experimental data gathered at the Institute of Combustion Technology (VT) at DLR. The experiment has been performed on a tube with the characteristics summarized in Table 5.7. A set of measurements of the outlet gas temperature has been done with different initial flow conditions.

Table 5.7: Characteristics of the tube used to perform experimental measurements at the Institute of Combustion Technology.

	Unit	Value
Tube Diameter	<i>mm</i>	162
Tube Thickness	<i>mm</i>	3
Tube Length	<i>m</i>	2.486
Tube Material		Stainless Steel 1.4828
Insulation Thickness	<i>mm</i>	100
Insulation Material		Asglasil

The same conditions are simulated with the different model approaches and the results are compared in Figure 5.8. The WCS and BCS represent the boundaries of the solution, as expected. The experimental measurements are included in this interval. Considering that the models account for a perfect insulation, the deviation from the experimental data, which are obtained in non perfect conditions, is reasonable. The insulation imperfection could be due to non perfect construction and assembly as well as to the degradation of the properties of the material. It is artificially simulated through the ARI approach by increasing the thermal conductivity of a certain percentage. A sensitivity analysis on the insulation imperfection (IMP) is done in Figure 5.9.

The behavior of the results predicted by the models matches that of the experiments, considered the severe differences in the boundary conditions throughout

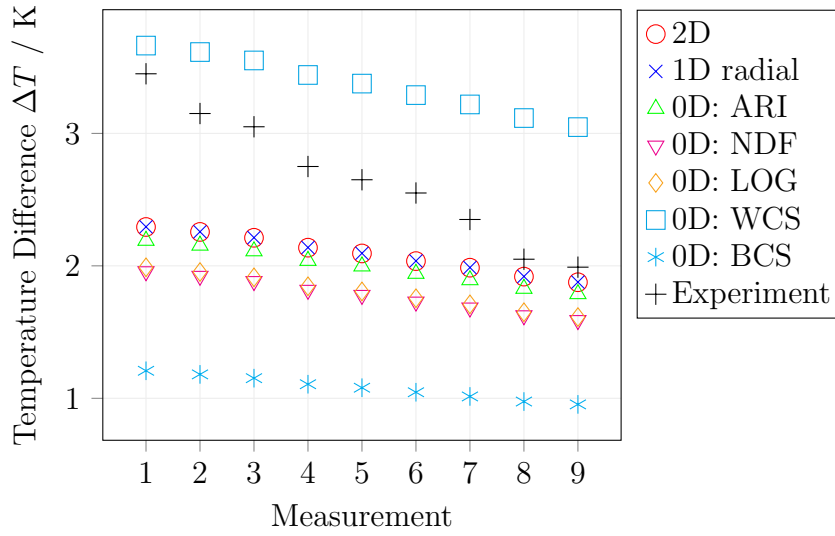


Figure 5.8: Gas temperature difference between inlet and outlet: comparison of the different models with the experimental measurements performed by the Institute of Combustion Technology.

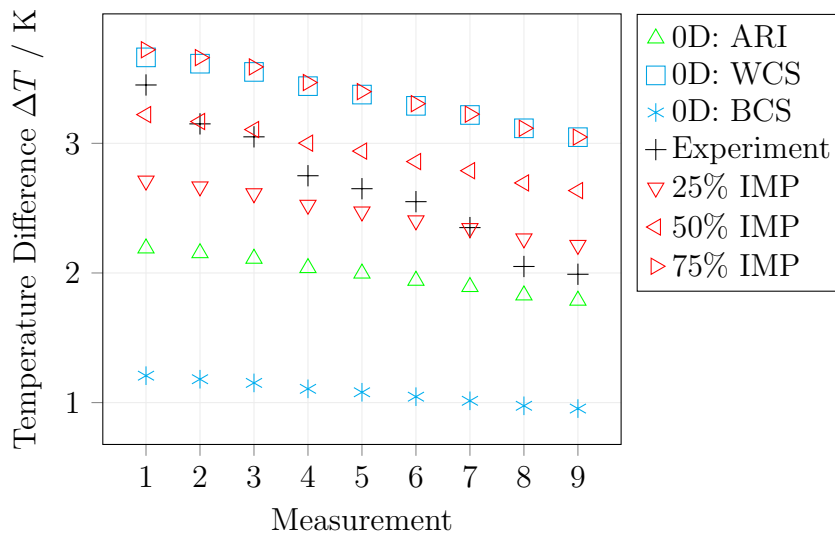


Figure 5.9: Gas temperature difference between inlet and outlet: sensitivity with insulation imperfection and comparison with the experimental measurements.

the tests. Therefore, the models can be considered validated for the purpose of the present work. Nonetheless, further experiments would be beneficial to confirm this statement.

5.5 Stationary vs Transient

In transient processes, the knowledge of the distribution of temperature can be beneficial to investigate the role of the materials as a storage capacity. The temperature of the storage system at a given time-step is obtained.

The simulations have been run with the assumptions discussed in Section 4.3. For the zero-dimensional transient model, the storage system temperature is considered as the temperature of each material layer, evaluated in the neutral face. Though the approach has no dimension, the same concept as in the stationary analysis is applied. Each material layer of the tube is considered as a finite volume and the grid points for the evaluation of the variables are centered in each of these volumes.

The simulation is conducted for the test tube described at the beginning of Section 5. The following additional parameters are given:

- Initial condition: the entire system is at ambient temperature at the beginning of the time scale ($t = 0$);
- Time-step: $\Delta t = 10$ s.

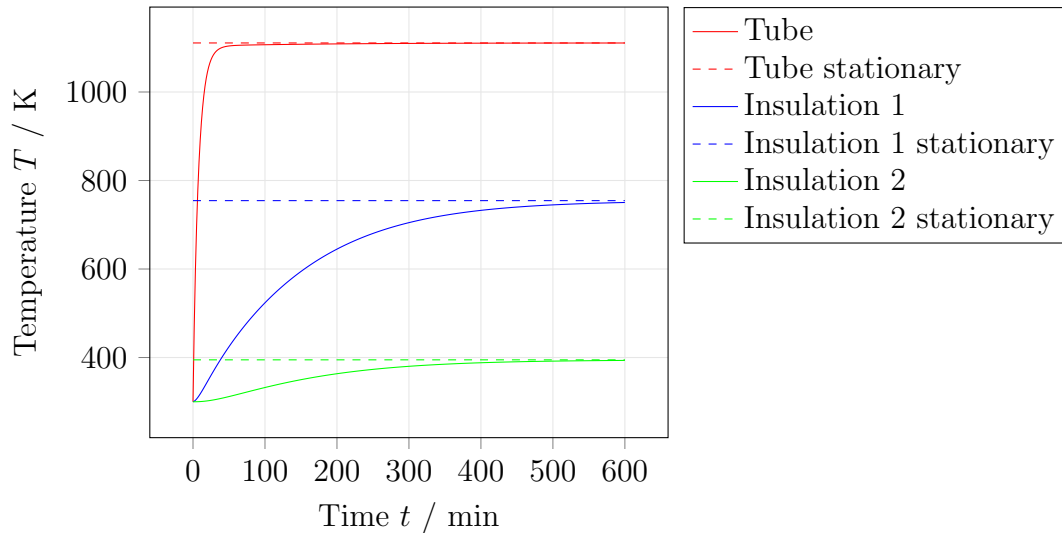


Figure 5.10: Temperature of the materials over time.

Figure 5.10 represents the distribution of temperature of the materials over time. The temperatures obtained with the stationary model are also shown.

The results of the computation are reasonable. Each material is heated up, due to the heat transferred by the gas flow, at different rates depending on the heat capacity. To be more specific, the stainless steel tube has a lower heat capacity due to the smaller volume so its temperature gets higher faster, while the insulation layers have a much bigger heat capacity and therefore their heating rate is slower. After a certain time, the system reaches a steady-state: the values of temperature obtained in this case are the same as calculated with the stationary model. This means that the models are coherent.

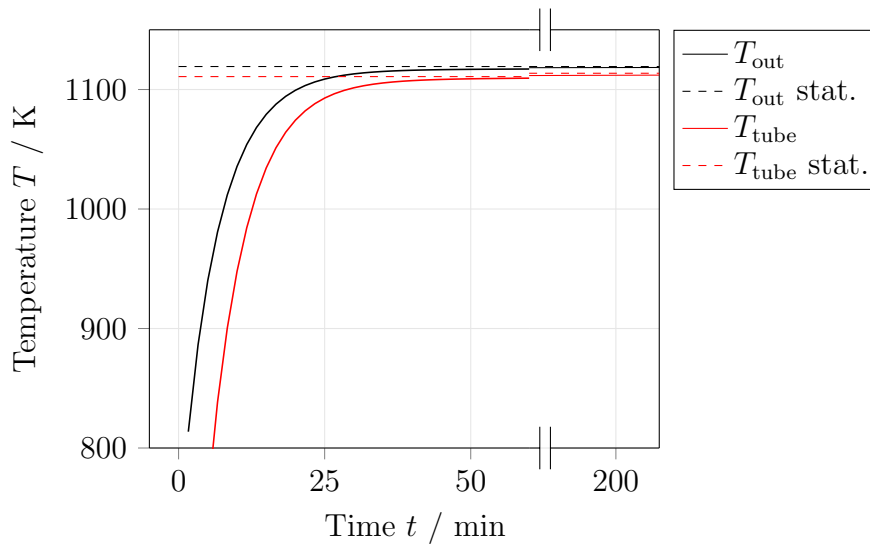


Figure 5.11: Gas outlet temperature over time.

The evolution of the gas outlet temperature over time, depicted in Figure 5.11 is reasonable as well. At the beginning of the time scale, a significant amount of energy is transferred towards the outside, as the materials are at ambient temperature. While energy is being stored in their capacity, their temperature increases and the heat lost by gas flow gets lower. Eventually, the steady-state is reached.

As expected, the time-step does not influence the solution in a relevant way. The implicit solution method recalled in Section 3.2 allows to maintain stability for every time-step. A comparison of three different time-steps is made in Figures 5.12 and 5.13 where the deviation of the temperatures in respect of a time-step of 1 s is depicted. While the deviation of the material temperature is not significant, a slightly bigger difference concerning the gas temperature can be detected for the first time-steps. That is due to the fact that, at the beginning, the fluid has a fast

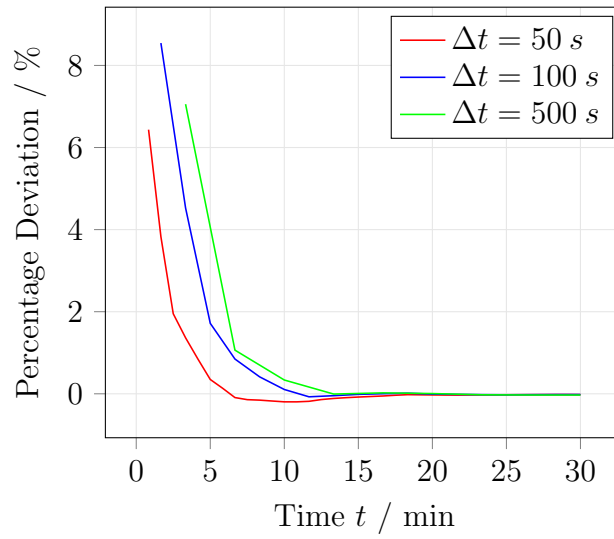


Figure 5.12: Influence of the time step on the percentage deviation of the gas outlet temperature: comparison with $\Delta t = 10$ s.

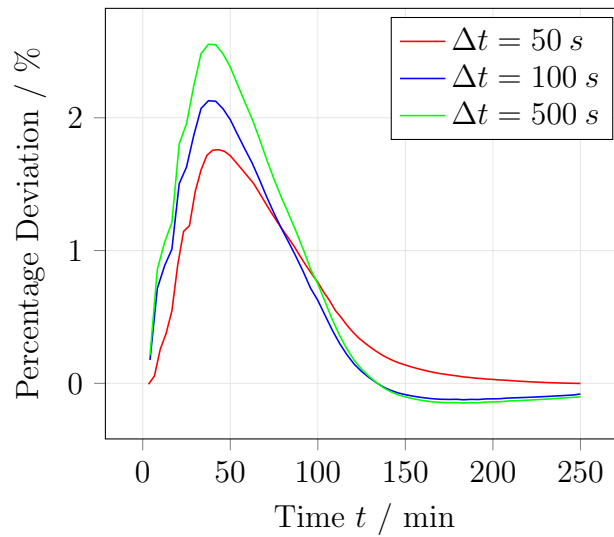


Figure 5.13: Influence of the time step on the percentage deviation of the material temperature: comparison with $\Delta t = 10$ s.

dynamic that can not be fully appreciated with a bigger time-step.

Analogue considerations can be done concerning the goodness of the zero-dimensional transient model, compared to a multi-dimensional one. Figure 5.14 shows the influence of the model approach on the prediction of the gas outlet temperature for the test 10-m-long tube. The following approaches are compared:

- Zero-dimensional model;
- One-dimensional model with radial discretization, to investigate the role of the distribution of temperature towards the environment;
- One-dimensional model with axial discretization, to account for the cooling down of the gas flow along the tube;
- Two-dimensional model, to consider both the above-mentioned aspects.

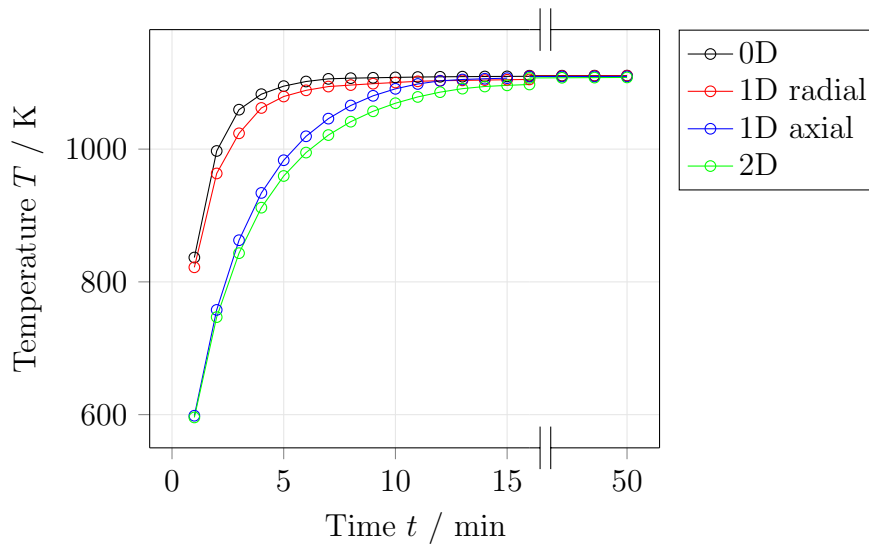


Figure 5.14: Gas outlet temperature over time: comparison of different models ($L = 10\text{ m}$).

It is possible to notice that, at the very beginning of the time scale, the 0D simplification differs quite significantly from the more accurate but computationally expensive 2D model. While the radial does not play a big role in this difference, the axial discretization considers a variable temperature. This factor drives the solution especially for higher tube lengths, where the effect of gas cooling is stronger.

The difference becomes relevantly smaller for shorter components (i.e. 1-m-long tube in Figure 5.15).

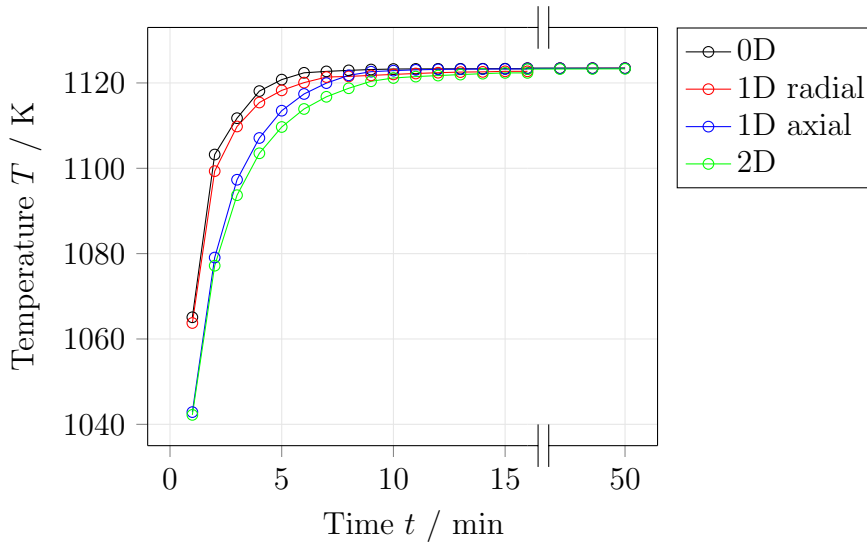


Figure 5.15: Gas outlet temperature over time: comparison of different models ($L = 1 m$).

If a better accuracy at the beginning of the time scale is required, it can be beneficial to consider a 1D approach for the first set of time-steps and then skip to a 0D simplification as soon as a steady-state is reached. It is a matter of finding, from time to time, the right compromise between the accuracy and the computational speed. However, in the hybrid power plant, the lengths of interest are below $10 m$. Hence, the 0D approach is applied as it gives good results.

5.6 Adiabatic vs Non-Adiabatic

As shown in Section 5.2, a zero-dimensional model for heat losses is chosen and applied to the components of the system previously described. In the interests of brevity, the results of the simulations performed with the proposed models have been shown for the cylindrical geometry of a tube. Entirely comparable considerations can be done for all the components.

The non-adiabatic layout of the global model of the hybrid power plant is represented in Figure 5.16. For a comparison with the old scheme, see Figure 4.2. The global model gains in both complexity and accuracy and the study of a large number of situations is now possible. In fact, in spite of the high number of components and the loop-type interactions between them, the solution of each stationary point of the hybrid power plant is possible in less than 10 seconds with a standard office computer. As it is shown previously in this Section, this would not have been achievable with a different modeling strategy.

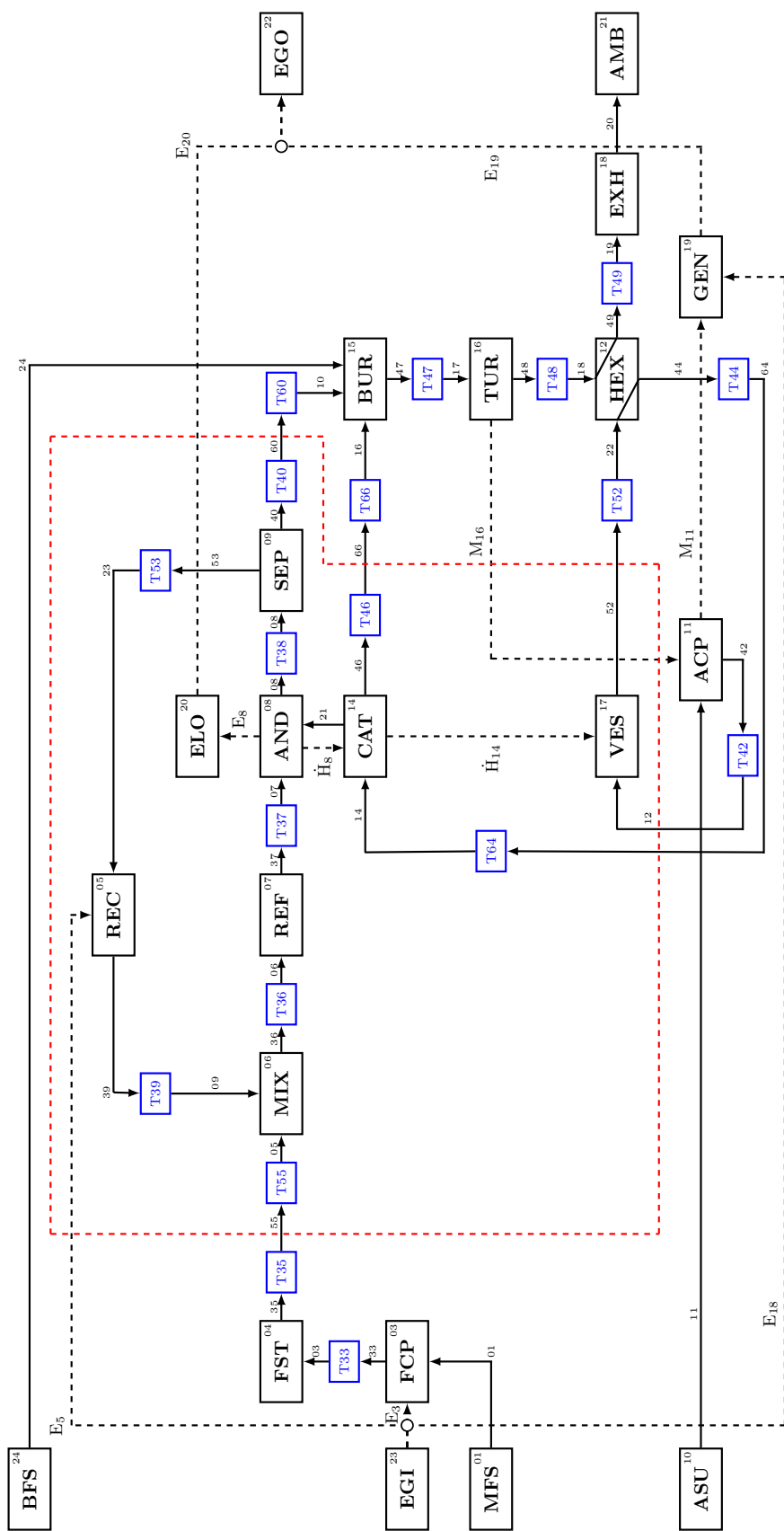


Figure 5.16: Hybrid power plant global model non-adiabatic concept. The blue boxes represent the connecting tubes. The red dashed line represents the boundaries of the pressure vessel. For the meaning of the abbreviations, see Nomenclature.

To give an idea of the impact of the non-adiabatic concept, rough numbers obtained from the simulation of the system in a typical stationary situation are given.

Table 5.8: Heat losses from the components of the hybrid power plant as predicted by the model.

Component	Heat Loss
	<i>kW</i>
Tubes	1.0
Reformer	0.1
Recirculation Blower	0.7
Heat Exchanger	0.5
Burner	0.4
Gas Turbine	0.2
SOFC Stack Modules	2.5
Pressure Vessel	0.6
Total Heat Losses	6.0

An approximate first consideration on the system can be done. Assuming an overall efficiency of 50%, an input energy flow of 60 kW in the form of chemical energy of the fuel is necessary to reach the desired output power of about 30 kW. The heat losses play a relevant role as they amount to the 10% of the inlet energy.

For future developments, it is therefore beneficial to carry on with this analysis and investigate further the role of heat losses and heat capacities as thermal storage system in the global operation of the hybrid power plant. It could be of interest to understand the maximum heat losses allowed in the operating range of the plant, in order to provide considerations on the design as well as on the insulation assembly.

A detailed sensitivity analysis on the relevant parameters of the hybrid power plant will be carried out in a later work.

6 Conclusions

The purpose of this thesis, as presented at the beginning of the document, was the development of heat loss models for the components of the DLR SOFC/GT hybrid power plant, aimed at being used in the global system simulation.

As the current overall system model is adiabatic, the inclusion of heat losses of the system itself will give the chance to improve the prediction of the operating range and the knowledge of the components temperature. This could be beneficial for the prevention of undesired operating problems of the power plant.

Furthermore, the consideration of the system's thermal capacity will allow for a more detailed prediction of the transient processes, since the role of the materials a thermal storage system will be investigated. The study of start-up, shut-down and load changes as well as new possible operating strategies for the hybrid power plant will therefore be a real chance.

In order to select the modeling approach that realizes the best compromise between accuracy and computational speed, the basics of computational heat transfer have been applied to develop a series of multi-dimensional models of the heat losses from an insulated tube. Various 2D, 1D and 0D models characterized by different assumptions regarding the parameters distribution have been built in MATLAB environment and compared.

Satisfactory results have been obtained through the zero-dimensional model that considers an arithmetic mean temperature for the evaluation of the system properties and parameters. The results obtained for the sample case differ from the more detailed 2D and 1D models of a maximum of 2% concerning the heat lost to the environment, while the computational speed is orders of magnitude higher. Additional mathematical and conceptual simplifications, such as the use of the Horner's method for computing polynomials, has allowed for the speeding up of the solution process. Moreover, a good agreement with a set of experimental measurements has been found to testify the goodness of the model.

The 0D heat loss concept has been further applied to the other components of the hybrid power plant (i.e. reformer, recirculation blower, heat exchanger, burner, gas turbine, SOFC and pressure vessel). Similar considerations have been repeated and coherent results have been found.

Hence, the mentioned 0D strategy respects entirely the initial requirements of the analysis. It has been chosen and implemented, permitting the solution of each stationary point of the complex global model in less than 10 seconds with a standard office computer.

Eventually, the simulations have been made transient: new components models have been built with the inclusion of the real system's thermal capacities and the discretization of the time scale. The coherence of the transient models has been affirmed through the comparison with the stationary model, as the distribution of temperature converges precisely to the steady-state results.

A complete set of fast and reliable sub-models is now available for the integration in the global system simulation. Both steady-state and transient operation of the SOFC/GT hybrid power plant will be thoroughly investigated. A detailed and accurate comparison of the results obtained with the adiabatic and non-adiabatic approaches will be carried out as well as a sensitivity analysis on the relevant parameters of the hybrid power plant. The outcome of this study will be published in order to permit a better understanding of the operation of the SOFC/GT hybrid power plant.

Acknowledgements

First of all, I would like to thank my supervisor, Mike Steilen, for teaching me so much, advising me in every stage of my thesis work and trusting in my capabilities. This work would not have been possible without his thorough attention and determinant support.

I thank all the other researchers at DLR for giving me the opportunity to contribute to this research topic and sharing with me part of the everyday life in Germany. Special thanks to Syed Asif Ansar, Marc Heddrich, Moritz Henke, Christian Sch-negelberger, Marius Tomberg, Marc Riedel and Srikanth Santhanam.

I would like to express all my gratitude to Prof. Umberto Desideri for allowing me to carry out this work in another country and for his essential guidance towards the future.

I also thank Prof. Claudio Casarosa for his precious advices throughout my educational path.

From the deepest of my heart, thanks to all the incredible people that have walked with me during this journey, remembering me every day that happiness is only real when shared.

To Elena, for our ten years of unconditional friendship. To Francesco, for his loyalty and support. To Serena, for being so close despite the distance. To my amazing group of friends, le Comari, for their affection and encouragement.

Most of all, thanks to my Family, for being with me in every choice and every mistake. All I am today, all I have accomplished so far, I owe it to them.

To Dad, my greatest inspiration.

To Mum, my greatest strength.

To my sister Virginia and my brother Riccardo, for sharing with me the greatest love of all.

And to Nicola, who has stuck with me until the very end.

References

- [1] VDI - Gesellschaft Verfahrenstechnik und Chemieingenieurwesen: *VDI - Waermeatlas*, 1991.
- [2] E. Achenbach. Response of a Solid Oxide Fuel Cell to a Load Change. *Journal of Power Sources*, 57:105–109, 1995. doi: 10.1016/0378-7753(95)02263-5.
- [3] L. Barelli, G. Bidini, and A. Ottaviano. Part load operation of SOFC / GT hybrid systems : Stationary analysis. *International Journal of Hydrogen Energy*, 37(21):16140–16150, 2012. doi: 10.1016/j.ijhydene.2012.08.015.
- [4] L. Barelli, G. Bidini, and A. Ottaviano. Part load operation of a SOFC / GT hybrid system : Dynamic analysis. *Applied Energy*, 110:173–189, 2013. doi: 10.1016/j.apenergy.2013.04.011.
- [5] A. Bejan. *Convection Heat Transfer*. John Wiley & Sons, Inc., 2013. ISBN 978-0-470-90037-6.
- [6] R. Bove and S. Ubertini. Modeling solid oxide fuel cell operation: Approaches, techniques and results. *Journal of Power Sources*, 159(1 SPEC. ISS.):543–559, 2006. doi: 10.1016/j.jpowsour.2005.11.045.
- [7] R. Bove, P. Lunghi, and N. M. Sammes. SOFC mathematic model for systems simulations. Part one: From a micro-detailed to macro-black-box model. *International Journal of Hydrogen Energy*, 30(2):181–187, 2005. doi: 10.1016/j.ijhydene.2004.04.008.
- [8] J. Brouwer. Hybrid Gas Turbine Fuel Cell Systems. In *The Gas Turbine Handbook*, chapter 4, pages 127–163. U.S. Department of Energy, Morgantown, 2006.
- [9] G. Brus, K. Miyoshi, H. Iwai, M. Saito, and H. Yoshida. Change of an anode’s microstructure morphology during the fuel starvation of an anode-supported solid oxide fuel cell. *International Journal of Hydrogen Energy*, 40:6927–6934, 2015. doi: 10.1016/j.ijhydene.2015.03.143.
- [10] A. Buonomano, F. Calise, M. Dentice, A. Palombo, and M. Vicidomini. Hybrid solid oxide fuel cells – gas turbine systems for combined heat and power: A review. *Applied Energy*, 156:32–85, 2015. doi: 10.1016/j.apenergy.2015.06.027.

-
- [11] A. Burcat. Third Millennium Ideal Gas and Condensed Phase Thermochemical Database for Combustion with Updates from Active Thermochemical Tables. Technical Report September, Argonne National Laboratory, 2005. URL <http://garfield.chem.elte.hu/Burcat/burcat.html>.
- [12] F. Calise, M. Dentice, A. Palombo, and L. Vanoli. Simulation and exergy analysis of a hybrid Solid Oxide Fuel Cell (SOFC) – Gas Turbine System. *Energy*, 31:3278–3299, 2006. doi: 10.1016/j.energy.2006.03.006.
- [13] F. Calise, M. Dentice, L. Vanoli, and M. R. Von Spakovsky. Single-level optimization of a hybrid SOFC – GT power plant. *Journal of Power Sources*, 159:1169–1185, 2006. doi: 10.1016/j.jpowsour.2005.11.108.
- [14] F. Calise, A. Palombo, and L. Vanoli. Design and partial load exergy analysis of hybrid SOFC – GT power plant. *Journal of Power Sources*, 158:225–244, 2006. doi: 10.1016/j.jpowsour.2005.07.088.
- [15] F. Calise, M. Dentice, L. Vanoli, and M. R. Von Spakovsky. Full load synthesis/design optimization of a hybrid SOFC – GT power plant. *Energy*, 32:446–458, 2007. doi: 10.1016/j.energy.2006.06.016.
- [16] M. Carnogurská, M. Prihoda, M. Puskar, M. Fabian, R. Dobakova, and M. Kubik. Measurement and mathematical modelling of heat loss in the pipe systems of a central heat distribution network. *Measurement*, 94:806–811, 2016. doi: 10.1016/j.measurement.2016.09.033.
- [17] P. Costamagna, L. Magistri, and A. F. Massardo. Design and part-load performance of a hybrid system based on a solid oxide fuel cell reactor and a micro gas turbine. *Journal of Power Sources*, 96:352–368, 2001. doi: 10.1016/S0378-7753(00)00668-6.
- [18] I. W. S. L. Cruz, C. E. C. Alvarez, A. F. Teixeira, and R. M. Valle. Zero-dimensional mathematical model of the torch ignited engine. *Applied Thermal Engineering*, 103:1237–1250, 2016. doi: 10.1016/j.applthermaleng.2016.05.017.
- [19] M. L. Ferrari. Solid oxide fuel cell hybrid system : Control strategy for stand-alone configurations. *Journal of Power Sources*, 196(5):2682–2690, 2011. doi: 10.1016/j.jpowsour.2010.11.029.

-
- [20] S. Genić, I. Arandjelović, P. Kolendić, M. Jarić, N. Budimir, and V. Genić. A Review of Explicit Approximations of Colebrook’s Equation. *FME Transactions*, 39:67–71, 2011.
- [21] D. G. Goodwin (accessed 2017-02-14). Cantera, 2001-2010. URL <http://code.google.com/p/cantera/>.
- [22] M. Henke. *Pressurised Solid Oxide Fuel Cells: From Electrode Electrochemistry to Hybrid Power Plant System Integration*. PhD thesis, Institut für Thermodynamik und Wärmetechnik der Universität Stuttgart, 2015. URL <http://elib.uni-stuttgart.de/handle/11682/2409>.
- [23] M. Henke, M. Steilen, C. Schnegelberger, M. Riedel, M. Hohloch, S. Bücheler, M. Herbst, A. Huber, M. Heddrich, J. Kallo, and K. A. Friedrich. Construction of a 30 kW SOFC Gas Turbine Hybrid Power Plant. In *SOFC XIV*, 2015. URL <http://elib.dlr.de/97882/>.
- [24] M. Henke, M. Steilen, R. Näke, M. Heddrich, and K. A. Friedrich. Control strategy for a SOFC gas turbine hybrid power plant. In *12th European SOFC & SOE Forum*, 2016. URL <http://elib.dlr.de/105289/>.
- [25] M. Hohloch, A. Widenhorn, D. Lebküchner, T. Panne, and M. Aigner. Micro gas turbine test rig for hybrid power plant application. *ASME Turbo Expo, Berlin, Germany*, 2:499–506, 2008. doi: 10.1115/GT2008-50443.
- [26] IEA. World Energy Outlook 2016, 2016.
- [27] J. Leeper. 220 kWe Solid Oxide Fuel Cell/Gas Turbine Generator Hybrid Proof of Concept Demonstration Report. Technical report, California Energy Commission, 2001.
- [28] F. Leucht. *Der Festoxidbrennstoffzellengenerator im Hybridkraftwerk - Untersuchung von Betriebsweisen und ihrer Wirtschaftlichkeit*. PhD thesis, Institut für Thermodynamik und Wärmetechnik der Universität Stuttgart, 2012.
- [29] F. Leucht, W. G. Bessler, J. Kallo, K. A. Friedrich, and H. Müller-steinhausen. Fuel cell system modeling for solid oxide fuel cell / gas turbine hybrid power plants. Part I : Modeling and simulation framework. *Journal of Power Sources*, 196(3):1205–1215, 2011. doi: 10.1016/j.jpowsour.2010.08.081.
- [30] P. J. Lindstrom and W. G. Mallard (accessed 2017-02-14). Nist Chemistry Web Book, 2010. URL webbook.nist.gov/chemistry/fluid/.

-
- [31] E. J. Lopez and N. M. Nigro. Validation of a 0D / 1D Computational Code for the Design of Several Kind of Internal Combustion Engines. *Latin American Applied Research*, 184:175–184, 2010.
- [32] E. A. Mason and S. C. Saxena. Approximate Formula for the Thermal Conductivity of Gas Mixtures. *Physics of Fluids*, 361(1):361–369, 1958. doi: 10.1063/1.1724352.
- [33] M. F. Modest. *Radiative Heat Transfer*. Academic Press, 2013. ISBN 978-0-123-86944-9.
- [34] C. V. Ngayihi Abbe, R. Nzungwa, R. Danwe, Z. M. Ayissi, and M. Obonou. A study on the 0D phenomenological model for diesel engine simulation: Application to combustion of Neem methyl ester biodiesel. *Energy Conversion and Management*, 89:568–576, 2015. doi: 10.1016/j.enconman.2014.10.005.
- [35] D. Nguyen, J. Soria, and D. Honnery. Efficiency of the lumped parameter concept and the role of liquid properties in modelling microdroplet evaporation. *Fuel*, 166:86–95, 2016. doi: 10.1016/j.fuel.2015.10.097.
- [36] M. N. Özisik. *Heat Conduction*. John Wiley & Sons, Inc., 1993. ISBN 978-0-471-05481-8.
- [37] S. V. Patankar. *Numerical Heat Transfer and Fluid Flow*. Hemisphere Publishing Corporation, 1980. ISBN 978-0-891-16522-4.
- [38] F. Payri, P. Olmeda, J. Martín, and A. García. A complete 0D thermodynamic predictive model for direct injection diesel engines. *Applied Energy*, 88(12):4632–4641, 2011. doi: 10.1016/j.apenergy.2011.06.005.
- [39] M. Peksen. Numerical thermomechanical modelling of solid oxide fuel cells. *Progress in Energy and Combustion Science*, 48:1–20, 2015. doi: 10.1016/j.pecs.2014.12.001.
- [40] C.M. Rangel, R.A. Silva, M.A. Travassos, T.I. Paiva, and V.R. Fernandes. Fuel Starvation: Irreversible Degradation Mechanisms in PEM Fuel Cells. *18th World Hydrogen Energy Conference 2010*, 2010.
- [41] R. A. Roberts and J. Brouwer. Dynamic Simulation of a Pressurized 220 kW Solid Oxide Fuel-Cell – Gas Turbine Hybrid System: Modeled Performance Compared to Measured Results. *Journal of Fuel Cell Science and Technology*, 3(1):18, 2006. doi: 10.1115/1.2133802.

- [42] W. M Rohsenow, J. P. Hartnett, and Y. I. Cho. *Handbook of Heat Transfer*. McGraw-Hill, 1998. ISBN 978-0-070-53555-8.
- [43] T. Sathiyasheela and P. Mohanakrishnan. Annular fuel pin heat transfer and lumped model correction. *Progress in Nuclear Energy*, 52(5):487–490, 2010. doi: 10.1016/j.pnucene.2009.11.004.
- [44] C. Schnegelberger. Entwicklung und aufbau eines teststandes zur ermittlung zulässiger druckdifferenzen an feststoffoxidbrennstoffzellen. Master’s thesis, Technische Hochschule Mittelhessen, 2013. URL <http://elib.dlr.de/84930/>.
- [45] S. Seidler, M. Henke, J. Kallo, W. G. Bessler, U. Maier, and K. A. Friedrich. Pressurized solid oxide fuel cells: Experimental studies and modeling. *Journal of Power Sources*, 196(17):7195–7202, 2011. doi: 10.1016/j.jpowsour.2010.09.100.
- [46] Y. Shi, P. Lawford, and R. Hose. Review of zero-D and 1-D models of blood flow in the cardiovascular system. *Biomedical engineering online*, 10(1):33, 2011. doi: 10.1186/1475-925X-10-33.
- [47] The MathWorks, Inc. MATLAB, 1994-2017. URL mathworks.com/products/matlab.
- [48] T. Verstraete, Z. Alsalihi, and R. A. Van den Braembussche. Numerical Study of the Heat Transfer in Micro Gas Turbines. *Journal of Turbomachinery*, 129:835, 2007. doi: 10.1115/1.2720874.
- [49] S. E. Veyo, L. A. Shockling, J. T. Dederer, J. E. Gillett, and W. L. Lundberg. Tubular Solid Oxide Fuel Cell / Gas Turbine Hybrid Cycle Power Systems: Status. *Journal of Engineering for Gas Turbines and Power*, 124:845–849, 2002. doi: 10.1115/2000-GT-0550.
- [50] W. P. J. Visser, S. A. Shakariyants, and M. Oostveen. Development of a 3 kW Microturbine for CHP Applications. *Journal of Engineering for Gas Turbines and Power*, 133:042301–1–8, 2011. doi: 10.1115/1.4002156.
- [51] E. W. Weisstein (accessed 2017-02-10). Mathworld – A Wolfram Web Resource – Horner’s Rule, 2010. URL <http://mathworld.wolfram.com/HornersRule.html>.

- [52] C. Willich, C. Westner, S. Seidler, F. Leucht, M. Henke, J. Kallo, U. Maier, and K. A. Friedrich. Pressurized Solid Oxide Fuel Cells : Operational Behavior. In *Conference Paper*, 2011.
- [53] X. Wu, Q. Huang, and X. Zhu. Thermal modeling of a solid oxide fuel cell and micro gas turbine hybrid power system based on modified LS-SVM. *International Journal of Hydrogen Energy*, 36(1):885–892, 2010. doi: 10.1016/j.ijhydene.2010.08.022.